

AN EXPERIMENTAL DETERMINATION OF THE  
TOPOLOGICAL PROPERTIES OF SINTERED STRUCTURES

By  
EDWARD HOWARD AIGELTINGER

A DISSERTATION PRESENTED TO THE GRADUATE COUNCIL OF  
THE UNIVERSITY OF FLORIDA  
IN PARTIAL FULFILLMENT OF THE REQUIREMENTS FOR THE  
DEGREE OF DOCTOR OF PHILOSOPHY

UNIVERSITY OF FLORIDA

1970

DEDICATED TO

MY MOTHER  
AND  
FATHER

## ACKNOWLEDGMENTS

The research and studies which resulted in this dissertation were supported, in part, by a College of Engineering Fellowship at the University of Florida. The author expresses his appreciation for this and all other financial aid provided by the University and the State of Florida.

The author wishes to express his sincere gratitude to Dr. R. T. DeHoff, chairman of his supervisory committee, for his invaluable guidance and assistance during the course of this research.

The use of the results obtained by Dr. J. R. Steele and the helpful discussion of Dr. J. Kronsbein, Dr. R. A. Gregg and Dr. J. H. Steele, Jr. were appreciated and are hereby acknowledged.

The financial support of this research by the Atomic Energy Commission under Contract No. AT(40-1)2851 was appreciated and is hereby acknowledged.

Finally, the author wishes to thank Dr. F. N. Rhines, chairman of the Metallurgy and Materials Engineering Department, Dr. E. D. Verink, Dr. J. B. Conklin, Jr. and Dr. E. H. Radlock for serving on his supervisory committee.

## TABLE OF CONTENTS

	Page
ACKNOWLEDGMENTS.....	iii
LIST OF TABLES.....	x
LIST OF FIGURES.....	xii
ABSTRACT.....	xxiv
CHAPTER	
I INTRODUCTION.....	1
1.1 Sintering and Powder Metallurgy.....	1
1.2 General Features of the Sintering Process.....	2
1.3 General Features of the Geometrical Evolution of a Powder Aggregate During Sintering.....	2
1.4 Parameters Employed to Monitor Micro-structure of Powder Aggregates During the Sintering Process.....	7
1.5 Purpose and Scope of This Research.....	8
1.6 General Applicability of the Topological Approach for Studying Microstructures....	9
1.7 General Applicability of the Method of Analysis Presented in This Dissertation..	10
II NETWORK TOPOLOGY APPLIED TO SINTER STRUCTURES.	11
2.1 Introduction.....	11
2.2 Properties of Networks.....	11



Chapter		Page
	2.3 Characterization of Sinter Structures According to Their Topological Properties.....	13
	2.4 Construction of a Linear Graph Associated with a Sinter Structure.....	14
III	EXPERIMENTAL PROCEDURE.....	21
	3.1 Sample Preparation.....	21
	3.2 Determination of Sample Densities.....	23
	3.3 Determination of the Number of Particles per Gram for the Unsintered Powders.....	23
	3.4 The Serial Sectioning Technique.....	24
	3.5 Methods Used to Obtain Serial Sections...	26
IV	DETERMINATION OF THE GENUS AND NUMBER OF SEPARATE PARTS FROM SERIAL SECTIONS.....	32
	4.1 Introduction.....	32
	4.2 Determination of the Genus of Sinter Structures by Counting Contacts per Particle.....	33
	4.3 Determination of the Genus of Sinter Structures After Kronsbein, <u>et al.</u> .....	37
	4.4 Determination of the Number of Separate Parts per Unit Volume.....	44
	4.5 General Features of an Improved Method for the Determination of the Genus of Sinter Structures.....	44
	4.5.1 Labeling Procedure.....	47
	4.5.2 Method II for the Determination of the Maximum Values of Cumulative Genus.....	57

Chapter		Page
	4.5.3 Determination of the Minimum Values of Cumulative Genus.....	70
	4.5.4 An Example Illustrating Method II for the Determination of the Maximum and Minimum Limits of the Cumulative Genus.....	77
	4.6 Determination of $G_V^{\max}$ and $C_V^{\min}$ from the Values of $G_1^{\max}$ and $G_1^{\min}$ .....	81
	4.7 Determination of the Number of Separate Parts per Unit Volume from the Values of Cumulative Separate Parts.....	87
	4.8 Method III.....	88
	4.9 Analysis of a Space, Material or Void, Which Exhibits Multiple Connectivity on a Single Microsection.....	96
V	EXPERIMENTAL RESULTS.....	118
	5.1 Introduction.....	118
	5.2 Topological Properties of the 115 Micron Spherical Powder.....	138
	5.2.1 Genus per Gram Data.....	138
	5.2.2 Number of Separate Parts per Gram Data.....	149
	5.3 Topological Properties of the 48 Micron Spherical Powder.....	154
	5.3.1 Genus per Gram Data.....	154
	5.3.2 Number of Separate Parts per Gram Data.....	162
	5.4 Topological Properties of the 48 Micron Electrolytic Powder.....	169
	5.4.1 Genus per Gram Data.....	169
	5.4.2 Number of Separate Parts per Gram Data.....	180

Chapter		Page
5.5	Metric Properties of the 48 Micron Spherical and Electrolytic Powders.....	187
5.5.1	Surface Area Data.....	187
5.5.2	Curvature Data.....	190
5.5.3	Grain Size and Grain Boundary Area Data.....	193
VI	DISCUSSION.....	203
6.1	Introduction.....	203
6.2	Variation of the Genus and Number of Separate Parts with Density for Spherical and Electrolytic Copper Powders.....	203
6.2.1	Genus of Spherical Powders.....	203
6.2.1.1	First stage sintering....	203
6.2.1.2	Second and third stage sintering.....	204
6.2.2	Variation of the Number of Separate Parts During Sintering for a Single Size Fraction of Spherical Copper Powder.....	209
6.2.3	Variation of the Genus During Sintering for 48 Micron Electrolytic Copper Powder.....	220
6.2.4	General Features of the Variation in the Number of Separate Parts for the 48 Micron Electrolytic Copper Powder.....	233
6.3	General Features of the Cumulative Genus Versus Volume of Material Analyzed Curves.....	236
6.3.1	$G_i^{\min}$ Curves.....	236
6.3.2	$G_i^{\max}$ Curves.....	242

Chapter		Page
6.4	General Features of the Cumulative Number of Separate Parts Versus Volume of Material Analyzed Curves.....	247
6.5	Comparison of the Genus Versus Volume Fraction of Porosity Curves for the 115 Micron Spherical, 48 Micron Spherical and 48 Micron Electrolytic Copper Powders.....	249
6.6	Comparison of the Number of Separate Parts per Gram Versus Volume Fraction of Porosity Curves for the 48 Micron Spherical and Electrolytic Copper Powders	255
6.7	Computer Model.....	258
6.8	Correlation Between the Computer Model Data and the Experimental Data.....	266
6.9	Variation in the Void-Solid Interface Area During Sintering for the 48 Micron Spherical and Electrolytic Copper Powders	273
6.10	Variation in Total Curvature per Unit Volume and Average Mean Curvature During Sintering for the 48 Micron Spherical and Electrolytic Copper Powders.....	286
6.11	Variation in Grain Boundary Structure During Sintering for the 48 Micron Spherical and Electrolytic Copper Powders.....	289
6.12	General Features of the Sintering Process	293
6.13	Sampling Error Involved in the Determination of the Genus and Number of Separate Parts.....	295
6.13.1	Difference Between $G_V^{\max}$ and $G_V^{\min}$ .....	295
6.13.2	Correlation Error.....	296
6.13.3	Total Number of Serial Sections Which Must Be Analyzed to Obtain a Given Level of Accuracy.....	297

Chapter		Page
	6.13.4 Error Resulting from Inhomogeneity of the Sinter Structures.....	297
	6.13.5 Error Resulting from Uncertainty in the Position of the Deformation Retract.....	298
	6.13.6 Error Resulting from the Presence of Large-Scale Features in the Structure.....	303
	6.13.7 Error in the Number of Separate Parts.....	304
	6.14 The Design of Serial Sectioning Experiments.....	304
VII	CONCLUSIONS AND SUGGESTED RESEARCH.....	305
	7.1 Conclusions.....	305
	7.2 Suggested Research.....	307
APPENDICES		
1	DETERMINATION OF THE NUMBER OF IDENTIFIABLE FEATURES PER UNIT VOLUME USING SERIAL SECTIONS	310
2	SEPARATE PARTS ERROR RESULTING FROM THE SURFACE EFFECT.....	313
3	RELATION BETWEEN THE VALUES OF GENUS FOR TWO DIFFERENT SIZE FRACTIONS OF SPHERICAL POWDER..	317
4	SAMPLING ERROR.....	319
	REFERENCES.....	324
	BIOGRAPHICAL SKETCH.....	327

# LIST OF TABLES

Table		Page
1.	Labels and their meanings.....	48
2.	Events which must be noted as successive serial sections are considered and the labels associated with each of these events. The numbers in parentheses refer to the 11 steps presented in the text.....	49
3.	Data taken from the node-branch network of Figure 24.....	84
4.	Classification of changes which occur during the analysis of serial sections.....	101
5.	Data for those samples for which contacts per particle were counted.....	139
6.	Frequency of the number of contacts per particle for a sample of 115 micron spherical copper powder sintered to a density of 6.15 gm/cc ( $V_v = 0.314$ ).....	141
7.	Values of genus per gram for 115 micron spherical copper powder sintered to densities of 6.67 and 7.05 gm/cc.....	146
8.	Genus per gram and number of separate parts per gram data for 115 micron spherical copper powder sintered to four different densities....	152
9.	Values of genus per gram for the 48 micron spherical copper powder sintered to densities of 7.26, 7.74, 8.00, 8.25 and 8.40 gm/cc.....	155
10.	Number of separate parts per gram data for the 48 micron spherical and electrolytic copper powders.....	170

Table		Page
11.	Values of genus per gram for the 48 micron electrolytic copper powder.....	181
12.	Values of parameters used in the estimation of the number of separate parts per gram for 48 micron electrolytic copper powder sintered to a density of 8.45 gm/cc.....	188
13.	Surface area per unit volume and per unit mass for 48 micron spherical and electrolytic copper powders sintered to the indicated densities...	191
14.	Curvature data for the 48 micron spherical and electrolytic copper powders.....	194
15.	Grain size and grain boundary area data for the 48 micron spherical and electrolytic copper powders.....	196
16.	Computer model data for the 115 micron spherical copper powder.....	268
17.	Computer model data for the 48 micron spherical copper powder.....	269
18.	Computer model data for the 48 micron electrolytic copper powder.....	270
19.	Values of L and D.....	316

# LIST OF FIGURES

Figure		Page
1.	Illustration of neck formation and the channel closure process.....	4
2.	Illustration of the formation of an isolated separate part of the void-solid interface.....	5
3.	Illustration of the deformation retract (dotted line) of a solid.....	15
4.	Illustration of the effect of dummy nodes on the connectivity of a node-branch network....	18
5.	Illustration of the superposition of a node-branch network in a portion of the void space of a sinter structure.....	19
6.	Unsintered 48 micron electrolytic copper powder particles (100 X).....	22
7.	Jung ultra-microtome used to obtain serial sections.....	27
8.	Bakelite mount containing seven samples which were simultaneously sectioned by metallographic polishing.....	30
9.	Schematic serial sections illustrating (a) double multiple connectivity on a section and (b) single multiple connectivity (shaded phase).....	34
10.	Illustration of the effect of the external node on the deformation retract.....	39
11.	Three schematic serial sections and the corresponding node-branch network.....	42



Figure		Page
12.	Illustration of branching events.....	52
13.	Illustration of joining events.....	54
14.	Illustration of branching of a new channel....	56
15.	Illustration of several events which occur between serial sections.....	59
16.	Illustration of a branch which comes in from the side of the sample and then ends.....	63
17.	Illustration of a branch ending which is incident on an internal node.....	65
18.	Illustration of the equivalence of a five- branch and three three-branch nodes.....	68
19.	Illustration of a new channel which branches with one branch ending on a subsequent section.....	69
20.	Illustration of capped branches at the sample surface during determination of the minimum limit of the genus.....	71
21.	Illustration of the effect of branching and joining events on the value of $G_1^{\min}$ .....	73
22.	Illustration of the subnetwork graph associated with the determination of the values of $G_1^{\min}$ .....	75
23.	Three schematic serial sections and their deformation retracts used to illustrate Method II.....	78
24.	Hypothetical node-branch network.....	83
25.	Cumulative plots for the network shown in Figure 24.....	86
26.	Illustration of a node which branches down....	90
27.	Illustration of a node which branches up.....	92
28.	Subnetwork graph associated with the analysis of the network shown in Figure 24.....	93
29.	Hypothetical serial section illustrating the construction of a network analogous to the deformation retract in three dimensions.....	99

Figure		Page
30.	Appearance and disappearance of circuits associated with separate parts during the analysis of the solid space.....	103
31.	Illustration of (a) appearance of a new circuit and (b) appearance of a new branch in the subnetworks constructed on successive serial sections.....	105
32.	Illustration of the separation of a sub-network between two successive serial sections.....	109
33.	Illustration of sample surface effects. The appearance and disappearance of (a) branches to the external node and (b) circuits incident on the external node.....	111
34.	Hypothetical serial sections illustrating the analysis of a space which exhibits multiple connectivity on the serial sections.....	113
35.	Two serial sections through a sample of 48 micron electrolytic copper powder sintered to a density of 6.05 gm/cc illustrating several of the types of changes which occur as successive serial sections are analyzed.....	116
36.	Serial sections through 115 micron spherical copper powder sintered to densities of (a) 5.94 and (b) 6.15 gm/cc (125 X).....	119
37.	Serial sections through 115 micron spherical copper powder sintered to densities of (a) 6.67 and (b) 7.05 gm/cc (125 X).....	120
38.	Serial sections through 115 micron spherical copper powder sintered to densities of (a) 7.50 and (b) 7.76 gm/cc (125 X).....	121
39.	Serial section through 115 micron spherical copper powder sintered to a density of 8.05 gm/cc (125 X).....	122
40.	Serial sections through 48 micron spherical copper powder sintered to a density of 5.91 gm/cc (a) etched (200 X) and (b) unetched (130 X).....	123

Figure		Page
41.	Serial sections through 48 micron spherical copper powder sintered to a density of 6.62 gm/cc (a) etched (200 X) and (b) unetched (130 X).....	124
42.	Serial sections through 48 micron spherical copper powder sintered to a density of 7.26 gm/cc (a) etched (200 X) and (b) unetched (130 X).....	125
43.	Serial sections through 48 micron spherical copper powder sintered to a density of 7.74 gm/cc (a) etched (200 X) and (b) unetched (130 X).....	126
44.	Serial sections through 48 micron spherical copper powder sintered to a density of 8.00 gm/cc (a) etched (200 X) and (b) unetched (130 X).....	127
45.	Serial sections through 48 micron spherical copper powder sintered to a density of 8.25 gm/cc (a) etched (200 X) and (b) unetched (130 X).....	128
46.	Serial sections through 48 micron spherical copper powder sintered to a density of 8.40 gm/cc (a) etched (200 X) and (b) unetched (130 X).....	129
47.	Serial sections through 48 micron electrolytic copper powder sintered to a density of 1.30 gm/cc and infiltrated with epoxy (a) etched (200 X) and (b) unetched (100 X).....	130
48.	Serial sections through 48 micron electrolytic copper powder sintered to a density of 2.81 gm/cc and infiltrated with epoxy (a) etched (200 X) and (b) unetched (100 X).....	131
49.	Serial sections through 48 micron electrolytic copper powder sintered to a density of 3.99 gm/cc and infiltrated with epoxy (a) etched (200 X) and (b) unetched (100 X).....	132
50.	Serial sections through 48 micron electrolytic copper powder sintered to a density of 4.96 gm/cc and infiltrated with epoxy (a) etched (200 X) and (b) unetched (100 X).....	133

Figure		Page
51.	Serial sections through 48 micron electrolytic copper powder sintered to a density of 6.05 gm/cc and infiltrated with epoxy (a) etched (200 X) and (b) unetched (100 X).....	134
52.	Serial sections through 48 micron electrolytic copper powder sintered to a density of 6.95 gm/cc and infiltrated with epoxy (a) etched (200 X) and (b) unetched (100 X).....	135
53.	Serial sections through 48 micron electrolytic copper powder sintered to a density of 7.92 gm/cc and infiltrated with epoxy (a) etched (200 X) and (b) unetched (100 X).....	136
54.	Photomicrograph of 48 micron electrolytic powder sintered to a density of 8.45 gm/cc, etched (200 X).....	137
55.	Frequency distribution of contacts per particle for 115 micron spherical copper powder sintered to a density of 6.15 gm/cc ( $V_v = 0.314$ ).....	142
56.	Genus per gram and number of separate parts per gram versus volume fraction of porosity for 115 micron spherical copper powder.....	144
57.	Cumulative genus versus volume analyzed for 115 micron spherical copper powder sintered to a density of 6.67 gm/cc ( $V_v = 0.256$ ).....	147
58.	Cumulative genus versus volume of material analyzed for 115 micron spherical copper powder sintered to a density of 7.05 gm/cc ( $V_v = 0.213$ ).....	148
59.	Cumulative genus/volume analyzed versus number of sections analyzed for four samples of 115 micron spherical copper powder sintered to the indicated densities.....	150
60.	Cumulative number and cumulative volume density of separate parts versus volume analyzed for 115 micron spherical copper powder sintered to a density of 8.05 gm/cc ( $V_v = 0.102$ ).....	153
61.	Genus per gram versus volume fraction of porosity for 48 micron spherical copper powder.....	156

Figure		Page
62.	Cumulative genus versus volume analyzed for 48 micron spherical copper powder sintered to a density of 7.26 gm/cc.....	157
63.	Cumulative genus versus volume analyzed for 48 micron spherical copper powder sintered to a density of 7.74 gm/cc.....	158
64.	Cumulative genus versus volume analyzed for 48 micron spherical copper powder sintered to a density of 8.00 gm/cc.....	159
65.	Cumulative genus versus volume analyzed for 48 micron spherical copper powder sintered to a density of 8.25 gm/cc.....	160
66.	Cumulative genus versus volume analyzed for 48 micron spherical copper powder sintered to a density of 8.40 gm/cc.....	161
67.	Number of separate parts per gram (all and large) versus volume fraction of porosity for 48 micron spherical copper powder.....	163
68.	Cumulative number of separate parts versus volume analyzed for 48 micron spherical copper powder sintered to a density of 7.26 gm/cc....	164
69.	Cumulative number of separate parts versus volume analyzed for 48 micron spherical copper powder sintered to a density of 7.74 gm/cc.....	165
70.	Cumulative number of separate parts versus volume analyzed for 48 micron spherical copper powder sintered to a density of 8.00 gm/cc....	166
71.	Cumulative number of separate parts versus volume analyzed for 48 micron spherical copper powder sintered to a density of 8.25 gm/cc....	167
72.	Cumulative number of separate parts versus volume analyzed for 48 micron spherical copper powder sintered to a density of 8.40 gm/cc.....	168
73.	Genus per gram versus volume fraction of porosity for 48 micron electrolytic copper powder.....	171

Figure		Page
74.	Cumulative genus versus volume analyzed for 48 micron electrolytic copper powder sintered to a density of 1.30 gm/cc obtained by analysis of the metal space.....	172
75.	Cumulative genus versus volume analyzed for 48 micron electrolytic copper powder sintered to a density of 2.81 gm/cc obtained by analysis of the metal space.....	173
76.	Cumulative genus versus volume analyzed for 48 micron electrolytic copper powder sintered to a density of 3.99 gm/cc obtained by analysis of the metal space.....	174
77.	Cumulative genus versus volume analyzed for 48 micron electrolytic copper powder sintered to a density of 4.96 gm/cc obtained by analysis of the metal space.....	175
78.	Cumulative genus versus volume analyzed for 48 micron electrolytic copper powder sintered to a density of 6.05 gm/cc obtained by analysis of the metal space.....	176
79.	Cumulative genus versus volume analyzed for 48 micron electrolytic copper powder sintered to a density of 6.05 gm/cc obtained by analysis of the void space.....	177
80.	Cumulative genus versus volume analyzed for 48 micron electrolytic copper powder sintered to a density of 6.95 gm/cc obtained by analysis of the void space.....	178
81.	Cumulative genus versus volume analyzed for 48 micron electrolytic copper powder sintered to a density of 7.92 gm/cc obtained by analysis of the void space.....	179
82.	Number of separate parts per gram versus volume fraction of porosity for 48 micron spherical and electrolytic copper powders.....	182
83.	Cumulative number of separate parts versus volume analyzed for 48 micron electrolytic copper powder sintered to a density of 6.05 gm/cc.....	183

Figure		Page
84.	Cumulative number of separate parts versus volume analyzed for 48 micron electrolytic copper powder sintered to a density of 6.95 gm/cc.....	184
85.	Cumulative number of separate parts versus volume analyzed for 48 micron electrolytic copper powder sintered to a density of 7.92 gm/cc.....	185
87.	Total curvature per unit volume versus volume fraction of porosity for 48 micron spherical and electrolytic copper powders.....	192
88.	Average mean surface curvature versus volume fraction of porosity for 48 micron spherical and electrolytic copper powders.....	195
89.	Grain boundary area per unit volume versus volume fraction of porosity for 48 micron spherical and electrolytic copper powders.....	197
90.	Grain boundary area per unit mass versus volume fraction of porosity for 48 micron spherical and electrolytic copper powders.....	199
91.	Total grain surface area per unit volume versus volume fraction of porosity for 48 micron spherical and electrolytic copper powders.....	200
92.	Total grain surface area per unit mass versus volume fraction of porosity for 48 micron spherical and electrolytic copper powders.....	201
93.	Mean grain intercept versus volume fraction of porosity for 48 micron spherical and electrolytic copper powders.....	202
94.	(a) Schematic size distribution of channels. (b) Channel with smallest cross-sectional area denoted.....	206
95.	Illustration of the effect of a decrease in the width of the channel size distribution on the variation of the genus with pore volume fraction.....	208

Figure		Page
96.	Illustration of possible paths of variation in the shape of an irregularly shaped isolated separate part.....	210
97.	Hypothetical plots of genus and number of separate parts versus pore volume fraction for (a) perfect stacking and (b) imperfect stacking.....	212
98.	Illustration of the size of a small separate part relative to the spacing between serial sections.....	214
99.	Number of separate parts (all and small) versus volume fraction of porosity for 48 micron spherical copper powder.....	215
100.	Ratio of the number of small to the number of large separate parts versus volume fraction of porosity for 48 micron spherical copper powder.....	216
101.	Schematic separate parts illustrating the effect of channel closure on the number of separate parts.....	219
102.	(a) Cross section through three irregular powder particles. (b) Enlarged region of contact between two irregular powder particles	221
103.	Illustration of the closure of small channels between irregularly shaped particles.....	223
104.	Illustration of the pulling apart of filaments between irregularly shaped particles.....	224
105.	Photograph of a stack of 15 serial sections through 48 micron electrolytic copper powder sintered to a density of 2.81 gm/cc.....	226
106.	Genus per gram and number of separate parts per gram versus volume fraction of porosity for 48 micron spherical and electrolytic copper powders.....	228
107.	Illustration of the various factors which contribute to the genus of the 48 micron electrolytic copper powder.....	229



Figure		Page
108.	Two schematic channel size distributions.....	231
109.	Comparison of some features of the channel size distributions of the spherical and electrolytic powders.....	234
110.	Illustration of a measure of circuit size.....	238
111.	Thickness analyzed to reach linearity versus sample density for 48 micron electrolytic and spherical copper powders.....	240
112.	Frequency distribution of circuit size for four schematic node-branch networks.....	241
113.	Thickness analyzed to reach linearity versus genus per cc for 48 micron spherical and electrolytic copper powders.....	243
114.	Illustration of tree-like regions attached to multiply connected regions of the void space.....	244
115.	Comparison of genus per gram versus volume fraction porosity for 48 and 115 micron spherical copper powders.....	250
116.	Sample density versus sintering time for 48 micron spherical and electrolytic copper powders.....	253
117.	Genus per gram and number of separate parts per gram versus sintering time for 48 micron spherical and electrolytic copper powders.....	254
118.	Number of separate parts per gram versus sintering time for 48 micron spherical and electrolytic copper powders.....	257
119.	Average variation in $G/G_0$ and $N/N_0$ for the $3 \times 3 \times 3$ , $4 \times 4 \times 4$ and $5 \times 5 \times 5$ network models with the exterior node. The arrows indicate the direction in which the curves shift with increasing number of nodes, which is toward the limiting slopes shown by the dashed lines. (Steele [3]).....	260

Figure		Page
120.	Average variation in $G/G_0$ and $N/N_0$ for the $3 \times 3 \times 3$ , $4 \times 4 \times 4$ and $5 \times 5 \times 5$ network models without the exterior node. The arrows indicate the direction in which the curves shift with increasing number of nodes, which is toward the limiting slopes shown by the dashed lines. (Steele [3]).....	261
121.	Average distribution of nodes among different types of separate parts for the $5 \times 5 \times 5$ network with the exterior node. The curves represent the fraction of nodes contained in separate parts having the number of nodes indicated (1 for isolated nodes, 2 for isolated pairs of nodes, etc.). (Steele [3]).	263
122.	Average distribution of nodes among different types of separate parts for the $5 \times 5 \times 5$ network without the exterior node. The curves represent the fraction of nodes contained in separate parts having the number of nodes indicated (1 for isolated nodes, 2 for isolated pairs of nodes, etc.). (Steele [3]).....	264
123.	Average number of multiply connected separate parts in the $5 \times 5 \times 5$ network models with and without the exterior node. (Steele [3]).....	265
124.	Correlation of the computer model results and the experimental data for the 115 micron spherical and 48 micron spherical and electrolytic powders.....	271
125.	Comparison of the computer model results and the experimental results for the 115 micron spherical and 48 micron spherical and electrolytic powders.....	275
126.	Fraction of branches removed versus volume fraction of porosity for the 115 micron spherical and 48 micron spherical and electrolytic powders.....	277
127.	Illustration of the variation in the surface area per unit volume with sample density during the initial decrease in genus for the 48 micron electrolytic powder.....	280

Figure		Page
128.	Number of channels removed versus surface area per gram for 48 micron spherical and electrolytic copper powders.....	285
129.	Illustration of the curvature change associated with the channel closure event.....	288
130.	Schematic void space configuration employed to illustrate the error resulting from uncertainty in the position of the deformation retract....	300
131.	Cumulative grain data obtained from 72 serial sections. Note that the cumulative density approaches the asymptote (dashed line), which was calculated from the slope of the cumulative number data (Steele [3])......	312
132.	Illustration used to estimate the separate part error resulting from the surface effect..	314
133.	Illustration of a node-branch network formed from a stack of small cubes.....	320

Abstract of Dissertation Presented to the Graduate Council  
in Partial Fulfillment of the Requirements for the Degree of  
Doctor of Philosophy

AN EXPERIMENTAL DETERMINATION OF THE TOPOLOGICAL  
PROPERTIES OF SINTERED STRUCTURES

By

Edward Howard Aigeltinger

March, 1970

Chairman: Dr. R. T. DeHoff  
Major Department: Metallurgical and  
Materials Engineering

A procedure which allows the determination of the topological properties (genus and number of separate parts) of any sinter structure is presented. Experimental measurements of the topological properties were made on uncompacted, sintered copper samples as a function of pore volume fraction for two different size fractions of spherical powder (-270 +325 and -120 +140 mesh) and one size fraction of electrolytic powder (-270 +325 mesh) over the entire range of density available to the powders sintered in the uncompacted state. Measurements of the metric properties, surface area and average mean surface curvature of the void-solid interface and of grain boundary area and grain size were made for the -270 +325 mesh spherical and electrolytic powder samples. The results for the three different powders are compared and the differences in behavior are explained. The combination of the topological and metric properties results in a detailed, quantitative description of the evolution of geometry which occurs during the sintering process.

This evolution of geometry can be divided into three distinct stages of behavior in terms of the variation in the topological properties. During the first stage, the genus varies in a complicated way with increasing density which depends on the shape and initial stacking of the particles. The second stage begins as channels surrounded by three or more particles begin to close. As a result of the closure of channels, the genus decreases and isolated separate parts of the void space are formed. The void-solid interface which exists during the second stage is referred to as a conditional minimal surface. Channel closure and the removal of void space and void-solid interface are closely related during second-stage sintering. When channel closure is complete, the third stage begins and conglomeration of separate parts becomes the dominant geometric process. This three-stage behavior is also exhibited by the variation in the metric properties and the grain structure during the sintering process.

Normal grain growth was found to be closely associated with the closure of channels during the second stage of the sintering process after the conditional minimal configuration is established. Exaggerated grain growth was observed to occur at the same pore volume fraction independent of the genus of the void-solid interface.

The variation in the topological properties during the sintering process was found to agree closely with the predictions of a previously developed computer model.

## CHAPTER I

### INTRODUCTION

#### 1.1 Sintering and Powder Metallurgy

Sintering is a term which is descriptive of a process whereby a mass of particulate material is transformed, usually at elevated temperature, into a solid body. The sintering process is of importance in metallurgy, ceramics and chemistry.

In ceramics, for example, bricks are produced from particles of clay by firing at elevated temperature, and fuel elements for nuclear reactors are produced from uranium dioxide powder.

In chemistry, Teflon is produced from Teflon powder by exposure to pressure and elevated temperature.

According to Jones [1]:

Two main types of products are manufactured by powder metallurgy:

(a) materials which cannot easily be made any other way. Examples of this class are porous bearings and filters, metallic frictional materials, abrasive tools, electric lamp filaments, some electric contacts, motor and dynamo brushes, and a variety of soft and hard magnetic materials;

(b) materials which could be made by other methods, but for which the powder metallurgy technique may be more convenient or cheaper. Examples of this class include many of the rarer or precious metals, strip or extruded shapes in base metals or alloys, some bearing metals, some hard or soft magnetic materials, and a wide variety of engineering components, usually in iron or copper base alloys, usually fairly small, manufactured in competition with processes involving machining, drop forging, die casting, pressing, etc.

These widespread applications indicate the broad technological importance of the sintering process.

### 1.2 General Features of the Sintering Process

When a system of finely divided powder particles is exposed to a temperature close to, but below, the melting point of the particles, material rearrangement driven by the excess energy of the surface of the particles takes place. As a result, the particles become bonded together and a solid framework is produced. The primary changes resulting from the material rearrangement are densification and a decrease in the surface area of the void-solid interface of the solid framework.

An external pressure can be applied either before or during exposure to elevated temperature in order to accelerate densification.

Most materials will exhibit sintering behavior under the proper conditions of atmosphere, temperature and applied pressure.

### 1.3 General Features of the Geometrical Evolution of a Powder Aggregate During Sintering

As a result of the research presented in this dissertation, it is now possible to quantitatively establish the path of geometrical evolution of a powder aggregate which occurs during the sintering process. A qualitative description of this path of geometrical evolution will now be presented so that the parameters employed to monitor the geometric structure of powder aggregates undergoing sintering can be introduced.

In a powder aggregate to which no external pressure is applied and prior to exposure to the sintering conditions, there are points

of contact between the individual particles. This is shown schematically in Figure 1a for three spherical particles, each of which is in contact with the other two. Spherical particles of the same size are chosen here for simplicity of illustration. The powder particles in an actual structure can have a large distribution of sizes and can be irregular in shape.

On exposure to the sintering temperature and atmosphere, the points of contact grow into areas of contact, or necks, as shown in Figure 1b. This process is called neck growth and characterizes the first stage of sintering. The classification of the stages of sintering proposed by Rhines generally is followed here [2].

As necks in the structure continue to grow, adjacent necks come into contact, as indicated in Figure 1c. This results in the formation of throat or channel configurations, an example of which is shown in the same figure. On further sintering, these channels in the void space begin to close or pinch off, as shown in Figure 1d. The second stage of sintering is characterized by a decrease in the connectedness of the void space of the sinter structure which is produced by the closure of channels in the void network.

As channel closure events take place in the structure, the sequence of events illustrated in Figure 2 occurs. Figure 2a shows a portion of the void space of a hypothetical sinter structure, four channels of which are labeled with numbers. In Figure 2b, the channel labeled 1 has closed. In Figure 2c, the channel labeled 3 has closed, and in Figure 2d, all four channels have closed. This isolates the portion of the void space, labeled "separate part" in Figure 2d, from the remainder of the void space. This isolated



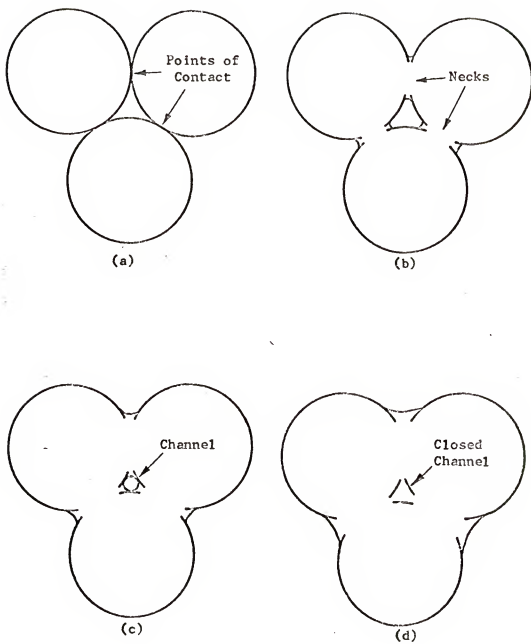


Figure 1. Illustration of neck formation and the channel closure process.

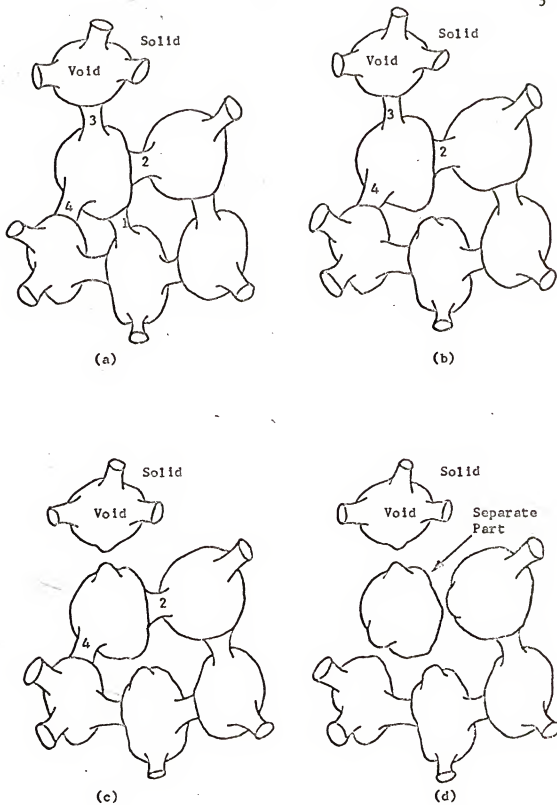


Figure 2. Illustration of the formation of an isolated separate part of the void-solid interface.

portion is no longer connected by any continuous path, entirely within the void space, to any region of the surrounding void space. The isolated portion is completely enclosed in solid material and, as in Figure 2d, is referred to as a separate part.

When a sufficient number of channels have closed, the void space will consist entirely of separate parts, each of which is topologically equivalent to a sphere.\* This condition characterizes the third and final stage of the sintering process.

During the first stage of sintering when the areas of contact between adjacent particles have been established, the structure consists of highly interconnected, solid and void space regions. The interconnectedness is quantitatively characterized by the connectivity, which is defined as the number of independent closed paths that can be formed within a constituent which cannot be shrunk continuously to a point without leaving the constituent [3].

During second-stage sintering, channel closure reduces the connectivity of the structure until, when the third stage of sintering is reached, the connectivity is zero.

The channel closure process manifests itself as a reduction in the connectivity of, and an increase in, the number of separate parts of the void space of the sinter structure. These changes account for a large portion of the total geometric change which occurs

---

\*Two surfaces are said to be topologically equivalent if they can be made to superimpose by continuous deformation. According to Barrett and Yust [6], "A precise mathematical definition of the topological equivalence of two sets is: a one-to-one transformation  $f(A) = B$  of  $A$  onto  $B$  is called a homeomorphism or topological mapping if  $f$  and  $f^{-1}$  are continuous. If such a mapping exists, then  $A$  and  $B$  are said to be homeomorphic or topologically equivalent."

during the sintering of a powder aggregate. Thus, the connectivity and number of separate parts are important parameters of the geometric structure of sinter bodies.

#### 1.4 Parameters Employed to Monitor Microstructure of Powder Aggregates During the Sintering Process

Microstructure is most commonly characterized by metric properties (e.g., length, area, volume) such as, in the case of sinter structures, volume fraction of porosity, surface area of void-solid interface per unit volume, total curvature of void-solid interface per unit volume [4], etc. These properties can be determined from counting measurements made on single, representative two-dimensional sections, coupled with probability arguments [4].

Another class of properties, the topological properties, can also be used to characterize microstructure. The topological properties are properties which are invariant with respect to continuous deformation. This allows considerable simplification and generalization of the geometric description of complex structures, such as those produced by sintering powder aggregates. As a result, it is possible to compare the behavior of quite different systems undergoing the sintering process, such as aggregates of particles of different sizes, shapes and materials.

As indicated in the preceding section, the connectivity and number of isolated separate parts of the void space are important microstructural parameters of sinter structures. These parameters belong to the class of topological properties, and, as shown in this dissertation and elsewhere [2, 5, 6], they can be used to characterize the geometric structure of powder aggregates during the sintering process.

### 1.5 Purpose and Scope of This Research

In order to obtain a relation between the structure and properties of a powder aggregate, the geometric structure must be quantitatively established. It is the purpose of the work presented in this dissertation to quantitatively determine the geometric structural evolution of a powder aggregate during the sintering process.

The geometric changes which take place during the sintering of a powder aggregate have been studied by means of simple systems, such as a spherical particle on a plate [7], two spherical particles [8], bundles of wires [9], etc. As a result of the simplicity of the systems involved, these investigations throw little light on the complex geometric changes which take place in an actual sinter body. Therefore, it is necessary to consider either more realistic models or the actual sinter structures. Measurements were made on the latter during the course of this research.

The topological properties of sinter structures were first considered by Rhines [2] and later by Kronsbein, et al. [5]. Unlike the metric properties, the topological properties cannot be determined from measurements made on a single two-dimensional microsection. At present, the topological properties can only be determined from an analysis which includes the third dimension of the structure.

An experimental procedure which allows the determination of the topological properties of sintered structures is presented in this dissertation and applied to a number of copper sinter bodies. Some of the metric properties of the structures considered during the course of this work were also measured. A description of the

sintering process in terms of the evolution of the topological and metric properties is then formulated.

#### 1.6 General Applicability of the Topological Approach for Studying Microstructures

The topological properties of the microstructure of a variety of materials are of interest. Some examples are: structures produced by recrystallization and grain growth [3, 10, 11, 12], multiply connected structures such as vycor glass [13] and sinter structures [2, 3, 5].

More specifically, the connectivity is of importance in most of the examples mentioned above. Delloff [4] and Cahn [14] have suggested that a phase transformation in the process of going from 0 to 100 per cent of a product phase passes through a configuration wherein both the parent and product phases are continuous and completely interconnected. Examples of this type of transformation are recrystallization in deformed metal structures, crystallization of glasses and ordering transformations.

It has been suggested that in multi-phase structures increased connectivity tends to increase the stability of the grain structure [3]. Such an effect could be of importance in high-temperature applications. It has also been stated that connectivity may be closely associated with superplastic behavior of materials since most, if not all, two-phase structures in which it has been observed appear to be highly interconnected [3].

### 1.7 General Applicability of the Method of Analysis Presented in This Dissertation

The method of analysis presented in this dissertation can be used to determine the connectivity and number of separate parts for any structure for which suitable serial sections are available. Serial sections are closely spaced, parallel microsections through the structure of interest.

The analysis can be applied to structures consisting of more than two kinds of constituents where a constituent is defined as a physically identifiable feature of the structure. Some examples, according to Steele [3], are grains in polycrystalline aggregates, solid and void-space regions in sinter bodies, eutectic or eutectoid regions in multi-phase alloys (e.g., pearlite colonies in mild steel), connected phase regions in multi-phase structures, anti-phase domains in ordered alloys and ferromagnetic domains. In a structure consisting of more than two constituents, the topological properties can be determined by applying the analysis to each individual constituent separately. This is considered further at the end of Section 4.9.

## CHAPTER II

### NETWORK TOPOLOGY APPLIED TO SINTER STRUCTURES

#### 2.1 Introduction

The procedure, presented in Chapter IV, which allows the determination of the topological properties of sintered structures, is based in principle on the construction of a network, or linear graph, which contains the same values of connectivity and number of isolated separate parts as the structure from which it is obtained.

Some of the properties of networks are presented in the next section. The construction of networks from sinter structures is then considered in the following sections.

#### 2.2 Properties of Networks

A number of properties of node-branch networks which are important in the characterization of sinter structures according to their topological properties are presented in this section.

According to Barrett and Yust [6]:

An arc is a line segment or a curved or elastically distorted form of a line segment:

A linear graph or network, designated as  $N$ , is a finite set of points together with a finite set of arcs. The points are called the vertices of  $N$ ; the arcs are called the edges of  $N$ . Each edge of a linear graph has a vertex at each end; each vertex is the end point of at least one edge; and any two edges are distinct except that they may have one or two ends in common with other edges.



Graphs can be thought of as lying in the plane or in three-dimensional space.

A path of the network  $N$  is a finite sequence of vertices,  $p_1$ , and edges,  $e_i$ , where  $e_i$  has vertices  $p_i$  and  $p_{i+1}$  for end points [i.e., the path is  $(p_1, e_1, p_2, e_2, \dots, p_i, e_i, p_{i+1}, \dots, e_{n-1}, p_n)$ ]. If  $p_1 = p_n$ , the path is closed. Note that a single vertex or edge may occur more than once in the sequence.

A graph is connected if there exists at least one path between each two vertices.

A circuit is a simple closed path in a graph with all the vertices (hence, all the edges) distinct (i.e., they appear only once) except that  $p_1 = p_n$ .

A graph that is connected and in which there are no circuits is called a tree.

Consider a network,  $N$ , having  $\mathcal{L}_0$  vertices and  $\mathcal{L}_1$  edges. If  $N$  is connected, then the number

$$\mu = \mathcal{L}_1 - \mathcal{L}_0 + 1 \quad (1)$$

is called the cyclomatic number; also the first Betti number of  $N$ . The following theorem follows directly, by an inductive argument on  $\mathcal{L}_1$ , from the foregoing definitions. The statement here is that of Cairns [15]; see also Arnold [16].

Theorem 1 - A connected graph  $G$  is a tree if and only if  $\mu = 0$ . If  $\mu \neq 0$ , then it is possible to reduce  $G$  to a tree by the removal of  $\mu$  suitably selected inner edges. This cannot be done by the removal of fewer than  $\mu$  edges, and  $G$  is necessarily disconnected by the removal of  $\mu + 1$  edges.

A network satisfies the Euler-Poincare equation [3]

$$\mathcal{L}_0 - \mathcal{L}_1 = p_0 - p_1 \quad (2)$$

where  $p_0$  and  $p_1$  are the zeroth and first Betti numbers ( $p_1$  rather than  $\mu$  is used for the first Betti number in this dissertation), respectively. The zeroth Betti number is the number of separate or disconnected parts or components of the network, and the first Betti number is the cyclomatic number or the connectivity of the network.

### 2.3 Characterization of Sinter Structures According to Their Topological Properties

According to Kronsbein, et al. [5], a sinter body may be considered to consist of the three-dimensional void and material, or solid, spaces, and the two-dimensional void-solid interface. The exterior of the sinter body is taken as part of the void space.

Consider the surface, the void-solid interface, which separates the void and material spaces. A topological property of such a surface is the genus, or handle number, which is the number of closed, non-self-intersecting cuts which can be made on the surface without separating it into two parts [3]. A cut is a separation of the surface along a simple curve.

The connectivity of either the void or material space is defined as the number of independent, closed paths, or circuits, which cannot be shrunk continuously to a point within the space [3]. Independent paths are paths which cannot be deformed so that they superimpose without leaving the space. The connectivity of the void or material space is equal to the genus of the bounding surface of the space. This is apparent as only paths which encircle handles of the bounding surface cannot be shrunk continuously to a point within the void or material space [3]. Since the same surface bounds both the void and material spaces, the connectivity of these spaces is the same [5]. Therefore, the term connectivity will be used with reference to a given sinter structure, and void, or material space, will not be designated unless one or the other is specifically under consideration.

The equivalence of the connectivity of the void and material spaces is indicated by the Alexander Duality Theorem. According to

Barrett and Yust [6],

$$p_1(X) = p_1(E^3 - X) \quad (3)$$

where  $E^3$  denotes three-dimensional space,  $X$  denotes a subset of space and  $E^3 - X$  denotes the complement of  $X$ .

This relationship indicates that the first Betti number of the void and material spaces of a sinter structure are equal since the material and void spaces are complementary spaces.

#### 2.4 Construction of a Linear Graph Associated with a Sinter Structure

Consider the solid shown in Figure 3 and the network represented by the dotted line placed inside the solid. According to Barrett and Yust, "The solid can be shrunk through itself onto the network, without closing any openings or creating new openings." A network obtained in this way is called the deformation retract of the solid.

As stated by Barrett and Yust [6]:

If (the set)  $A$  is a deformation retract of (the set)  $X$ , then the Betti numbers of  $A$  are equal to the Betti numbers of  $X$ .

The deformation retracts associated with the void-solid interface of sinter structures at various stages of the sintering process will now be considered. The network model of a sinter body was originally proposed by Rhines [2] and extended by Kronsbein, et al. [5]. The concept of the deformation retract was first applied to sinter structures by Kronsbein, et al. [5], although the term deformation retract was introduced into the metallurgical literature by Barrett and Yust [6].

At low density, when the individual particles are still distinguishable, the deformation retract can be developed as follows. Each particle is continuously shrunk to a point, or node,

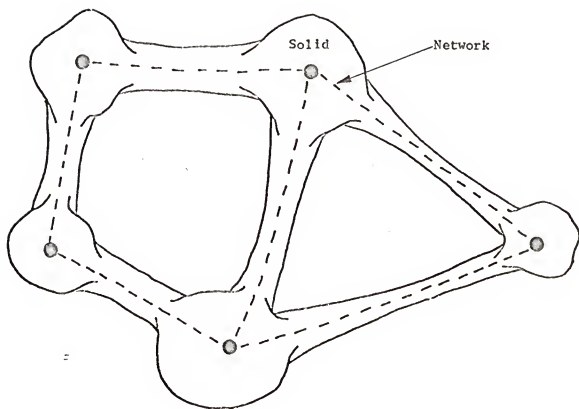


Figure 3. Illustration of the deformation retract (dotted line) of a solid.

and each contact between particles is simultaneously stretched axially and shrunk radially until it becomes a simple curve. The end points of each curve lie on the nodes representing the particles originally in contact. The connectivity,  $p_1$ , of a network so developed is equal to the genus,  $G$ , of the void-solid interface according to the preceding section and the statement by Barrett and Yust on page 14. In the range of density where this treatment can be applied, the solid and void each form a single, connected space. It is assumed that the solid space remains connected during sintering, as is experimentally observed. Thus, there is only one separate part, the solid or void space itself. Hence, the number of separate parts,  $p_0$ , is one and equation (1) becomes

$$G = c_1 - c_0 + 1 \quad (4)$$

where  $c_1$  is the number of branches (number of contacts or necks between particles,  $C$ ) and  $c_0$  is the number of nodes (number of particles,  $P$ ) in the network.

If the void rather than the solid space is considered, a deformation retract can again be constructed. This can be done in principle by superimposing a node-branch network in the void space in such a way that the network consists only of all linearly independent closed paths, or circuits, which cannot be shrunk to a point entirely within the void space. Thus, according to the definition on page 13, such a network has a value of connectivity equal to that of the void space. A network constructed in this manner is not unique, as in the case of the deformation retract of the solid space at low density. This is because the geometry of the

void space is not such that nodes and branches can be uniquely defined. This non-uniqueness will now be considered in detail.

The number of nodes and branches in a given network can be increased or decreased without changing the connectivity of the network as long as no new loops or separate parts are created in the network. For example, consider the four-node, six-branch network of connectivity three shown in Figure 4a. In Figure 4b, six nodes and six branches are added without creating new loops or separate parts in the network. The connectivity of the network is still three. The superfluous nodes are called dummy nodes. Dummy nodes are defined as nodes which have only one or two branches incident upon them.

Now consider the hypothetical toroidal configuration of a portion of the void space of a sinter structure shown in Figure 5a. This configuration has a genus of one according to the definition of genus given on page 13. Two possible configurations of the deformation retract are shown in Figures 5b and 5c. According to equation (1), the connectivity of both networks is one. An infinite number of node-branch networks could be superimposed in the void configuration of Figure 5a, all having the same value of connectivity. This is true for the deformation retracts of the void spaces of all sinter structures. From this example and from equation (1) it can be seen that as long as the quantity  $\mathcal{L}_1 - \mathcal{L}_0$  remains invariant (and the number of separate parts,  $p_0$ , remains unchanged), then the connectivity is invariant. Thus, it can be stated that the genus of a sinter body is equal to the connectivity of any of its deformation retracts. It is this property which is fundamental to

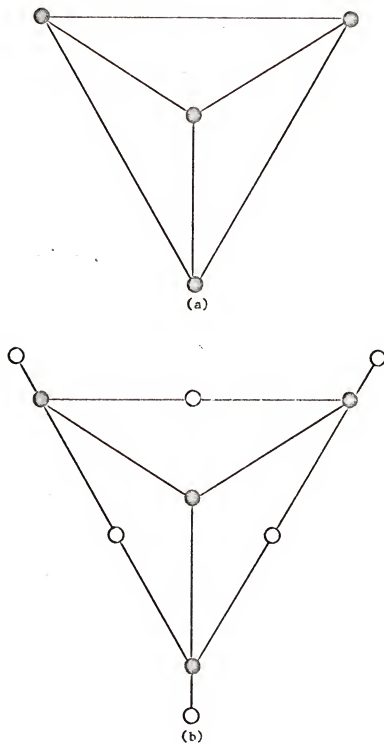


Figure 4. Illustration of the effect of dummy nodes on the connectivity of a node-branch network.

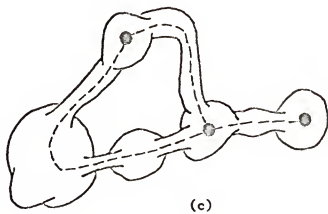
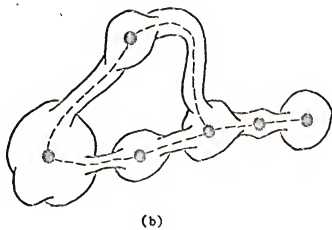
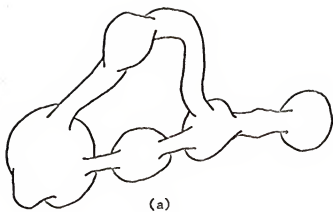


Figure 5. Illustration of the superposition of a node-branch network in a portion of the void space of a sinter structure.



the determination of the genus of a sinter structure from consideration of the void space.

The retraction of the solid, or material, space onto a network cannot be performed after isolated parts of the void space, which are topologically equivalent to a sphere, begin to form. This is because the surface of such a separate part cannot be retracted onto a linear network through the solid space. When such separate parts are present, the network representation can be maintained by retraction through the void space. In this case, separate parts which are topologically equivalent to a sphere form vertices.

Such vertices violate the definition of a network given by Barrett and Yust [6] as they have no edge incident upon them. They are, however, considered as part of the network during the course of this work.

The retraction of the void-solid interface through the void space of a sinter structure, therefore, results in a network, the connectivity and number of separate parts of which are equal to the genus and number of separate parts of the void-solid interface. This statement applies to structures of any density.

## CHAPTER III

### EXPERIMENTAL PROCEDURE

#### 3.1 Sample Preparation

Three different copper powders were used in this study, two different spherical size fractions, -120 +140 mesh (-125 +105 microns) and -270 +325 mesh (-52 +44 microns) and one size fraction of electrolytic powder, -270 +325 mesh. The numbers used to designate a given powder size correspond either to the number of screen openings per inch or to the average size of the screen openings. Minus (-) and plus (+) signs indicate that the particles will and will not pass through the corresponding screens, respectively. The spherical copper powder used for this work is a product of Linde Company, Inc. It was produced by atomization of liquid copper in an inert gas atmosphere. Copper oxide contained in the particles was negligible. This allowed sintering to be carried out in a dry hydrogen atmosphere without any significant production of gas pores internal to the particles. The electrolytic copper powder was produced by Malone Metal Powders Company, Inc. and is called Fernlock Copper. The electrolytic powder particles have the shape shown in the photomicrograph of Figure 6.

Both the spherical and the electrolytic powders were separated into size classes by standard ASTM sieve separation procedures. A



Figure 6. Unsintered 48 micron electrolytic copper powder particles (100 X).

standard Ro-Tap mechanical separator was used to prepare the powder size fractions for this work.

All powders were sintered in the uncompactd state at  $1005^{\circ}\pm 5^{\circ}\text{C}$  under a flowing dry hydrogen atmosphere. Samples covering the full range of density attainable under these conditions were prepared for all three powders. These samples were then used for the determination of the topological and metric properties of the sinter structures over the full range of density.

### 3.2 Determination of Sample Densities

The densities of all sinter structures were determined by a liquid displacement method. A sample is weighed and then immersed in liquid paraffin in order to seal surface pores. It is then weighed in air and in water, the difference in these two weights being the weight of water displaced by the sealed sample. From this weight and the density of water, the volume of the sample can be determined. The initial weight divided by this volume is the density of the sinter structure.

### 3.3 Determination of the Number of Particles per Gram for the Unsintered Powders

In order to obtain an estimate of the number of particles per gram for the -270 +325 mesh electrolytic powder, it was necessary to determine the average volume of these irregularly shaped particles. This was done in the following way. An alumina boat was partially filled with alumina powder. Particles of the electrolytic copper powder were then thinly spread over the surface of the alumina powder. The boat was placed in a furnace under flowing dry hydrogen at a temperature slightly greater than  $1083^{\circ}\text{C}$ , the melting point of

copper. The irregularly shaped electrolytic particles melted and were spheroidized by the surface tension of the liquid copper. The particles remained spherical on solidification. The average diameter of the spheroidized particles was measured and the average volume per particle calculated. The number of particles per gram was determined from the average volume per particle and the theoretical density of copper.

The volume per particle of the spherical powders used in this work was calculated from the average particle diameter. The average number of particles per gram was determined from the average volume per particle and the unsintered density of the powder.

#### 3.4 The Serial Sectioning Technique

As mentioned previously, it is necessary to consider the three-dimensional structure of a sinter body in order to determine the topological properties, genus and number of separate parts. The three-dimensional structure can be observed by means of a set of closely spaced microsections through the structure referred to as serial sections. The spacing of the serial sections must be small enough so that the property of the structure being monitored can be determined without loss of important detail between sections. During the course of this work, it was found that ten to fifteen serial sections in a distance equal to the diameter of the smallest particles in the structure are adequate for the determination of the topological properties of a sinter body. The most desirable spacing depends on a number of factors: the material under consideration, the parameter being monitored and the desired accuracy of the results.

The average spacing employed for the -120 +140 mesh spherical powder was 8.5 microns, or 13 to 14 sections per particle. For the -270 +325 mesh spherical powder, an average spacing of 4.31 microns was used, or 11 to 12 sections per particle. It was necessary to use more closely spaced sections for the -270 +325 mesh electrolytic powder because of the irregular particle shape. The average spacing used in this case was 1.58 microns, or about one-third that used for the same size fraction of spherical powder.

The serial sectioning technique can be employed to measure the volume density of a variety of properties. It has been used by Steele [3] in an analysis of the topological properties of grain structures, by Craig [17] to estimate changes in the density of quadruple point configurations during grain growth, by Buteau [18] to measure connectivity in sintered structures and by Kraft, et al. [19] to study faults in a lamellar eutectic structure. Serial sectioning has also been used in the life sciences to study complex three-dimensional shapes.

Properties which might be measured by the serial sectioning technique are, according to Steele [3]:

1. Number of identifiable structural features per unit volume (e.g., grains, faces, triple lines, inclusions, twins, phase regions, voids, eutectic faults, etc.).
2. Three-dimensional size and shape (e.g., size distribution, configurational distributions for grains and faces, shape parameters such as used by DeHoff [20] for elliptical particles, etc.).
3. Spatial distribution (e.g., association of grain boundaries and recrystallization [21], relationship of voids and grain boundaries in sinter bodies [22], spatial distribution of the product phases resulting from phase transformations [23], etc.).

4. Topological properties (e.g., connectivity, Gaussian curvature,\* number of separate parts, etc.).

### 3.5 Methods Used to Obtain Serial Sections

The serial sections used to obtain the data presented in this dissertation were prepared either by means of an ultra-microtome or by standard metallographic polishing techniques.

A Jung microtome, capable of cutting layers approximately one micron thick from a metal sample, was equipped with a microscope so that photomicrographs could be made without removing the sample from the microtome. The microtome and microscope attachment is shown in Figure 7. This insured that the surfaces produced remained parallel as the sample was sectioned. The fully annealed copper sinter bodies analyzed during the course of this work, when cut with the microtome, produced badly smeared surfaces. In order to prevent this smearing, the low density samples, having a void space network open to the surface of the sample and internally connected, were immersed in molten 50-50 Pb-Sn solder in order to fill the void space network. The solder was held at about 450°C, and the samples were immersed for about one minute. This was sufficient to infiltrate a layer a few mm thick adjacent to the external surface of the samples. The samples, after this process, did not smear on cutting with the microtome and appeared to be brittle rather than soft during cutting. This behavior is probably a result of the formation of a brittle

---

\*The local value of the Gaussian curvature is

$$K \equiv \frac{1}{r_1} \frac{1}{r_2}$$

where  $r_1$  and  $r_2$  are the principal local radii of curvature.

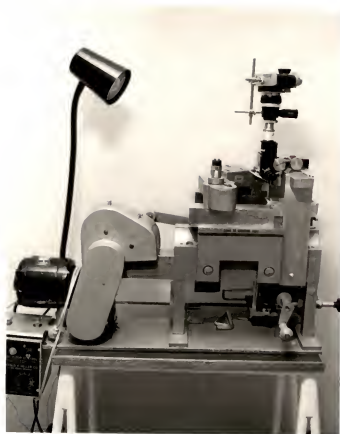


Figure 7. Jung ultra-microtome used to obtain serial sections.



phase or phases at the solder-copper interface. Photomicrographs of the cut surface produced by this technique are shown in Figures 36 to 38. Photomicrographs could be taken at any multiple of the one-micron cut made by the microtome. Five to ten cuts were taken between all sections obtained by means of the microtome.

Since the distance between sections must be accurately known in order to determine the genus from the serial sections, a block of dental cold-mount was placed in the microtome and cut 200 times at the one-micron-per-cut setting. The thickness removed was then measured with a micrometer. This thickness divided by 200 gave the average thickness per cut of the microtome as 0.85 micron.

High-density samples, for which the internal void space is sealed off at the surface of the sample, could not be infiltrated with solder, and therefore could not be sectioned with the microtome. These samples were sectioned by polishing with a standard metallographic technique. Since it is necessary to section the high-density samples in this way, it is convenient to mount both high-and low-density samples together in the same bakelite mount and polish all simultaneously. Thus, when high-density samples must be sectioned, it is not necessary to use the microtome for sectioning any samples. This, of course, assumes that samples covering a range of density are being analyzed, as was the case for the work presented here. If only low-density sinter structures are to be sectioned, then the microtome can be used. It should also be noted that the microtome can be employed to section fully dense materials where smearing over of the void region is not a problem [3, 17].

Figure 8 shows one bakelite mount containing seven samples of sintered copper powder which were all sectioned by metallographic polishing at the same time. The thickness of each sample, from the sample surface to the back of the bakelite mount, was measured with a micrometer. The differences in thickness, before and after each section, give the thickness of material between sections. These differences in thickness were determined to  $\pm 0.00002$  inch. Note that the total thickness of the bakelite mount could not be determined to greater than  $\pm 0.0005$  inch accuracy. Only differences in thickness could be determined to  $\pm 0.00002$  inch.

The metallographic polishing procedure employed consisted of polishing with 600-grit silicon carbide powder on a Buehler Microcloth until the desired amount of material was removed. The surface produced by this polishing process was sufficient for the determination of the topological properties. Rounding of the samples and bakelite mount during the repeated polishing steps was reduced by placing a copper ring around the samples near the edge of the bakelite mount, as shown in Figure 8. This ring also served as a means by which pitting during the polishing process could be detected. The solid-copper ring was periodically checked for pitting during the polishing step as pores and pits could not be distinguished on the copper sinter bodies. In this way the polishing variables could be controlled so that pitting did not occur.

Low-density sinter structures (less than about one-half theoretical density) undergo rounding on a microscopic scale to an unacceptable extent during the polishing process. To prevent this, all samples having an interior void space connected to their surfaces



Figure 8. Bakelite mount containing seven samples which were simultaneously sectioned by metallographic polishing.

were infiltrated with a hard epoxy resin. This was done by placing the sinter body under the liquid epoxy in a vacuum system attached to a mechanical vacuum pump, evacuating the system and then opening the system to the atmosphere. This procedure forces epoxy into the void space of the structure. As a result, rounding on a microscopic scale is reduced to a level such that the topological measurements can be made with a high degree of certainty. The samples shown in Figures 47 to 53 were infiltrated with epoxy and successfully serial sectioned using this technique. The lowest density material, shown in Figure 47, has a volume fraction of porosity of 0.855.

As a result of the microscopic surface rounding, point counts (to determine pore volume fraction) and tangent counts (to determine total and average mean surface curvature) were not made on surfaces which were used for the topological measurements. New surfaces were prepared for this purpose which had an acceptably small degree of rounding.

CHAPTER IV  
DETERMINATION OF THE GENUS AND NUMBER OF  
SEPARATE PARTS FROM SERIAL SECTIONS

4.1 Introduction

Several methods of analysis which can be applied to sinter structures in order to determine the genus and number of separate parts are presented in this chapter. The methods of analysis are presented in the order in which they were employed during the course of this work. As the work progressed, improvements were made in the procedure so that it became more efficient and consequently less time consuming. The most general and least time-consuming method of analysis is presented in Section 4.9; the reader not interested in the chronological development of the procedure is referred to this section.

The procedure presented by Kronsbein, et al. [5] (Section 4.3) was used first. This method was then modified during the course of this work to obtain Method II (Section 4.5), a less time-consuming method of analysis. Method II was then modified further to obtain a still more efficient procedure, Method III (Section 4.8).

The method of Kronsbein, et al. [5] and Method II can only be applied to structures which do not possess double multiple connectivity on a given microsection. Double multiple connectivity on a given

microsection is manifested by loops in both the solid and void space which cannot be shrunk to a point without crossing the void-solid interface, as indicated by the dotted lines in Figure 9a. Actual sinter structures possessing double multiple connectivity are shown in Figures 49, 50 and 51.

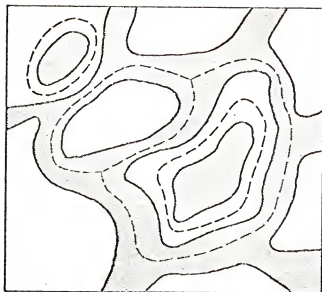
Figure 9b shows a schematic microsection which possesses single multiple connectivity. The shaded space is simply connected and the unshaded space is multiply connected. The sinter structures shown in Figures 46 and 53 have single multiple connectivity on a given microsection. The solid space of the microsection shown in these figures is multiply connected and the void space is not. It is also possible for the void space of a microsection to be multiply connected and for the solid space to be simply connected. Such a structure is shown in Figure 47.

Both of these structures can be analyzed by either of the two methods of analysis which can be applied only to structures without double multiple connectivity on a given microsection. These two methods of analysis can only be applied to the space which is simply connected on a given microsection; e.g., the void space of Figure 46 or the solid space of Figure 47.

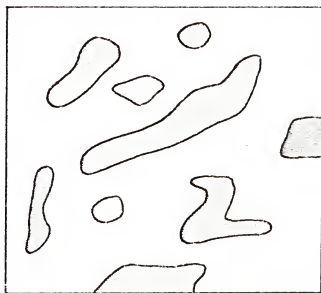
Only Method III can be employed to analyze a space which is multiply connected on a given microsection. As a result, Method III can be used to analyze either space of any sinter structure.

#### 4.2 Determination of the Genus of Sinter Structures by Counting Contacts per Particle

Consider a sinter structure during the first stage of sintering when contacts between the individual particles are distinguishable.



(a)



(b)

Figure 9. Schematic serial sections illustrating (a) double multiple connectivity on a section and (b) single multiple connectivity (shaded phase).

In this case, as pointed out in Chapter II, the particles,  $P$ , represent nodes, and the contacts between particles,  $C$ , represent branches in the deformation retract. The genus is given by equation (4), as there is only one separate part, the sinter body itself. The one can be neglected as the quantity  $C - P \gg 1$ . If unit volume of the sinter structure is considered, equation (5) is obtained.

$$G_V = C_V - P_V \quad (5)$$

where  $G_V$ ,  $C_V$  and  $P_V$  are the genus per unit volume, number of contacts per unit volume and number of particles per unit volume, respectively.\*

Multiplying equation (5) on the right side by  $P_V/P_V$  yields

$$G_V = P_V \left( \frac{C_V}{P_V} - 1 \right) \quad (6)$$

When both sides of this equation are divided by  $\rho$ , the density of the material under consideration, an expression for the genus per unit mass,  $G_\rho$ , is obtained.

$$G_\rho = P_\rho \left( \frac{C_\rho}{P_\rho} - 1 \right) \quad (7)$$

where  $P_\rho$  is the number of particles per unit mass. The value of  $P_\rho$  for a single size fraction of spherical particles is given by

$$P_\rho = \left[ \frac{4\pi}{3} \left( \frac{\bar{D}}{2} \right)^3 \rho_{th} \right]^{-1} \quad (8)$$

where  $\bar{D}$  is the average diameter of the particles and  $\rho_{th}$  is the theoretical density of the material under consideration. The number

---

\*The topological properties are considered on a unit volume or a unit mass basis throughout the course of this work so that the topological properties of different structures can be compared.



of contacts per particle,  $C_p/P_p$ , is equal to the average number of branches per node in the network,  $\overline{b/n}$ .

When individual particles are distinguishable and before channel closure begins,  $\overline{b/n}$  can be determined from the serial sections through the sinter body by counting the number of contacts per particle.

Particles are counted until the resulting value of  $\overline{b/n}$  is within the 95 per cent confidence limits for 5 per cent error, according to the Central Limit Theorem of statistical analysis [24]. The particles counted are chosen at random throughout the volume of the sinter structure represented in the serial sections. This is done in order to ensure that the value obtained for  $\overline{b/n}$  is representative of the bulk sinter structure and is not influenced by local inhomogenieties in the particle stacking.

If the number of particles per unit mass,  $P_p$ , is also known,  $C_p$  can be calculated using the equation

$$C_p = P_p (\overline{b/n} - 1) \quad (9)$$

where  $\overline{b/n}$  is the average number of contacts per particle (branches per node).

If  $P_p$  cannot be determined, either because the particles are irregular in shape or because the particles are not uniform in size, then the genus cannot be determined by the preceding method. In this case a method, presented in the latter part of this chapter, can be used (see Section 4.9).

#### 4.3 Determination of the Genus of Sinter Structures After Kronsbein, et al.

Kronsbein, et al. [5] developed a method which allows the determination of the genus of sintered structures having no multiple connectivity of the void space on a given microsection. The method is based on the construction of a network with the same topological properties as the deformation retract of the void space of that portion of the sinter structure that is analyzed. The method of Kronsbein, et al. can also be applied to the material space of a sinter structure when this space is simply connected on a given microsection. The void space is considered throughout the remainder of this section for the sake of illustration.

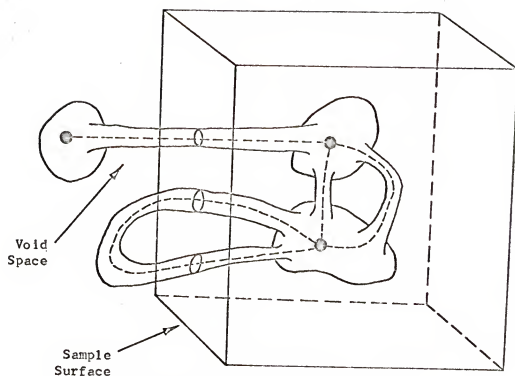
The method of Kronsbein, et al. yields the maximum limit of the genus per unit volume,  $G_v^{\max}$ , and not the actual value of genus per unit volume. The actual value of genus per unit volume could be determined if a sample of infinite extent could be analyzed so that branches crossing the surface of the sample would have essentially negligible effect on the value obtained. Since only a small sample can actually be analyzed, the contribution of branches crossing the surface of the sample can be significant, and therefore must be taken into account. This can be done by experimentally determining a maximum and a minimum limit for the genus per unit volume. A procedure which allows the determination of the minimum limit is presented in Section 4.5.

That the procedure of Kronsbein, et al., presented in this section, yields the maximum limit of genus per unit volume, can be seen from the following.

Consider the void space configuration illustrated in Figure 10a. The deformation retract is shown by the dotted line. If the sample which is analyzed has the boundaries shown in Figure 10a, then three branches cross the sample surface. These branches are labeled with numbers in Figure 10b, which again shows the deformation retract. The branch labeled 1 does not contribute to the genus of the void space, while the branches labeled 2 and 3 do contribute.

Kronsbein, et al. assume that all branches which cross the surface of the sample are attached to an external node, as illustrated in Figure 10c. In this case, the branch labeled 1 contributes one to the genus of the void space. Thus, the value of genus per unit volume obtained when it is assumed that all branches which cross the surface of the sample are attached to the external node is greater than or equal to the actual value of genus per unit volume.

If all branches which cross the surface of the sample are connected in the portion of the sinter body external to the sample, as the branches labeled 2 and 3 in Figure 10 are, then the experimentally obtained maximum limit of genus per unit volume is still greater than the actual value of genus per unit volume. This is because the circuits intersected by the surface of the sample are not contained entirely within the sample, and hence they each actually contribute less than one to the genus of the structure contained inside the sample. During the experimental procedure, however, they are all attached to the external node, and so each is assumed to contribute one to the genus of the structure contained inside the sample. As a result, the value of genus per unit volume



Dotted Line = Deformation Retract

(a)

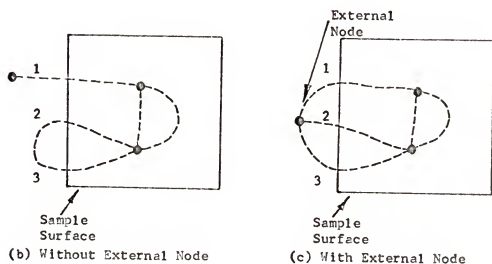


Figure 10. Illustration of the effect of the external node on the deformation retract.

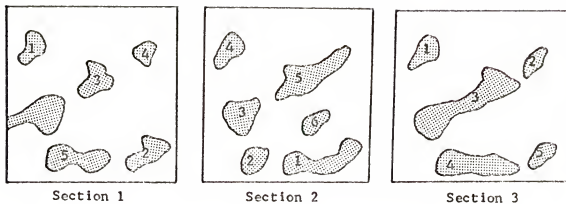
obtained by the procedure presented in this section is greater than or equal to the actual value of genus per unit volume, and hence is referred to as the maximum limit of genus per unit volume. The value of  $G_v^{\max}$  can be equal to the actual value of genus per unit volume if the structure has a genus of zero.

A network which is topologically equivalent to the deformation retract is constructed from serial sections through the sinter body according to the following procedure. A square area is drawn on the photomicrograph of each serial section. The areas are all the same size, and each lies directly below the one above. The first and last serial sections and the perimeters of the constructed areas enclose a volume of the structure so that all the surfaces of the volume form  $90^\circ$  angles with adjacent surfaces. It is not necessary that the area analyzed on each section be square; a circular area can be used as well as an area of any other shape. It is only necessary that the magnitude of the area be known, and that the perimeters of the areas analyzed form a cylinder passing through the sinter structure. When these conditions are satisfied, the volume of material analyzed can be determined. This volume must be known in order to determine the magnitude of the topological properties on a per-unit volume basis. Right circular and right square cylinders were used for sample shapes during the course of this work. The size of the area is chosen so that a number of independent areas of the void space are enclosed. It is desirable that approximately 150 areas of the void space be enclosed for the reasons discussed in Section 6.13.

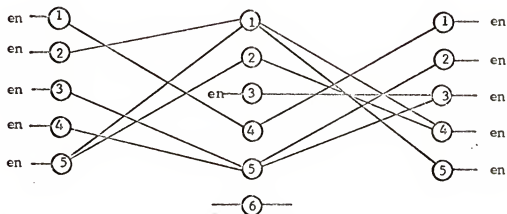
Each independent area of the void space which lies entirely within the area constructed on each section is arbitrarily numbered. This is done for each section which is analyzed. Each numbered area on each section is assumed to represent a node in the deformation retract. Recall from Chapter II that the presence of dummy nodes in a network has no effect on the value of the connectivity of the network.

An array of points representing these nodes is then constructed, as shown in Figure 11b, for the three corresponding serial sections shown in Figure 11a. The nodes are connected by a branch if a continuous path exists in the void space between them, as shown in Figure 11. When the void space contacts the surface of the portion of the sinter body being analyzed, a branch to the external node is formed, denoted  $e_n$  in Figure 11.

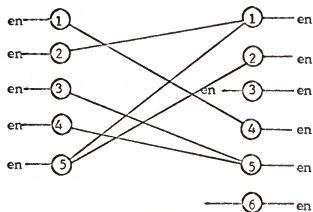
As each successive serial section is considered, the connectivity of the deformation retract up to and including that section is determined. As an example, consider again Figure 11. After the first two sections have been analyzed, the node-branch network shown in Figure 11c is generated. This network consists of 18 branches, 11 interior nodes, one external node and one separate part, the network itself. Putting these values in equation (4) gives a value of seven for the genus of the portion of the void space between the first two sections. This value of genus divided by the volume contained between the first two sections is not representative of the genus per unit volume of the bulk sinter structure. The procedure by which such a representative value is obtained is presented in the latter part of this section.



(a)



(b)



(c)

Figure 11. Three schematic serial sections and the corresponding node-branch network.

When the first three sections are considered, the node-branch network shown in Figure 11b is generated. The node labeled 6 on section 2 is not connected to the external node; hence, it represents an isolated separate part of the void space. The network consists of 24 branches and 17 nodes, 16 of which are internal nodes. This includes the node which represents a separate part mentioned above. The seventeenth node is the external node. There are two separate parts, one being the multiply connected portion of the node-branch network and the other the simply connected void represented by node 6 of section 2.

On applying equation (2), it is found that

$$G = 24 - 17 + 2 = 9$$

Thus, the maximum value of the genus of that portion of the void space between the three sections of Figure 11 is 9.

This procedure is repeated as each successive serial section is considered. The value of genus obtained for the sample after each serial section is added to the sample is referred to as the maximum value of the cumulative genus.

During the preparation of each serial section, the thickness of sample removed is measured so that the volume of material analyzed per section can be calculated. This volume is determined from the thickness and the area of each section that is analyzed.

The maximum limit of genus per unit volume,  $G_v^{\max}$ , for a given sinter structure can be determined in the following way. The maximum value of cumulative genus for each section is first divided by the corresponding volume of material analyzed. The resulting



value is referred to as the maximum value of cumulative genus per unit volume. These values are then plotted against the corresponding section number. The resulting curve approaches zero slope after a number of sections have been analyzed. The position on the ordinate of the zero slope line through the data points gives the maximum limit of genus per unit volume for the material being analyzed. Some experimental plots are shown in Figure 59.

#### 4.4 Determination of the Number of Separate Parts per Unit Volume

A procedure similar to that presented in the preceding section is used to determine the number of separate parts per unit volume. The total number of separate parts contained in the sample after each section has been analyzed is referred to as the cumulative number of separate parts. Each of these values is divided by the corresponding value of volume of material analyzed. The resulting values are referred to as cumulative number of separate parts per unit volume. These values are then plotted against the section number, and the resulting curve approaches zero slope after a number of sections have been analyzed. The position on the ordinate of the zero slope line through the data points gives the desired value of separate parts per unit volume for the material being analyzed.

#### 4.5 General Features of an Improved Method for the Determination of the Genus of Sinter Structures

The requirement that the node-branch network be constructed makes the method of analysis presented in Section 4.3 time consuming, especially when 100 to 200 void areas are included in the area of each serial section that is analyzed. It is desirable to analyze

such a large area because the difference between the experimentally determined value of  $G_v^{\max}$  and the actual value of genus per unit volume decreases as the area analyzed on each section is increased. This is shown in Appendix 1.

The long time necessary to determine the topological properties by the method of analysis presented in Section 4.3 prompted the development of a less time-consuming method of analysis, referred to as Method II.

Method II is applicable to the same range of structures as the method of Kronsbein, et al.; that is to say, only a space, solid or void, which is simply connected on a given microsection can be analyzed. A void space which is simply connected on a given serial section is referred to throughout this section to illustrate the procedure.

As in the method of Kronsbein, et al., a square area is drawn on the photomicrograph of each serial section so that each area is directly below the preceding one. The size of the area considered should be such that 100 to 200 void areas are enclosed. The analysis can then be carried out relatively rapidly with an acceptably small difference between the experimentally determined value of  $G_v^{\max}$  and the actual value of genus per unit volume (see Appendix 1).

Up to this point, only a maximum limit for the actual value of genus per unit volume has been considered. It is also possible to obtain a minimum limit for this parameter. Recall that the maximum limit is found by determining the genus per unit volume after assuming that all channels of the void network which cross the

surface of the sample are connected to the external node. The minimum limit for the genus per unit volume is obtained when it is assumed that all channels which cross the surface of the sample are capped at the surface. That this does give a lower limit can be seen from the following.

In general, some branches which cross the surface of the sample should contribute to the genus, as pointed out in Section 4.3. Since this contribution is removed by capping these branches at the sample surface, the value of genus per unit volume obtained will be less than or equal to the actual value of the genus per unit volume of the sinter body. The experimentally determined minimum limit of the genus per unit volume can be equal to the actual value if none of the branches which cross the surface of the sample are connected to each other in the portion of the sinter body exterior to the sample. These conditions can be expressed as

$$G_V^{\min} \leq G_V \leq G_V^{\max} \quad (10)$$

where  $G_V^{\max}$  and  $G_V^{\min}$  are the maximum and minimum limits of the genus per unit volume, respectively, and  $G_V$  is the actual value of genus per unit volume.

Method II allows the determination of the maximum and minimum limits of the genus per unit volume and the number of separate parts per unit volume. Circuits in the void or material space and separate parts of the void-solid interface can be detected by considering each serial section through the structure in succession. A labeling procedure, presented in Section 4.5.1, allows this to be done simply by noting all changes which occur as each successive serial section is compared to the preceding one. It is therefore

unnecessary to check serial sections which were previously considered in order to detect the presence of circuits or separate parts in the structure. It also becomes unnecessary to construct the actual node-branch network corresponding to the deformation retract, as is the case when the method of Kronsbein, et al. is used. Kronsbein, et al. [5] also point out that matrix algebra can be employed to determine the connectivity and number of separate parts of a network, making it unnecessary to construct the deformation retract. This technique, however, is no less time consuming than the method presented in this section, and therefore was not employed during the course of this work.

#### 4.5.1 Labeling Procedure

In this section, a labeling procedure is presented which allows the determination of the cumulative values of genus and number of separate parts as each serial section is analyzed. The void space will be referred to throughout this section; however, this procedure can be applied to either space, void or material as long as the space is simply connected on any given microsection.

Four different labels for void areas are necessary in order to monitor all changes which can occur in the void space as successive pairs of serial sections are analyzed. These labels and their meanings are listed in Table 1. There are 11 events which must be monitored as successive pairs of serial sections are considered. These events and the labeling procedure which must be employed as each event is encountered are presented schematically in Table 2. These 11 events are described in detail in the remainder of this section.

Table 1. Labels and their meanings.






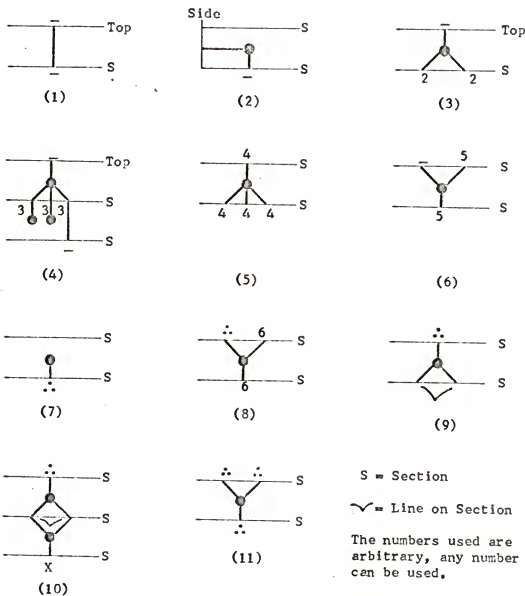
<u>Void Area Labels</u>	<u>Meaning</u>
 (dash)	Channel attached to the external node at both ends.
 (N = number)	Channels which are incident on the external node at the end which passes through the bottom of the sample and on an internal node at the other end.
 (three dots)	New channels. The end which passes through the bottom of the sample is incident on the external node. The other end of a channel so labeled ends within the sample.
 (line on section)	The void areas which are connected originated at a new channel and are incident on the external node through the bottom of the sample.
	A channel labeled X is incident at one end on an n-hole torus ( $n = 1, 2, 3, \dots$ ) and at the other end on the external node.

Table 2. Events which must be noted as successive serial sections are considered and the labels associated with each of these events. The numbers in parentheses refer to the 11 steps presented in the text.



The method of analysis presented in the following sections employs the labeling procedure presented in this section in order to determine maximum and minimum values of the cumulative genus.

The first serial section is referred to as the top of the sample. The sides of the sample are those surfaces which lie at  $90^\circ$  angles to the top surface and which are established by the perimeter of the area analyzed on each section.

The labeling procedure consists of the following steps.

1. All void areas which pass through the top of the sample are labeled with the same symbol or color. As these void areas are followed to the second, third and successive sections, they are labeled with the same symbol or color. A dash (-) was used to label these channels during the course of this work.

As a result of this procedure, all void areas on any section which are connected to the external node are labeled as such. This information is carried from section to section by means of the labeling procedure, and it is unnecessary to trace back through previously analyzed sections to determine if void areas are connected to the external node.

2. Void areas which pass through the sides of the sample are labeled with the same symbol or color as those in 1 above as they are also incident on the external node.

3. All void areas which result from the splitting, or branching as it will be referred to, of a channel connected to the external node during comparison of successive serial sections are labeled with a number. A different number is used for each event of this type.

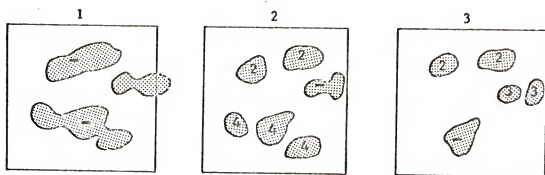
Schematic examples of such branching events are shown in Figure 12. One void area branches into three void areas between sections 1 and 2. These three void areas are labeled 4 on section 2. Another void area branches into two void areas which are labeled 2 on section 2. One void area comes in through the side of the sample between sections 1 and 2 and then branches into the two void areas labeled 3 on section 3.

All void areas which result from a given branching event are labeled with the same number. Void areas resulting from different branching events are labeled with different numbers. As a result, all numbered void areas are incident on an internal node at one end and on the external node through the bottom of the sample at the other end. All channels labeled (-) are incident on the external node at both ends.

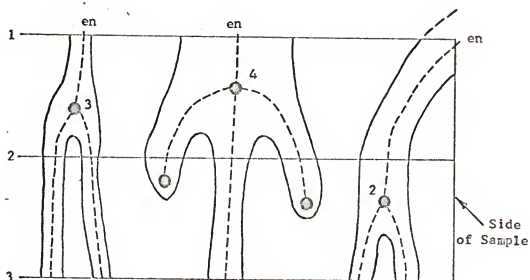
4. If a void area branches into two or more void areas and at a later point in the analysis all but one of these void areas end, then the remaining void area must be relabeled with the symbol or color indicating a branch incident on the external node (-).

This is because such a void area is not incident on an internal node, it is only incident on the external node. The portion of the void space designated 4 in Figure 12b is an illustration of this. The superimposed node in this portion of the void space is a dummy node as two of the branches which are incident on this node end. Thus, this portion of the void space is equivalent to one branch, incident at the top of the sample on the external node and passing through section 3. The labeling of this portion of the void space on section 3 by a (-) indicates this.





(a)



en = External Node

----- Deformation Retract

(b)

Figure 12. Illustration of branching events.

5. All channels which are the result of branching of a numbered void area are labeled with the same number as the void area from which they branched.

A joining event is the reverse of a branching event. For example, two branches join between sections 4 and 5 in Figure 21.

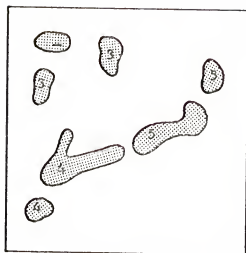
6. If a numbered void area joins a void area from the external node, the resulting void area is labeled with the number. If two or more numbered void areas join, the number of any of these areas can be used to label the resulting void areas.

For example, Figure 13a shows one void area from the external node. In Figure 13b, this void area has joined a void area labeled 3, and the resulting void area is labeled 3. Also, between these two serial sections void areas labeled 4 and 5 join, and the resulting void area is labeled 4. Note that 5 could also have been used.

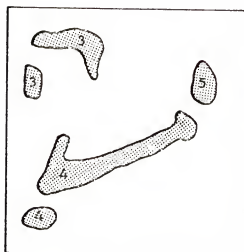
Another event which must be considered is the appearance of new channels during the analysis. For example, the void area labeled 6 on section 2 in Figure 11 appears between sections 1 and 2 and is referred to as a new channel.

7. New channels are labeled with a symbol or color different from that used for channels which enter the sample through the top or sides.

Three dots (..) were used during the course of this work, as in Figure 19. If a new channel ends without joining another part of the void space which is connected to the surface of the sample, then this new channel is a separate part of the void space. Thus, the labeling procedure allows separate parts to be monitored during the



(a)



(b)

Figure 13. Illustration of joining events.

analysis. For example, the void area labeled 6 on section 2 in Figure 11 is such a channel.

8. If a new channel joins another channel, the label of the latter channel is used to label the resulting channel.

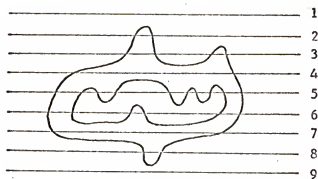
9. If a new channel branches, the resulting channels are connected with a line on each succeeding section.

An event of this type is shown schematically in Figure 14. The new channel shown in section 4 branches into five channels in section 5, all of which are connected by lines on section 5. These channels can undergo further branching, and each new channel is joined to the one from which it branched by a line on the respective section. If all channels resulting from the branching of a new channel end, then this new channel and its branches form a separate part. If one of the resulting channels joins part of the void space which is connected to the external node, then this new channel and its branches is not a separate part.

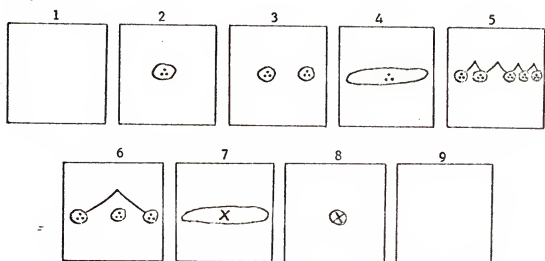
If a new channel branches and then at a later stage in the analysis the resulting channels join to form one channel and this channel then ends, the resulting separate part is multiply connected. The occurrence of such multiply connected separate parts can be detected as follows.

10. Any channels which are a result of the joining of channels which were formed by the branching of a new channel are so designated by a fourth symbol or color; an X was used during the course of this work. If the channel or channels so designated end, the presence of a multiply connected separate part is indicated.

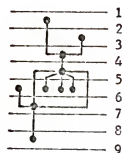
Serial Section



(a)



(b) Serial Sections



(c) Deformation Retract

Figure 14. Illustration of branching of a new channel.

An example of a multiply connected separate part is presented in Figure 14 with serial sections and the associated node-branch network. The proper labels are included on the serial sections. Multiple connectivity is established when the two previously connected channels in section 6 join between sections 6 and 7. It is not established that this portion of the void space is a separate part until the void area in section 7 ends, between sections 8 and 9.

11. If two or more new channels which are not previously connected join, the resulting channel is a new channel.

For example, two new channels join between sections 3 and 4 of Figure 14. The resulting channel in section 4 is therefore labeled as a new channel.

#### 4.5.2 Method II for the Determination of the Maximum Values of Cumulative Genus

When the labeling procedure presented in the previous section is combined with the method of analysis presented in this section, a maximum value of cumulative genus can be obtained as each successive serial section is considered.

The term  $i^{\text{th}}$  sample will refer to the volume of material enclosed by the first serial section, the surfaces established by the perimeters of the areas constructed on each section and by the serial section under consideration, the  $(i + 1)^{\text{th}}$  serial section. The first sample is actually contained between the first two serial sections as two serial sections must be considered before a volume of material is delineated. As a result, the  $(i + 1)^{\text{th}}$  serial section and the  $i^{\text{th}}$  sample correspond when the serial sections are counted from 1, as is done throughout the course of this work. The volume

of material analyzed, or the size of the sample, increases as each successive serial section is considered.

By determining the quantities defined below as each serial section is analyzed and applying equations (11), (12), (13) and (14), the maximum limit of the genus of the  $i^{\text{th}}$  sample,  $G_i^{\text{max}}$ , can be determined as the  $(i + 1)^{\text{th}}$  serial section is analyzed. From the values of  $G_i^{\text{max}}$ , referred to as cumulative values, a value can be determined which is representative of the genus per unit volume of the bulk structure. A method for doing this is presented in Section 4.6.

The values of the quantities defined below are obtained for the  $i^{\text{th}}$  sample by tabulating the changes in each of these quantities as successive serial sections are considered up to and including the  $(i + 1)^{\text{th}}$  serial section.

$b_i^t$   $\equiv$  Number of branches through the top of the  $i^{\text{th}}$  sample.

$b_i^b$   $\equiv$  Number of branches through the bottom of the  $i^{\text{th}}$  sample.

$b_i^s$   $\equiv$  Number of branches through the sides of the  $i^{\text{th}}$  sample.

$b_i^{e(\text{end})}$   $\equiv$  Number of branches incident on the external node which passes through the top and sides of the  $i^{\text{th}}$  sample and ends within the  $i^{\text{th}}$  sample.

$b_i^{(\text{end})}$   $\equiv$  Number of branches incident on internal nodes which ends within the  $i^{\text{th}}$  sample.

$n_{i,j}$   $\equiv$  Number of  $j$ -branch nodes ( $j = 3, 4, 5 \dots$ ) in the  $i^{\text{th}}$  sample (excluding the external node).

Examples of three-branch, four-branch and five-branch nodes are shown in Figure 15.

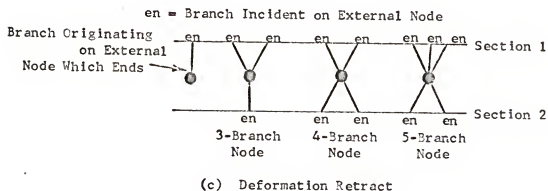
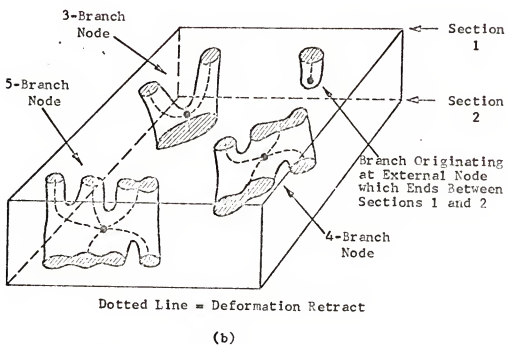
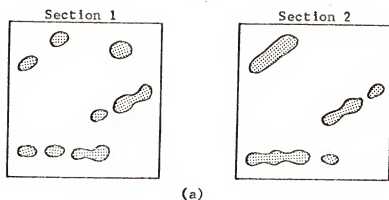


Figure 15. Illustration of several events which occur between serial sections.



The top of the  $i^{\text{th}}$  sample is the first serial section considered. Therefore, the value of  $b^t$  remains constant throughout the analysis. The bottom of the  $i^{\text{th}}$  sample is the  $(i + 1)^{\text{th}}$  serial section. The value of  $b_i^b$  varies randomly about a mean as successive serial sections are analyzed. The value of  $b_i^s$  generally increases as successive serial sections are analyzed. The value of  $b_i^{e(\text{end})}$  is equal to the number of channels incident on the external node (labeled -) which have ended at any point during the analysis.

The quantities defined below,  $b_i^e$ ,  $b_i$  and  $n_i$ , are expressed in terms of the measured quantities,  $b^t$ ,  $b_i^b$ ,  $b_i^s$ ,  $b_i^{e(\text{end})}$ ,  $b_i^{(\text{end})}$  and  $n_{i,j}$ , by equations (11), (12) and (13).

$b_i^e \equiv$  Number of branches incident on the external node for the  $i^{\text{th}}$  sample.

$b_i \equiv$  Number of internal branches (branches which do not contact the external node) in the  $i^{\text{th}}$  sample.

$n_i \equiv$  Number of nodes in the  $i^{\text{th}}$  sample (including the external node).

$$b_i^e = b^t + b_i^b + b_i^s - b_i^{e(\text{end})} \quad (11)$$

$$b_i = \left[ \sum_{j=3}^{j_{\text{max}}} j n_{i,j} \right] - [3 b_i^{(\text{end})}] \quad (12)$$

$$n_i = \sum_{j=3}^{j_{\text{max}}} n_i^j - b_i^{(\text{end})} + 1 \quad (13)$$

The order of the highest order node in the sample is  $j_{\text{max}}$ , where the highest order node is that node with the largest number of branches incident upon it.

The value of  $b_i^e$  generally increases as successive serial sections are considered.

A node is observed when a branching or joining event takes place between numbered void areas or between void areas incident on the sample surface (labeled -). This includes joining events between numbered void areas and void areas incident on the sample surface (labeled -).

The value of  $G_i^{\max}$  can be expressed in terms of  $b_i^e$ ,  $b_i$  and  $n_i$  as

$$G_i^{\max} = \frac{1}{2}(b_i + b_i^e) - n_i + 1 \quad (14)$$

This is equation (4) where

$$d_1 = \frac{1}{2}(b_i + b_i^e) \quad (15)$$

and

$$d_0 = n_i \quad (16)$$

The factor  $\frac{1}{2}$  is present because all branches are counted twice during consideration of the serial sections, once for each of the two nodes upon which they are incident.

Examples of some of the quantities mentioned above will now be presented. Two schematic serial sections are shown in Figure 15a. The void space between these serial sections is shown in Figure 15b, with the deformation retract superimposed. The deformation retract is shown again in Figure 15c.

A branch which originates at the external node and ends between the two sections is shown along with examples of three-branch, four-branch and five-branch nodes. If a third section were considered

and one of the branches through the second section ended between the second and third sections, this would be an example of a branch originating at an internal node which ends.

An example of a branch which comes in from the side of the sample and then ends is shown in Figure 16. The void area indicated by the arrow in the schematic serial sections of Figure 16a moves into the sample and then ends. After the third section has been considered, both ends of this branch are incident on the external node, as shown in Figure 16b. Therefore, both  $b_i^s$  and  $b_i^b$  are increased by one when the third section is considered. This increases  $b_i^e$  by two, which increases  $G_i^{\max}$  by one [see equation (14)]. When the fourth section is considered, the circuit on the external node shown in Figure 16b no longer exists, as shown in Figure 16c. This decreases  $b_i^b$  by one and increases  $b_i^{e(\text{end})}$  by one. Thus,  $b_i^e$  is decreased by two. Therefore, when the branch ends between the third and fourth sections,  $G_i^{\max}$  is decreased by one [see equation (14)]. This illustrates the fact that the total change in  $G_i^{\max}$  produced by a branch incident on the external node which passes through the side or top of the sample and then ends is zero.

In equation (14), the number of separate parts is given by the last term, 1. This is because separate parts are counted separately during the analysis so the only separate part which must be included in equation (14) is the multiply connected part of the network.

This was done during the course of this work because only one separate part in the 1187 observed in all the sinter structures analyzed was multiply connected. This observation is supported by

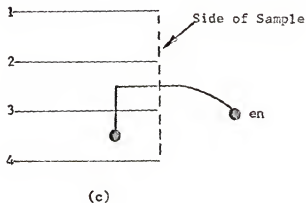
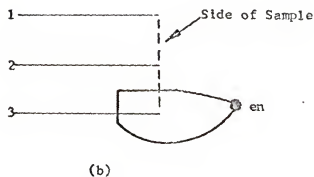
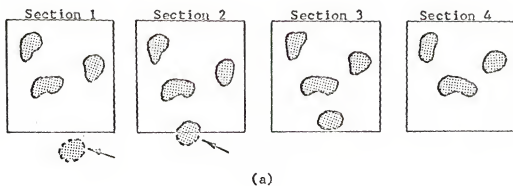


Figure 16. Illustration of a branch which comes in from the side of the sample and then ends.

the results of a computer model for the sintering process developed by Steele [3], which indicates that the probability of isolating multiply connected parts of the void space is small. The results of this computer model are presented in Section 6.7.

When the number of simply connected, isolated separate parts is not included in the value of  $n_i$ , equation (14) is correct, with the value of one for the number of separate parts,  $N$ . This is because if the number of simply connected separate parts is included in  $n_i$  as well as in  $N$ , the value of genus is not changed, as indicated by equation (2). Thus, if the number of simply connected separate parts is not included in  $n_i$  and  $N$ , as is done here, the resulting value of genus is the correct value.

Equation (13) has three terms on the right side. The first term gives the number of internal nodes in the network, and the last term takes the external node into account. The second term on the right side of equation (13) and the last term on the right side of equation (12) change the values of  $b_i$  and  $n_i$ , respectively, so that when branches incident on internal nodes end between sections, equation (14) still gives the correct value of  $G_i^{\max}$ . This is illustrated by means of the following example.

Consider the node-branch network shown in Figure 17. According to equation (14),  $G_i^{\max}$  of the network in Figure 17a is

$$G_i^{\max} = \frac{1}{2}(3 + 3) - 2 + 1 = 2$$

When the third section is included, as shown in Figure 17b, one of the two branches which crosses the second section has ended. As a

Section  
Numbers

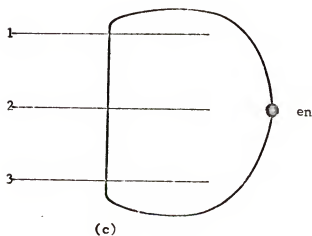
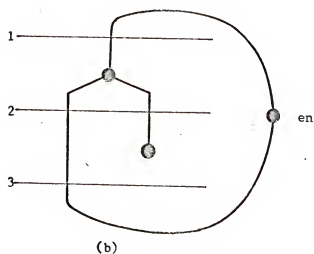
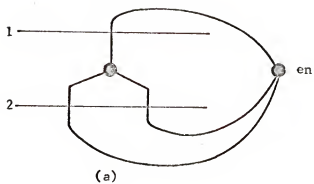


Figure 17. Illustration of a branch ending which is incident on an internal node.

result, according to equation (12),

$$b_1 = 3(1) - 3(1)$$

$$b_1 = 0$$

The three-branch node, previously tabulated between the first two sections and contributing the first term on the right side of the above equation, no longer exists as one of its branches has ended. The effect of this event on  $b_1$  is taken into account by the second term on the right side of equation (12) which, for this example, is the second term on the right side of the above equation. When the branch ends between the second and third sections, the number of nodes is also decreased by one. This is taken into account by the second term on the right side of equation (13), which decreases  $n_1$  by one for each branch which ends. Equation (13), when applied to Figure 17b, gives

$$n_1 = 1 - 1 + 1 = 1$$

The fact that  $b_1$  is zero and  $n_1$  is one indicates that the network is equivalent to the one shown in Figure 17c. This is true because the node present in Figure 17b is a two-branch node and is therefore a dummy node.

Note that  $b_1^e$  is two after the third section has been considered, as shown in Figure 17b. Putting these values of  $b_1$ ,  $b_1^e$  and  $n_1$  in equation (14) gives

$$G_1^{\max} = \frac{1}{2}(0 + 2) - 1 + 1 = 1$$

That this is correct is apparent from Figures 17b and 17c.

When a branch from a higher order node ( $j > 3$ ) ends, the effect on  $b_1$  and  $n_1$  is correctly given by the second term on the right side of equations (12) and (13), respectively. This is because whenever a branch from a node of any order ends, the effect on  $G_1^{\max}$  is the same as if a branch from a three-branch node had ended. This is a result of the fact that a node of order  $j$  ( $j = 3, 4, 5 \dots$ ) is equivalent to  $j - 2$  three-branch nodes.

In Figure 18, a five-branch node is shown to be equivalent to  $5 - 2 = 3$ , three-branch nodes. A five-branch node is shown in Figure 18a. In Figure 18b, a node and a branch have been added to give one four-branch and one three-branch node. Because one node and one branch have been added,  $G_1^{\max}$  is not changed as the quantity  $(b_1 - n_1)$  is unchanged. In Figure 18c, another branch and node have been added to give three three-branch nodes. Again, as one node and one branch have been added,  $G_1^{\max}$  remains unchanged.

From this it is apparent that if one of the branches passing through section 2 in Figure 18a ends, it is equivalent to removing one three-branch node from the network. The factor of three in the second term on the right side of equation (12) is a result of this fact. This term in equation (12) indicates that whenever a branch incident on an internal node ends, a three-branch node, and consequently three half-branches, are removed from the network. The second term on the right side of equation (13) takes into account the fact that a node is also removed by this event.

The effect of new channels on the values of  $G_1^{\max}$  will now be considered. The second serial section in Figure 19b illustrates



Section  
Numbers

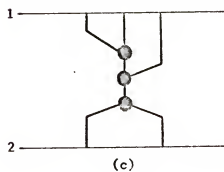
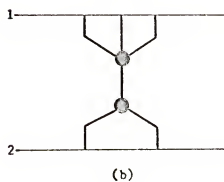
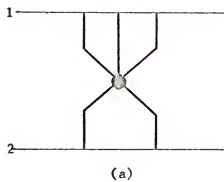


Figure 18. Illustration of the equivalence of a five-branch and three three-branch nodes.

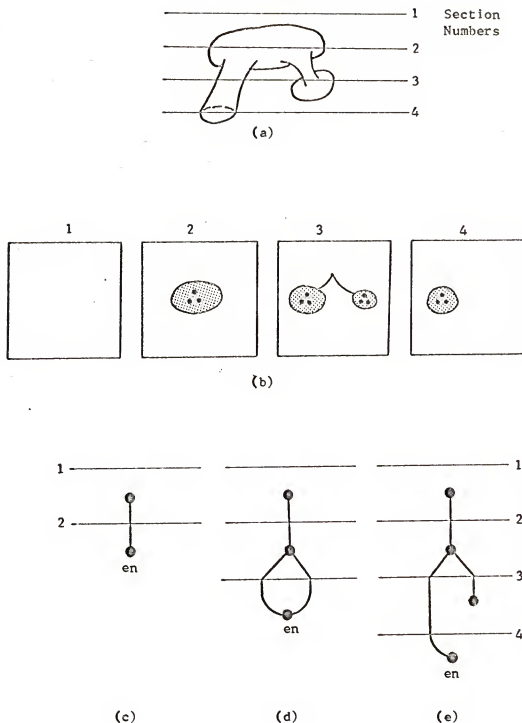


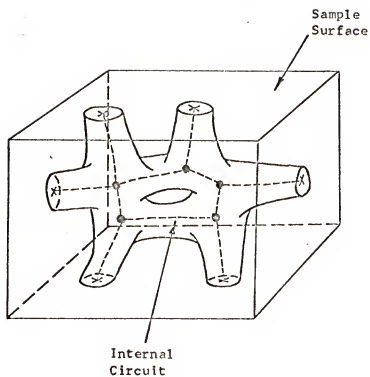
Figure 19. Illustration of a new channel which branches with one branch ending on a subsequent section.

the appearance of a new channel in the void space. The appearance of a new channel contributes nothing to the value of  $G_i^{\max}$ , as is indicated by the node-branch network shown in Figure 19c. If a new channel branches, as the new channel shown in Figures 19a and 19b does between the second and third sections, then  $G_i^{\max}$  is increased by one. This is apparent from the node-branch network shown in Figure 19d. This is accounted for by adding two to the value of  $b_i^b$  whenever a new channel branches. If one of these branches ends at a later point in the analysis, as indicated in Figures 19a and 19b, then two must be subtracted from the value of  $b_i^b$ . This produces a decrease in  $G_i^{\max}$  of one. That  $G_i^{\max}$  is decreased by one can be seen from the node-branch networks shown in Figures 19d and 19e. The configuration shown in Figure 19e forms no circuit with the external node, and thus does not contribute to  $G_i^{\max}$ .

This procedure yields the maximum limit of the cumulative genus,  $G_i^{\max}$ , as each successive serial section is analyzed. It is unnecessary to consider any serial sections previously analyzed as all necessary information from these sections is contained in the cumulative quantities,  $b_i^e$ ,  $b_i$  and  $n_i$ . Therefore, only two serial sections are considered at any one time during the analysis.

#### 4.5.3 Determination of the Minimum Values of Cumulative Genus

The minimum limit for the genus of a sinter structure is the value obtained when it is assumed that all channels which cross the surface of the sample analyzed are capped at the surface of the sample. This is illustrated schematically in Figure 20. There is



X = Caps

Figure 20. Illustration of capped branches at the sample surface during determination of the minimum limit of the genus.

no external node in this case. Contributions to  $G_1^{\min}$  come exclusively from circuits in the void space which are interior to the surface of the sample. A schematic example of such an interior circuit is shown in Figure 20; there is one circuit in the superimposed node-branch network. An example of a circuit which is not interior to the sample is shown in Figure 19d. Without the external node, this circuit would not be present.

The number of internal circuits in the  $i^{\text{th}}$  sample is equal to the value of  $G_1^{\min}$ . The values of  $G_1^{\min}$  were determined during the course of this work by noting the number of internal circuits formed as each serial section is analyzed and taking the sum of these values for all serial sections up to and including the one under consideration, the  $(i + 1)^{\text{th}}$  serial section. Internal circuits in the void space are easily detected by the following method based on the labeling procedure presented previously. This analysis is carried out simultaneously with the analysis to determine the values of  $G_1^{\max}$ .

As consecutive serial sections are considered, any two channels which join will produce an increase of one in  $G_1^{\min}$  if they are connected by some other path through the network. This is illustrated in Figure 21. When channels from the surface of the sample join, as in Figure 21a,  $G_1^{\min}$  is not changed. This is because these channels are considered to be capped at the surface of the sample, and hence are not connected by any other path through the void space. As a result, no circuit is formed in the network when these channels join.

In Figure 21b, the channels which join between sections 4 and 5 are joined by another path through the network; therefore, this

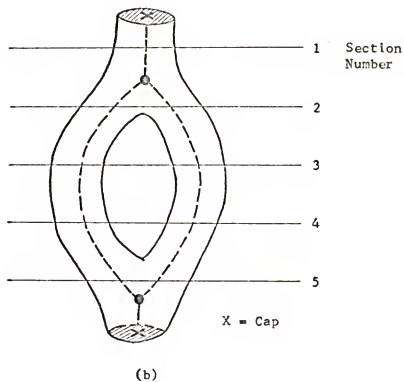
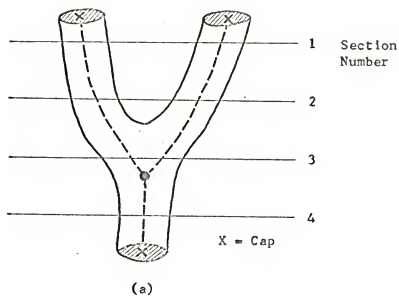
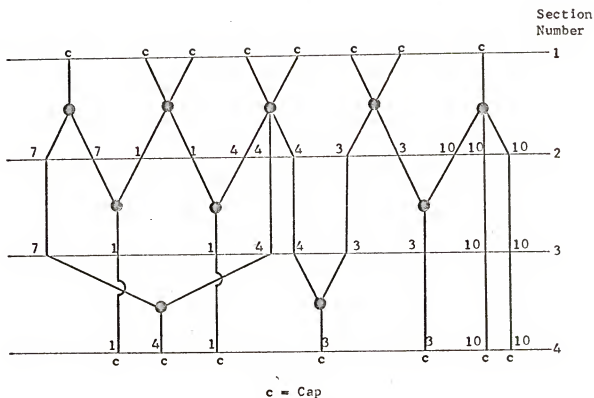


Figure 21. Illustration of the effect of branching and joining events on the value of  $C_1^{\min}$ .

event increases  $G_i^{\min}$  by one because a circuit is formed in the network.

As an actual sinter structure is analyzed, the previously described labeling procedure allows circuits in the void space to be monitored as each section is analyzed as follows. During the analysis, numbered channels will join other numbered channels. The numbers of the channels which join must either be the same or different. If the numbers are the same, then the labeling procedure assures that the channels are joined in some previously analyzed portion of the sample. This joining event thus completes a circuit in the void space, and therefore  $G_i^{\min}$  is increased by one. If the channels which join have different numbers, then the joining event is recorded as follows.

A new linear graph (not to be confused with the deformation retract of the structure under consideration) is established by writing the numbers of the channels and then connecting them with a line. In order to avoid confusing this new linear graph with the linear graph which represents the deformation retract of the structure under consideration, this new graph is referred to as the "subnetwork graph." Examples of such subnetwork graphs are shown in Figures 22b and 22c for the deformation retract shown in Figure 22a. If the number of either of the channels which joined is previously recorded in the subnetwork graph, then only the number of the channel which was not in the subnetwork graph is recorded and connected to the number of the channel already present. Thus, any number only appears once in the subnetwork graph. The event of



(a) Deformation Retract

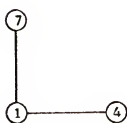
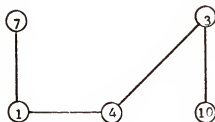
(b) Subnetwork Graph  
After Section 3(c) Subnetwork Graph  
After Section 4

Figure 22. Illustration of the subnetwork graph associated with the determination of the values of  $C_1^{\min}$ .



two channels joining, only one of which is recorded in the subnetwork graph, does not change  $G_1^{\min}$  as no other path exists between two such channels. This joining event, however, establishes such a path and the line in the subnetwork graph between the numbers of these two channels indicates this. The event of two channels joining which are already indicated as being joined in the subnetwork graph increases  $G_1^{\min}$  by one as these channels are joined previously, and the event under consideration establishes a circuit in the void space. Such an event is not recorded again in the subnetwork graph as it is not necessary to connect any pair of numbers with more than one line. In general, if two channels with different numbers join and if any path connecting them can be found in the subnetwork graph, then this event increases  $G_1^{\min}$  by one.

For example, consider the node-branch network shown in Figure 22a. The channel labels are indicated next to each of the branches where they intersect the serial sections. Note that between sections 2 and 3 a channel labeled 7 joins a channel labeled 1, a channel labeled 1 joins a channel labeled 4 and a channel labeled 3 joins a channel labeled 10. These events are indicated in the subnetwork graph shown in Figure 22b, which shows 1 joined to 4 and 7 and 3 joined to 10. When section 4 is considered, channels labeled 4 and 7 join and channels labeled 3 and 4 join. This is indicated in the subnetwork graph shown in Figure 22c, which is the same graph shown in Figure 22b except 3 and 4 are also joined.

When the channels labeled 4 and 7 join,  $G_1^{\min}$  is increased by one because these channels are joined in the subnetwork graph by a

path through 1. It is not necessary to join 4 and 7 in the sub-network graph as they are already joined by the path through 1. When the channels labeled 3 and 4 join,  $G_1^{\min}$  is not changed as there is no path in the subnetwork graph which connects these channels.

As each serial section is analyzed, the change in  $G_1^{\min}$  produced by the events described above are tabulated. Each value of  $G_1^{\min}$  is determined by adding the tabulated change in  $G_1^{\min}$  to the preceding value of  $G_1^{\min}$ . The values of  $G_1^{\min}$  are then used to determine the minimum limit of genus per unit volume,  $G_v^{\min}$ , according to the procedure presented in Section 4.6.

#### 4.5.4 An Example Illustrating Method II for the Determination of the Maximum and Minimum Limits of the Cumulative Genus

An example of the application of Method II for the determination of values of  $G_1^{\max}$  and  $G_1^{\min}$  will now be presented using the three schematic serial sections shown in Figure 23a. Figure 23b shows the deformation retract for the first two sections.

During the analysis of an actual sinter structure, it is not necessary to construct the deformation retract. As indicated previously, it is only necessary to record each event as it is observed during the analysis. The node-branch networks are presented here in order to clarify the example.

When the first two sections are considered, the quantities defined in Section 4.6 have the following values: the number of branches through the top (section 1) of the first sample (between sections 1 and 2),  $b_1^t$ , is 10, and the number of branches through the bottom of the first sample (section 2),  $b_1^b$ , is 7. The two new

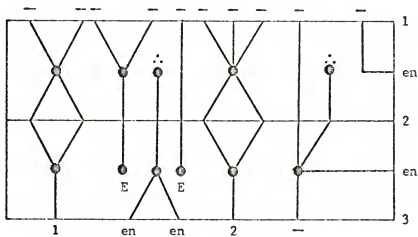
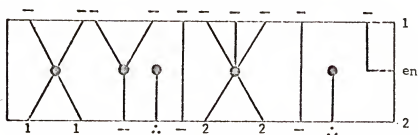
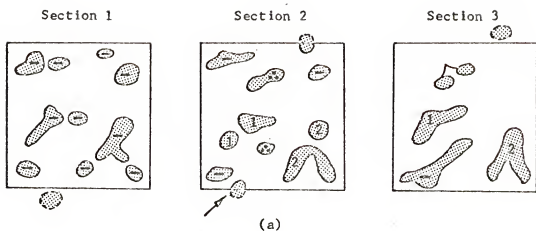


Figure 23. Three schematic serial sections and their deformation retracts used to illustrate Method II.

channels, designated  $\therefore$ , are not counted in  $b_1^b$ . The number of branches through the sides of the first sample,  $b_1^s$ , is 1. The channel indicated by the arrow in section 2 of Figure 23a is attached to the external node; however, it makes no circuit and so does not contribute to the genus. Therefore, it is not counted as a branch through the side of the sample and is not indicated in the node-branch network of Figure 23b.

The number of branches incident on the external node which passes through the top and sides of the first sample and ends within the first sample,  $b_1^{e(\text{end})}$ , is zero.

Therefore, according to equation (11), the number of branches incident on the external node for the first sample,  $b_1^e$ , is

$$b_1^e = 10 + 7 + 1 - 0 = 18$$

There is one three-branch, one four-branch and one five-branch node present in the first sample. Therefore, the values of  $n_{1,j}$  are one for  $j = 3, 4$  and  $5$  and zero for all other values of  $j$ . This can be seen from the node-branch network in Figure 23b.

The number of internal branches in the first sample,  $b_1$ , is given by equation (12).

$$b_1 = \left[ \sum_{j=3}^5 j n_{1,j} \right] = [3b_1^{(\text{end})}]$$

On substituting the values of  $n_{1,j}$  and  $b_1^{(\text{end})}$ , this becomes

$$b_1 = 3(1) + 4(1) + 5(1) - 0 = 12$$

The number of nodes in the first sample,  $n_1$ , is given by equation (13) where  $i = 1$  and  $j_{\text{max}} = 5$ . On substituting the values of

$n_{1,j}$  and  $b_1^{(end)}$ , this becomes

$$n_1 = 1 + 1 + 1 - 0 + 1 = 4$$

On substituting the above values in equation (14),  $G_1^{\max}$  is obtained

$$G_1^{\max} = \frac{1}{2}(12 + 18) - 4 + 1 = 12$$

Note that the value of  $G_1^{\min}$  is zero as no internal circuits can be present after only two sections have been considered.

When the third section is considered, the quantities defined in Section 4.6 have the following values. The number of branches through the top of the sample remains unchanged. The number of branches through the bottom of the second sample (section 3),  $b_2^b$ , is five. The number of branches through the sides of the second sample,  $b_2^s$ , is two, as can be seen from the node-branch network of Figure 23c. As each section is considered, the number of branches through the sides of the sample can be determined simply by adding the increase in the number of branches through the sides of the sample produced by adding this section to the total number of branches through the sides of the previous sample.

The number of branches incident on the external node which passes through the top and sides of the third sample and ends within the second sample,  $b_2^{e(end)}$ , is one. This quantity can be determined by adding the increment for a given serial section to the value for the previous sample, as for  $b_i^s$ .

According to equation (11), the number of branches incident on the external node for the second sample,  $b_2^e$ , is

$$b_2^e = 10 + 5 + 2 - 1 = 16$$

Three three-branch nodes are added to the network when the third section is analyzed. Thus, for the second sample,  $n_{2,3}$  is 4,  $n_{2,4}$  is 1 and  $n_{2,5}$  is 1. The value of  $n_{2,j}$  is zero for all other values of  $j$ .

The number of internal branches in the second sample,  $b_2$ , is given by equation (12) where  $i = 2$  and  $j_{\max} = 5$ . On substituting the values of  $n_{2,j}$  and  $b_2^{(\text{end})}$ , this becomes

$$b_2 = [3(4) + 4(1) + 5(1)] - [3(1)] = 18$$

The number of nodes in the second sample,  $n_2$ , is given by equation (13) where  $i = 2$  and  $j_{\max} = 5$ . On substituting the values of  $n_{2,j}$  and  $b_2^{(\text{end})}$ , this becomes

$$n_2 = 6 - 1 + 1 = 6$$

On substituting the above values in equation (14),  $G_2^{\max}$  is obtained

$$G_2^{\max} = \frac{1}{2}(18 + 16) - 6 + 1 = 12$$

Two channels labeled 1 and two channels labeled 2 join between sections 2 and 3. Each of these events increases  $G_1^{\min}$  by one. Thus, after section 3 has been analyzed,  $G_2^{\min}$  has a value of two.

This example illustrates the application of the procedure presented in Sections 4.5.2 and 4.5.3 to determine the values of  $G_1^{\max}$  and  $G_1^{\min}$ .

#### 4.6 Determination of $G_v^{\max}$ and $G_v^{\min}$ from the Values of $G_1^{\max}$ and $G_1^{\min}$

Two methods can be used to determine the values of  $G_v^{\max}$  and  $G_v^{\min}$  from the values of  $G_1^{\max}$  and  $G_1^{\min}$ . The first method, proposed

by Kronsbein, et al. [5] was presented in Section 4.3. The second method, proposed by Steele [3], is presented here (see Appendix 1).

If the structural features which produce the changes in  $G_i^{\max}$  and  $G_i^{\min}$  are uniformly distributed throughout the volume of material analyzed, then  $G_i^{\max}$  and  $G_i^{\min}$  will, on the average, change by an amount proportional to the volume between sections as each successive section is analyzed. This can be expressed as

$$\Delta G_i^{\max} = G_v^{\max} (\Delta V) \quad (17)$$

where  $\Delta G_i^{\max}$  is the change in the cumulative value of genus,  $G_v^{\max}$  is the value of genus per unit volume and  $\Delta V$  is the volume of material analyzed which is associated with  $\Delta G_i^{\max}$ . This equation can also be applied to  $G_i^{\min}$ . Dividing both sides of equation (17) by  $\Delta V$  gives

$$G_v^{\max} = \frac{\Delta G_i^{\max}}{\Delta V} \quad (18)$$

This equation indicates that  $G_v^{\max}$  or  $G_v^{\min}$  is equal to the slope of a plot of  $G_i^{\max}$  or  $G_i^{\min}$ , respectively, versus volume of material analyzed. The following example will illustrate this.

Consider the hypothetical node-branch network shown in Figure 24. Assume that the serial sections from which this network was obtained are represented by the horizontal lines in the figure. Assume further that the sections are equally spaced so that the volume of sample between sections is the same for all sections. The values of  $G_i^{\max}$  and  $G_i^{\min}$  presented in Table 3 were determined from this network.

Section  
Number

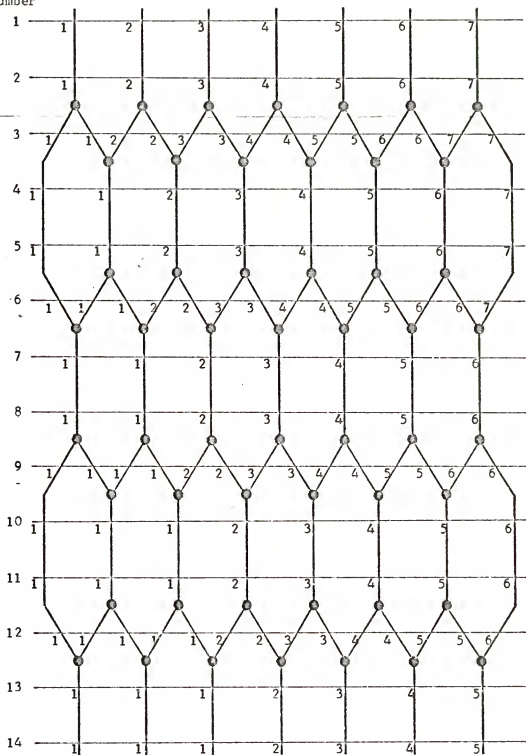


Figure 24. Hypothetical node-branch network.



Table 3. Data taken from the node-branch network of Figure 24.

Section Number (i)	$G_i^{\max}$	$\Delta G_i^{\max}$	$\sum \Delta G_i^{\max}$	$G_i^{\min}$	$\Delta G_i^{\min}$	$\sum \Delta G_i^{\min}$
2	7	0	0	0	0	0
3	14	7	7	0	0	0
4	14	0	7	0	0	0
5	14	0	7	0	0	0
6	20	6	13	0	0	0
7	20	0	13	7	7	7
8	20	0	13	7	0	7
9	27	7	20	7	0	7
10	27	0	20	13	6	13
11	27	0	20	13	0	13
12	33	6	26	13	0	13
13	33	0	26	20	7	20
14	33	0	26	20	0	20

If these values are plotted as a function of volume of material analyzed, or section number since the volume between sections is assumed constant, the curve shown in Figure 25a is obtained. The trend indicated in this plot continues as long as the network in Figure 24 goes on. Both  $G_i^{\max}$  and  $G_i^{\min}$  remain constant for three sections, and then the value increases by six or seven alternately. This produces a linear plot for both  $G_i^{\max}$  and  $G_i^{\min}$ , as is indicated by the lines through the points in Figure 25a. The plot for  $G_i^{\max}$  reaches linearity almost immediately; however, the plot for  $G_i^{\min}$  reaches linearity only after a number of sections have been analyzed. This is also a characteristic of plots obtained in the analysis of actual sinter structures (see Section 6.3). This behavior is a result of the fact that circuits in the void space cannot be detected until a number of sections have been analyzed.

In general, a plot of cumulative genus versus volume analyzed for an actual sinter structure will have less scatter than the plot shown in Figure 25a. This is because the events which produce changes in  $G_i^{\max}$  and  $G_i^{\min}$  are usually more uniformly distributed over the serial sections than is the case in Figure 24. Figures 62 to 64 are plots for sinter structures which exhibit little scatter. This scatter decreases as the area of each serial section which is analyzed increases. The plot shown in Figure 58 has considerable scatter as a result of the small number of channels in the area analyzed.

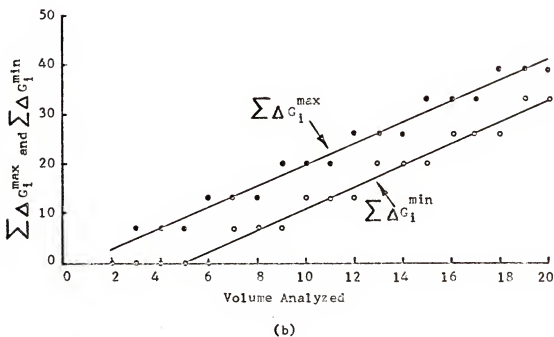
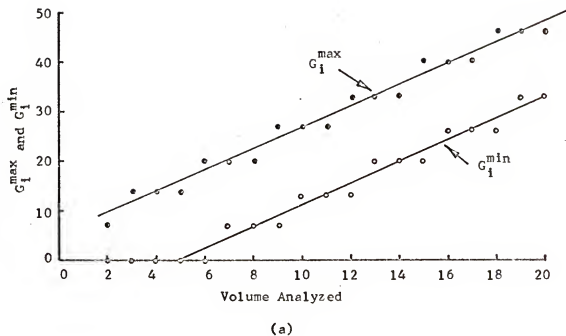


Figure 25. Cumulative plots for the network shown in Figure 24.

The curves in Figure 25a have the same slope. For an actual sinter structure, this will in general not be true. Usually  $G_v^{\max}$  will be greater than  $G_v^{\min}$  as a result of channels which pass through the sides of the sample. Since no branches pass through the sides of the sample in Figure 24, the plots of Figure 25a have the same slope. In general, the larger the surface-to-volume ratio of the sample (i.e., the smaller the sample size), the greater will be the difference of the slopes of the two curves. In order to place close limits on the actual value of the genus, it is important to minimize the difference caused by this effect. A compromise must therefore be reached between the shape and size of the sample analyzed and the time spent in the analysis. This will be considered further in Section 6.13.

#### 4.7 Determination of the Number of Separate Parts per Unit Volume from the Values of Cumulative Separate Parts

In order to determine the value of separate parts per unit volume,  $N_v$ , the same procedure as presented in the preceding section is followed. The cumulative values of separate parts are plotted against the volume of material analyzed. The slope of this plot is equal to  $N_v$ . This value is a minimum limit for  $N_v$  as only separate parts contained entirely within the volume analyzed are counted during the analysis. Separate parts which are intersected by the surfaces of the volume analyzed are not counted. If such separate parts were included, a maximum limit for  $N_v$  would be obtained. This surface effect is small as long as the area of each serial section that is analyzed is large. An area containing 150

to 200 channels was used for most samples analyzed during the course of this research. The surface effect error in the  $N_v$  values thus obtained is not greater than 11 per cent, according to the calculations in Appendix 2. This is considered further in Section 4.9.

#### 4.8 Method III

The fact that the parameter of interest in the determination of genus per unit volume is the slope of the plot of cumulative genus versus volume of material analyzed leads to a third, simpler method of analysis referred to as Method III.

In order to determine the slope of the plot of  $G_1^{\max}$  versus volume analyzed, it is only necessary to determine the change in  $G_1^{\max}$  as each successive serial section is considered, as is indicated by equation (18). This was pointed out and employed for Method II, presented in Section 4.5. Method II, however, is based on the application of equations (11) through (14) in order to determine  $G_1^{\max}$ . Before these equations can be used, the number of each type of event must be determined as each section is analyzed. The method of analysis presented in this section allows the determination of the changes in  $G_1^{\max}$  directly from the events which are observed as each section is analyzed. It then becomes unnecessary to employ any equations in order to determine the values of  $G_1^{\max}$ . As a result, Method III is more straightforward and less time consuming than Method II.

The procedure for the determination of the values of  $G_1^{\min}$ , presented in Section 4.5.3, is just such a method. It is unnecessary to use equations relating the number of the various types of events

and  $G_i^{\min}$ . Thus, this method for the determination of the values of  $G_i^{\min}$  is retained. Method III for the determination of the values of  $G_i^{\max}$  will be introduced by applying the method to the network of Figure 24.

Sections 1 and 2 of Figure 24 are the same; therefore, the change in  $G_i^{\max}$ ,  $\Delta G_i^{\max}$ , is zero for section 2, as indicated in Table 3. There are seven three-branch nodes between sections 2 and 3. These nodes all "branch down." This means that they are all oriented in such a way that two branches pass through the bottom of the sample and one branch passes through the preceding section. In this example, one branch from each node passes through section 2 and the remaining two branches pass through section 3.

Consider the three-branch node shown in Figure 26a which branches down. When the first two sections are considered, the network, shown in Figure 26b, has a value of  $G_i^{\max}$  of one, as one circuit is formed with the external node. When all three sections are considered, the network shown in Figure 26c has a value of  $G_2^{\max}$  of two, as two circuits are formed with the external node. Thus, the effect of adding one three-branch node which branches down to the node-branch network is to increase  $G_i^{\max}$  by one.

Since each three-branch node which branches down increases  $G_i^{\max}$  by one, the change in  $G_i^{\max}$ ,  $\Delta G_i^{\max}$ , between sections 2 and 3 of Figure 24 is +7, as indicated in Table 3. At this point in the analysis, no internal circuits have been formed in the network; hence, there is no change in  $G_i^{\min}$ . The branches in Figure 24 are labeled with numbers at the points where they cross each section according to the labeling procedure of Section 4.5.1.

Section  
Numbers

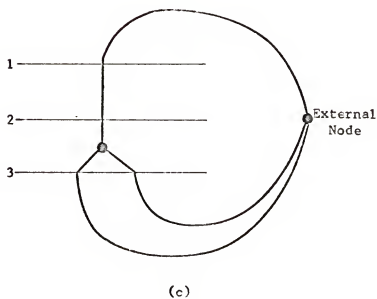
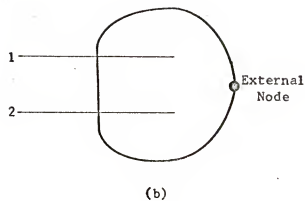
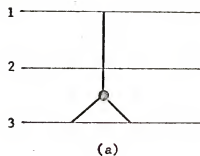


Figure 26. Illustration of a node which branches down.

There are six three-branch nodes between sections 3 and 4. These nodes "branch up" because they are oriented in such a way that two branches on section 3 combine to form one branch on section 4.

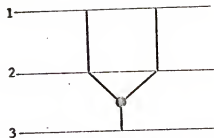
A three-branch node which branches up is shown in Figure 27a. When the first two sections are considered, the associated node-branch network, shown in Figure 27b, has a value of  $G_1^{\max}$  of two as two circuits are formed with the external node. When all three sections are considered, the associated node-branch network, shown in Figure 27c, also has a value of  $G_2^{\max}$  of two as two circuits are formed with the external node. Thus, the effect of adding one three-branch node which branches up to the node-branch network is to leave  $G_1^{\max}$  unchanged. Thus, the six three-branch nodes which branch up between sections 3 and 4 in Figure 24 have no effect on  $G_1^{\max}$ . Therefore, the value of  $\Delta G_3^{\max}$  is zero, as indicated in Table 3. The change in  $G_1^{\min}$ ,  $\Delta G_3^{\min}$ , is also zero as no internal circuits have been formed in the network.

When two channels with different labels join, the convention employed during the course of this work (Section 4.5.1) is that the lowest of the two numbers is used to label the resulting channel. This was done in Figure 24. The joining events in Figure 24 are recorded in the subnetwork graph shown in Figure 28. The events which take place between sections 3 and 4 produce this graph. The fact that these events were not previously recorded during the analysis results in the value of zero for  $\Delta G_3^{\min}$ . This is according to the procedure presented in Section 4.5.3.

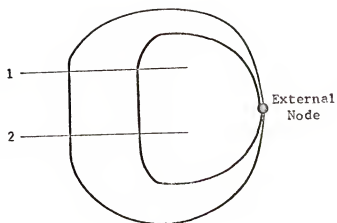
Sections 4 and 5 are identical; hence, both  $\Delta G_4^{\max}$  and  $\Delta G_4^{\min}$  are zero.



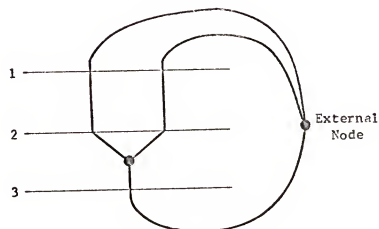
Section  
Numbers



(a)



(b)



(c)

Figure 27. Illustration of a node which branches up.



Figure 28. Subnetwork graph associated with the analysis of the network shown in Figure 24.

There are six three-branch nodes between sections 5 and 6, all of which branch down. As a result,  $\Delta G_5^{\max}$  is +6 for section 6. No internal circuits are formed by the addition of this section, so  $\Delta G_5^{\min}$  is zero.

When section 7 is analyzed, seven three-branch nodes, all of which branch up, are observed. As a result,  $\Delta G_6^{\max}$  is zero; however, seven internal circuits are formed in the network. One of the nodes is formed when two branches, both labeled 1, join. The remaining joining events are all recorded in the linear graph of Figure 28. Therefore, each of these events increases  $G_1^{\min}$  by one; thus,  $\Delta G_6^{\min}$  is +7.

If the analysis of each successive section is continued in this way, the values of  $\Delta G_i^{\max}$  and  $\Delta G_i^{\min}$ , presented in Table 3, are found. When the resulting values of  $\sum \Delta G_i^{\max}$  and  $\sum \Delta G_i^{\min}$  are plotted against volume of material analyzed, the curves shown in Figure 25b are obtained. This assumes that the serial sections are uniformly spaced so that the volume of material removed per section is the same for all sections. Note that the slopes of the curves presented in Figures 25a and 25b are the same in spite of the fact that  $G_i^{\max}$  and  $\sum \Delta G_i^{\max}$  are not the same. Since the slopes are the same, the values of  $G_v^{\max}$  and  $G_v^{\min}$  obtained by Method III are the same as the values obtained by Method II. The values of  $G_i^{\min}$  are the same as the values of  $\sum \Delta G_i^{\min}$  because Method II and Method III for the determination of  $G_v^{\min}$  are the same. The values of  $G_i^{\max}$  in Table 3 are equal to the corresponding values of  $\sum \Delta G_i^{\max}$  +7. Seven is the number of branches through the top of the sample in

Figure 24. Since the number of branches through the top of the sample remains constant throughout the analysis, these branches do not contribute to  $\sum \Delta G_i^{\max}$ . They, however, do contribute to the value of  $G_i^{\max}$ , thus the difference in these two parameters. This constant factor does not affect the equality of the slopes of the plots of  $G_i^{\max}$  and  $\sum \Delta G_i^{\max}$  versus volume of material analyzed, as indicated in the preceding example.

Method III contains further modifications of Method II as follows.

Recall from Section 4.5.2 that nodes of order greater than three can always be treated as collections of three-branch nodes. For example, consider again Figure 18c which shows the three-branch node equivalent of the five-branch node of Figure 18a. Two of the three three-branch nodes branch up and one branches down. Thus, this five-branch node increases  $G_i^{\max}$  by one.

This illustrates the fact that the effect of a node of any order on  $G_i^{\max}$  is equal to plus (+) the number of branches from the node which passes through the bottom of the sample minus (-) one. For example, the five-branch node of Figure 18a has two branches which pass through the bottom of the sample. Thus,  $\Delta G_i^{\max}$  is  $2 - 1 = 1$ . This also applies to three-branch nodes. For the three-branch node of Figure 27a which branches up,  $\Delta G_i^{\max} = 1 - 1 = 0$ . For the three-branch node of Figure 26a which branches down,  $\Delta G_i^{\max} = 2 - 1 = 1$ .

The appearance of new branches which split on a later section, as shown schematically in Figure 19, is taken into account as

follows. When the new channel splits, as on section 3 of Figure 19b,  $G_1^{\max}$  is increased by one. If one of the resulting channels ends on a later section, as in Figure 19, then  $G_1^{\max}$  is decreased by one.

The number of separate parts per unit volume,  $N_v$ , is determined by the method presented in Section 4.7.

To summarize, Method III allows the determination of the maximum and minimum values of cumulative genus by the summation of the effect on the cumulative genus produced by changes which occur in the void space as each serial section is considered. As a result, it is unnecessary to construct the associated node-branch network as in the method of Kronsbein, et al., or to employ any equations as in Method II presented in Section 4.5.

#### 4.9 Analysis of a Space, Material or Void, Which Exhibits Multiple Connectivity on a Single Microsection

The method of analysis presented in this section can be employed to determine the topological properties of any sinter structure. A space, material or void, which is multiply connected on a single microsection can be analyzed with this method.

A general procedure for the analysis of two-phase structures would allow the simultaneous determination of the genus of the interface between the two phases and the number of separate parts of both phases when either of the phases is analyzed. The procedure presented here allows the determination of the genus of the interface between the two phases and the number of separate parts of either, but not both phases, when either of the phases is analyzed. Therefore, this procedure can be applied to either space of any

sinter structure, as only separate parts of the void space are experimentally observed. The general applicability of the procedure presented here is considered further at the end of this section.

As with the preceding methods of analysis, a maximum and minimum limit of the genus is obtained. Throughout the analysis for the values of  $G_i^{\max}$ , the space being analyzed is assumed to be capped at the top and bottom of the sample. Only branches which pass through the sides of the sample are assumed to be incident upon the external node. That this has no effect on the values of  $G_i^{\max}$  which are obtained is shown in the following. It should be kept in mind that the parameter of interest is the change in the values of  $G_i^{\max}$  and  $G_i^{\min}$  and not the actual values of  $G_i^{\max}$  and  $G_i^{\min}$ .

The number of branches through the top of the sample remains constant throughout the analysis and therefore has no effect on the change in  $G_i^{\max}$  as successive serial sections are considered. The number of branches through the bottom of the sample varies from section to section. However, this number can be characterized by some average value since there is no systematic variation in this number as successive sections are considered. As a result, the branches through the bottom of the sample have no effect on the average on the change in  $G_i^{\max}$ , the parameter of interest, as successive sections are considered and hence are assumed to be capped at the sample surface.

During the course of this research, the channels through the top and bottom of the samples were assumed to be capped only when the space being analyzed exhibited multiple connectivity on a given microsection. However, this assumption could have been made

for all samples without changing the value obtained for  $G_v^{\max}$ . For example, if this assumption had been made in the case of the hypothetical network of Figure 24, the values of  $\sum \Delta G_1^{\max}$  and  $\sum \Delta G_1^{\min}$  would have been the same as those obtained in Section 4.6. Thus, the value obtained for  $G_v^{\max}$  is the same whether or not it is assumed that channels through the top and bottom of the  $i^{\text{th}}$  sample are capped.

The number of branches through the sides of the sample generally increases as the area of the sides increases. Thus, this contribution cannot be neglected in the determination of the values of  $G_1^{\max}$ , as can the contribution of branches through the top and bottom of the sample.

All branches through the surface of the sample are assumed capped during the determination of the values of  $G_1^{\min}$ .

After the desired area on each serial section is delineated (see Section 4.3), a network is constructed in the area as follows. The intersection of the space (material or void) chosen for analysis with the plane of each serial section is a set of areas bounded by closed curves which are the intersection of the plane of the serial section with the void-solid interface. If each of these areas is shrunk continuously, a set of networks of nodes and branches is formed. This construction is a two-dimensional analogue of the deformation retract in three dimensions. An example of such a network is shown for a hypothetical section through a sinter structure in Figure 29. The network in two dimensions obtained by this procedure will, in general, be composed of a number, or set, of isolated networks, or separate parts, called subnetworks. The

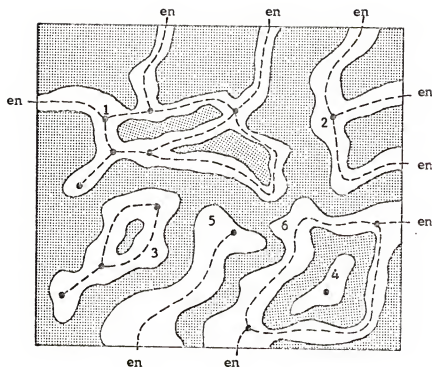


Figure 29. Hypothetical serial section illustrating the construction of a network analogous to the deformation retract in three dimensions.



retract shown in Figure 29 consists of six subnetworks. These isolated subnetworks may be connected in the third dimension.

The next and most important step in the analysis is the comparison in succession of the networks on adjacent serial sections. As the comparison of each successive network with the preceding network is made, changes are noted and tabulated. Four classes of change can occur. The tabulation of these changes is facilitated by means of a labeling procedure which will be described as each class of change is presented. The four classes of change which must be monitored and tabulated are listed in Table 4. Each of these will now be described in detail.

Unless the material or void space is specified, the following procedure applies to either space.

Class I: Changes in the Number of Subnetworks. Each subnetwork on the first serial section is labeled with a different number, as illustrated in Figure 29. As each successive section is considered, corresponding subnetworks are labeled with the same number as on the preceding section.

In general, subnetworks will appear during the analysis, as illustrated in Figures 14 and 19. These subnetworks are referred to as new subnetworks if they do not contact the sides of the sample. For example, the network indicated by an arrow in Figure 16 is not a new subnetwork. A subnetwork such as this which contacts the external node is labeled with a new number just as those subnetworks which contact the external node through the top of the sample.

Table 4. Classification of changes which occur during the analysis of serial sections.

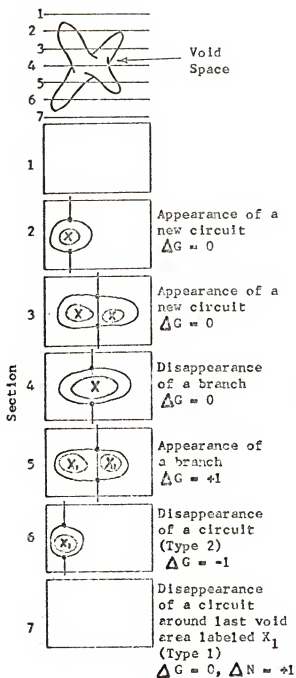
Class	Description of Change	$G_i^{\max}$	$G_i^{\min}$	N	Comment
I Appearance and disappearance of subnetworks	Appearance of subnetwork	0	0	0	If the subnetwork is labeled X or is the last subnetwork labeled $X_i$ , $i=1,2,3,\dots$ All other subnetworks
	Disappearance of subnetwork	0	0	+1	
		0	0	0	
II Appearance and disappearance of circuits and branches	Appearance of new circuit	0	0	0	If the circuit bounded a subnetwork labeled X or the last subnetwork labeled $X_i$ , $i=1,2,3,\dots$ All other circuits
	Appearance of new branch	+1	+1	0	
	Disappearance of a circuit	0	Type 1 0	+1	
		-1	Type 2 -1	0	All other circuits
	Disappearance of a branch	0	0	0	
III Separation and connection of subnetworks	Separation of a subnetwork into two subnetworks	0	0	0	
	Appearance of a connection between two subnetworks	0	0	0	If labels are different
		+1	+1	0	If labels are the same
IV Appearance and disappearance of branches and circuits incident on the external node	Appearance of a branch to the external node	+1	0	0	
	Disappearance of a branch to the external node	0	0	0	
	Collapse (or disappearance) of a circuit incident on the external node	-1	0	0	
	Appearance of a circuit incident on the external node	0	0	0	

When a new subnetwork appears, it is labeled with a symbol rather than a number; the same symbol is used for all new subnetworks. An X is used here for illustration [however, three dots ( $\therefore$ ) were used during the course of this work]. This allows the new subnetworks to be followed from section to section, just as in the case of subnetworks already present.

Since separate parts of the material space are not observed, it is unnecessary to label new subnetworks during the analysis of the material space. However, it is desirable to label new subnetworks during the analysis of the material space so that all subnetworks on a given section will be labeled. This avoids confusion as to which subnetworks have and have not been analyzed.

If a new subnetwork separates into two or more subnetworks, the resulting subnetworks are all labeled  $X_i$ , where  $i$  is an integer, 1 being used for the first such event, 2 for the next, etc. In general, as successive serial sections are considered, some subnetworks labeled with a given  $X_i$  end or disappear. When the last subnetwork labeled with a given  $X_i$ ,  $X_1$  for example, disappears, the presence of a separate part is indicated. This is illustrated in Figure 30a. This event and the disappearance of subnetworks labeled X indicate the presence of a separate part of the void space because the subnetwork which ends is not connected to the sample surface by any path through the void space.

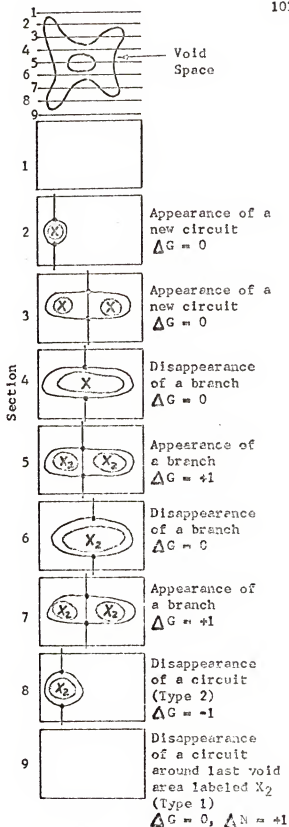
If two or more subnetworks with the same  $X_i$  label join and then all subnetworks with this label end later in the analysis, the presence of a multiply connected separate part is indicated.



$$\text{Total: } \Delta G = +1 - 1 = 0$$

$$\Delta N = +1$$

(a)



$$\text{Total: } \Delta G = +1 + 1 - 1 = +1$$

$$\Delta N = +1$$

(b)

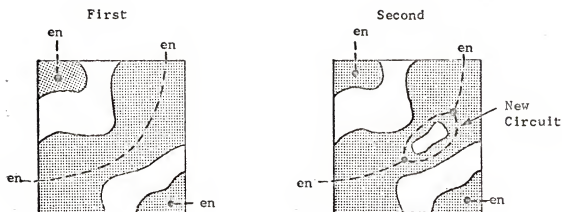
Figure 30. Appearance and disappearance of circuits associated with separate parts during the analysis of the solid space.

This is illustrated in Figure 30b. When two subnetworks with the same  $X_i$  label join,  $G_i^{\max}$  and  $G_i^{\min}$  are both increased by one, as indicated in Table 4 under Class III changes. This will be considered again in the following discussion of Class III changes.

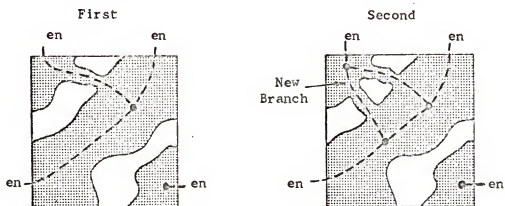
A separate part is observed when either of two events occur: (1) a subnetwork labeled  $X$  ends, and (2) a subnetwork labeled  $X_i$ , which is the last remaining subnetwork with this label, ends. The total number of these two events which is observed during the analysis of a serial section is equal to the change in the number of separate parts for that serial section,  $\Delta N$ .

This procedure does not allow the detection of separate parts which intersect the sample surface. If these separate parts are neglected, a small error is introduced into the results, as shown in Appendix 1.

**Class II: Changes in the Connectivity of the Subnetworks.**  
Changes in the connectivity of each subnetwork must be noted as successive serial sections are considered. The connectivity of a subnetwork is increased in either of two ways - by the appearance of a new circuit or by the appearance of a new branch. These events are illustrated in Figure 31. A new circuit appears between the two serial sections shown in Figure 31a. Changes of this type have no effect on the value of  $G_i^{\max}$  or  $G_i^{\min}$ . This is because such a new circuit can be shrunk through the space being analyzed in the third dimension (perpendicular to the plane of the serial sections) until it collapses or forms a point without crossing the void-solid



(a)



(b)

Figure 31. Illustration of (a) appearance of a new circuit and (b) appearance of a new branch in the sub-networks constructed on successive serial sections.

interface. Such a circuit is not an independent circuit, and therefore does not contribute to the genus of the structure (see Section 2,3).

The appearance of a new branch is illustrated in the serial sections shown in Figure 31b. Changes of this type increase both  $G_1^{\max}$  and  $G_1^{\min}$  by one. This is because any circuit of which such a new branch is a part cannot be shrunk to a point without crossing the void-solid interface. Therefore, a new branch is part of an independent circuit, and hence contributes to the genus of the structure.

The connectivity of a subnetwork is decreased in either of two ways - by the disappearance of a branch or by the collapse or disappearance of circuits. These events are the same as those illustrated in Figure 31 with the order of the serial sections reversed.

The disappearance of a branch leaves both  $G_1^{\max}$  and  $G_1^{\min}$  unchanged, as the branch which has disappeared still remains in the third dimension. Therefore, the connectivity of the deformation retract is unchanged by this event.

The effect of the collapse of a circuit depends upon the manner in which the circuit was formed. There are two types of circuit collapse, as indicated in Table 4.

Type 1 is the disappearance of a circuit which was the last circuit associated with the appearance of a new circuit. Type 1 events occur only during the analysis of the material space, as this event is associated with the presence of a separate part of the void space. A Type 1 event leaves both  $G_1^{\max}$  and  $G_1^{\min}$  unchanged and increases  $N$  by one, as illustrated by the following examples. The labeling procedure is the same as that used for new subnetworks under Class I changes.

Figure 30a shows a simply connected separate part which is intersected by five serial sections which are also shown. The analysis is performed on the material space, and the changes in the topological properties are indicated next to each serial section.

The areas encircled by new circuits are labeled  $X$ . Two of these areas join to form one area between sections 3 and 4, and the resulting area is labeled  $X$ . This area then splits into two areas between sections 4 and 5, both of which are labeled  $X_1$  to indicate they are joined on a previously analyzed serial section. One of these areas then ends between sections 5 and 6, and the circuit around this void area collapses. This is a Type 2 event which produces a decrease of 1 in both  $G_1^{\max}$  and  $G_1^{\min}$  as a branch is removed by this event. The other void area labeled  $X_1$  then ends between sections 6 and 7, and the circuit around this void area collapses. This is a Type 1 event, and therefore produces no change in  $G_1^{\max}$  or  $G_1^{\min}$ . This event indicates the presence of a separate part of the void space. A simply connected separate part does not contribute to the genus; therefore, the total change in genus,  $\Delta G$ , produced by the separate part of Figure 30a, is zero, as indicated by summing the changes in genus associated with this separate part.

Multiply connected isolated separate parts of the void space can also be analyzed by this procedure, as illustrated in Figure 30b. The labeling procedure is the same as that used for separate parts under Class I changes. These subnetworks are labeled  $X_2$  rather than  $X_1$  to indicate that the subnetworks so labeled are not connected to those labeled  $X_1$ . When the last void area labeled  $X_2$  ends between sections 8 and 9, the accompanying circuit collapse is a Type 1 event. As a result,  $G_1^{\max}$  and  $G_1^{\min}$  are unchanged and  $N$  is increased by one. The total change in  $G_1^{\max}$  and  $G_1^{\min}$  associated with the separate part of Figure 30b is +1, as this separate part is multiply connected and has a genus of one.



### Class III: Separations or New Connections Between Subnetworks.

The separation of subnetworks into two or more subnetworks and the formation of connections between subnetworks must be noted as successive serial sections are considered. This is facilitated by means of the labeling procedure as follows. Subnetworks that result from the separation of a given subnetwork are given the same label as the original subnetwork. For example, consider the serial sections shown in Figure 32. The subnetwork labeled 3 on the first section separates by the removal of a branch to form two subnetworks on the second section; both are labeled 3 according to the above convention. When two or more subnetworks with different labels join, the smallest of the labels is used to relabel all subnetworks, with the larger of the two labels on both sections under consideration. Also, when a subnetwork labeled with a number joins a new subnetwork, the number is used to label the resulting subnetwork. This labeling procedure does away with the necessity of constructing a subnetwork graph, as was the case for Methods II and III (see Sections 4.5.3 and 4.8).

Separations of subnetworks produce no change in  $G_1^{\max}$  and  $G_1^{\min}$ , as this corresponds to the disappearance of a branch (Class II change), as illustrated in Figure 32. The appearance of a connection between two subnetworks with the same number produces an increase of one in both  $G_1^{\max}$  and  $G_1^{\min}$ . This is because such a joining event completes a circuit in the space being analyzed since the fact that the subnetworks which join have the same label indicates they are joined by a path through the portion of the

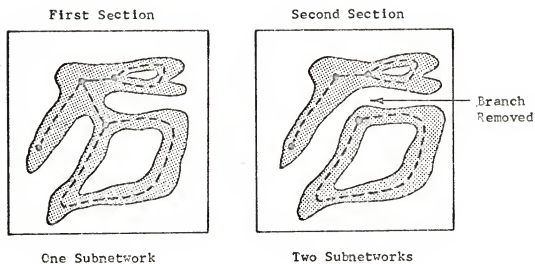


Figure 32. Illustration of the separation of a subnetwork between two successive serial sections.

structure previously analyzed. Joining events between numbered and new subnetworks leave  $G_i^{\max}$  and  $G_i^{\min}$  unchanged as this joining event does not complete a circuit in the space being analyzed. The number is used to label the resulting subnetwork.

If two or more subnetworks with different  $X_i$  labels join, the label with the smaller value of  $i$  is used to relabel all subnetworks with the larger value of  $i$  on both sections under consideration. If a subnetwork with a given  $X_i$  label joins a numbered subnetwork, the number is used to label the resulting subnetwork, and all other subnetworks labeled with that  $X_i$  label on both sections under consideration. No change in  $G_i^{\max}$ ,  $G_i^{\min}$  or  $N$  is associated with these events as they produce no circuits or separate parts.

Class IV: Connections to the External Node. Changes in the number of branches which contact the external node must be monitored also. As pointed out previously, only branches which pass through the sides of the volume of material analyzed are assumed to contact the external node. The following Class IV changes are possible.

Branches to the external node can appear or disappear, as illustrated in Figure 33a. The appearance of a branch increases  $G_i^{\max}$  by one as this event completes a circuit with the external node. The value of  $G_i^{\min}$  remains unchanged. The appearance of a circuit incident on the external node leaves  $G_i^{\max}$  and  $G_i^{\min}$  unchanged. This is because a circuit produced in this way is not an independent circuit since it can be shrunk in the third dimension (perpendicular to the serial sections) until it collapses without crossing the void-solid interface.

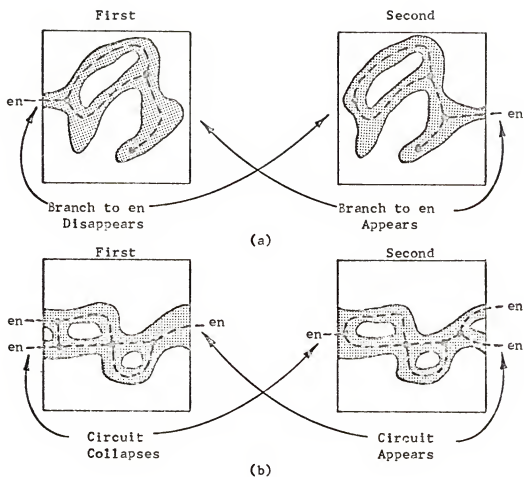


Figure 33. Illustration of sample surface effects. The appearance and disappearance of (a) branches to the external node and (b) circuits incident on the external node.

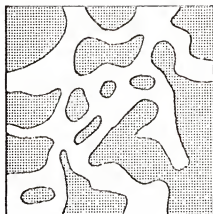
When the four classes of change described above are tabulated during the analysis of a set of serial sections, values of  $\Delta G_1^{\max}$ ,  $\Delta G_1^{\min}$  and  $\Delta N$  are obtained as each successive section is considered. The total change in each of these parameters, after a given number of sections has been analyzed, is referred to as the "cumulative change" of that parameter. Only those events which produce changes in  $G_1^{\max}$ ,  $G_1^{\min}$  and  $N$  are tabulated. Accordingly, events which must be noted are (see Table 4): disappearance of (a) subnetworks, (b) circuits, (c) branches to the external node, (d) circuits incident upon the external node; and appearance of (e) new branches and (f) connections between subnetworks. The desired values of  $G_v^{\max}$ ,  $G_v^{\min}$  and  $N_v$  are obtained by plotting the cumulative change of  $G_1^{\max}$ ,  $G_1^{\min}$  and  $N$  versus volume of material analyzed and taking the slope of the linear portion of the respective curve (see Sections 4.6 and 4.7).

An example illustrating the features of this method of analysis will now be presented by analyzing the schematic serial sections shown in Figure 34. The shaded region has no multiple connectivity on a given section and normally would be simplest to analyze. The multiply connected, unshaded region will be considered here for the sake of illustration.

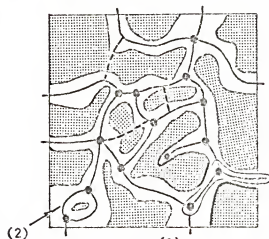
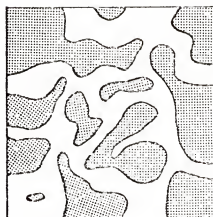
Consider the first serial section. A node-branch network is constructed on this section, as shown in Figure 33b. This network is constructed so that the phase of interest is covered by the network, and no circuit in the network can be shrunk continuously to a point. The term covered means that the two-dimensional intersection of the phase of interest with the section under consideration

Section  
Number

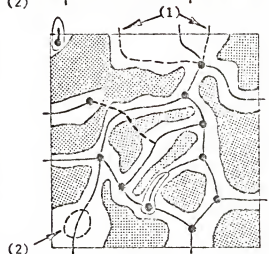
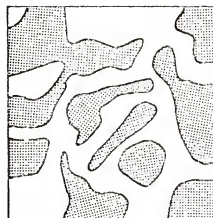
1



2



3



(a)  
Before Analysis

(b)  
After Analysis

Figure 34. Hypothetical serial sections illustrating the analysis of a space which exhibits multiple connectivity on the serial sections.

can be shrunk continuously until it comes into one-to-one correspondence with the superimposed node-branch network. All branches which cross the sides of the sample are assumed to be incident on the external node.

The second serial section is considered and a node-branch network is constructed on this section also. In the process, any differences between the networks on the first two sections are noted. As each change is observed, its effect on  $G_i^{\max}$ ,  $G_i^{\min}$  and  $N$  is noted in order to obtain the values of  $\Delta G_i^{\max}$ ,  $\Delta G_i^{\min}$  and  $\Delta N$ . The dotted lines on section 2 represent branches which were present on section 1, but not on section 2. The removal of these branches does not change  $G_i^{\max}$  or  $G_i^{\min}$ , as these events represent disappearance of branches (see Table 4). The portion of the node-branch network enclosed by the light line on section 2 was not present in section 1. The appearance of this portion of the network adds one internal branch to the network and one branch to the external node. The appearance of the internal branch increases both  $G_i^{\max}$  and  $G_i^{\min}$  by one (see Table 4). The appearance of a branch to the external node increases  $G_i^{\max}$  by one and leaves  $G_i^{\min}$  unchanged (see Table 4). When the analysis of section 2 is complete, the values of  $\Delta G_i^{\max}$  and  $\Delta G_i^{\min}$  are +2 and +1, respectively.

When section 3 is considered, the circuit incident on the external node, which was formed by the two branches labeled (1), has collapsed. As a result,  $G_i^{\max}$  is decreased by one and  $G_i^{\min}$  remains unchanged (see Table 4). The circuit, labeled (2) on section 2 and indicated by the dotted line on section 3, has collapsed when section 3 is considered. As a result, both  $G_i^{\max}$

and  $G_1^{\min}$  are decreased by one (see Table 4). The appearance of the branch to the external node in the upper left corner of the third section has no effect on  $G_1^{\max}$  or  $G_1^{\min}$  as no circuit is formed by this event. The appearance of the branch circled by the light line on section 3 increases both  $G_1^{\max}$  and  $G_1^{\min}$  by one. The analysis of section 3 thus results in a value of  $\Delta G_1^{\max}$  of -1 and a value of  $\Delta G_1^{\min}$  of 0.

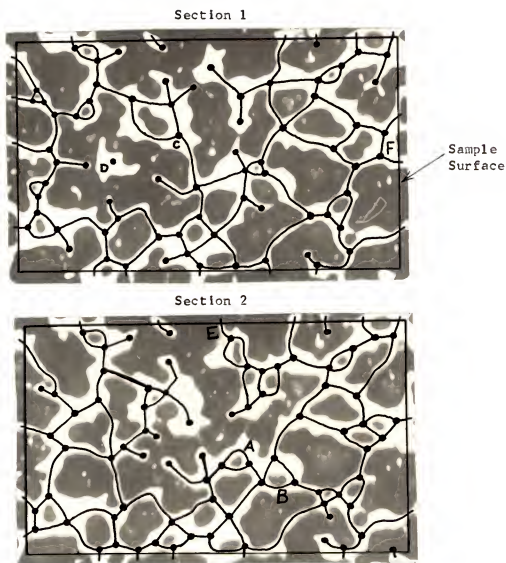
Two serial sections through an actual sinter structure are shown in Figure 35. The node-branch networks have been constructed on the sections, and a number of the changes listed in Table 4 are pointed out. For the sake of illustration, a rectangular, rather than a square, area is shown.

During the analysis of an actual sinter structure, all changes, such as those illustrated in the above examples and presented in Table 4, must be tabulated as each section is analyzed. The procedure presented in Section 4.6 is then employed to determine the desired values of  $G_v^{\max}$  and  $G_v^{\min}$ . The number of separate parts per unit volume is determined by the method presented in Section 4.7.

The final method of analysis, presented in this section, can be employed to determine the topological properties, genus per unit volume and number of separate parts per unit volume of any structure for which suitable serial sections are available. The acceptability of the serial sections is based on considerations such as spacing of the sections and distinguishability of the phases of interest on the sections. This is considered further in Chapter VI.

Structures consisting of more than two phases can be analyzed with this method of analysis. In this case, each phase must be analyzed separately.





- A - Appearance of a new circuit
- B - Appearance of a new branch
- C - Disappearance of a branch
- D - Appearance of a connection between two subnetworks
- E - Appearance of a branch to the external node
- F - Collapse of a circuit incident on the external node

Figure 35. Two serial sections through a sample of 48 micron electrolytic copper powder sintered to a density of 6.05 gm/cc illustrating several of the types of changes which occur as successive serial sections are analyzed.

As pointed out at the beginning of this section, the method of analysis presented here cannot be employed to analyze a general, two-phase structure; that is, a structure, both phases of which have isolated separate parts. However, if this method of analysis is extended as follows, a general two-phase structure can be analyzed. It is only necessary to employ circuit collapse and disappearance of subnetworks simultaneously as indicators of the presence of separate parts. In this case, the collapse of circuits (Type 1) indicates the presence of separate parts of the space complementary to the one being analyzed, and the disappearance of subnetworks, if they are labeled  $X$  or if they are the last labeled with a given  $X_i$ , indicates the presence of separate parts of the space being analyzed.

## CHAPTER V

### EXPERIMENTAL RESULTS

#### 5.1 Introduction

The methods of analysis presented in Chapter IV were used to determine the topological properties of 21 copper sintered structures. The results of this investigation are presented in this chapter.

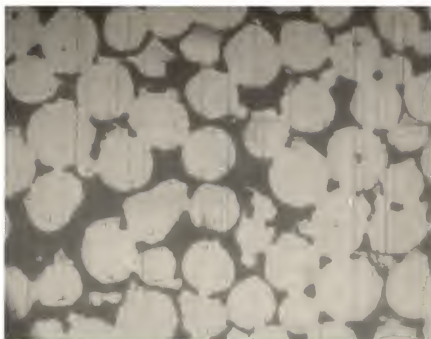
A portion of a serial section used during the analysis of each structure is presented in Figures 36 to 53. Data on the grain boundary structure were taken for the 48 micron\* spherical and electrolytic powders; therefore, an etched, as well as an unetched, surface is shown for each of the samples prepared from these powders.

The serial sections for the 115 micron spherical powder samples shown in Figures 36, 37 and 38 were obtained by means of the Jung microtome (see Section 3.5). Serial sections for the sample of the 115 micron spherical powder shown in Figure 39 were obtained by standard metallographic polishing (see Section 3.5).

The samples which were sectioned with the microtome were first immersed in molten solder. No solder can be seen in the void space of the lowest density samples shown in Figure 36; however,

---

\*The -270 +325 mesh and -120 +140 mesh size fractions are referred to as 48 micron and 115 micron powders, respectively. These are the average dimensions of the holes in the screens used to obtain these size fractions (see Section 3.1).



(a)

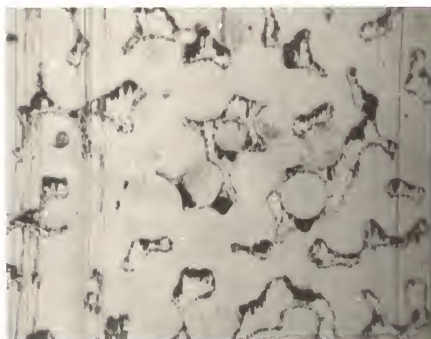


(b)

Figure 36. Serial sections through 115 micron spherical copper powder sintered to densities of (a) 5.94 and (b) 6.15 gm/cc (125 X).



(a)



(b)

Figure 37. Serial sections through 115 micron spherical copper powder sintered to densities of (a) 6.67 and (b) 7.05 gm/cc (125 X).



(a)



(b)

Figure 38. Serial sections through 115 micron spherical copper powder sintered to densities of (a) 7.50 and (b) 7.76 gm/cc (125 X).

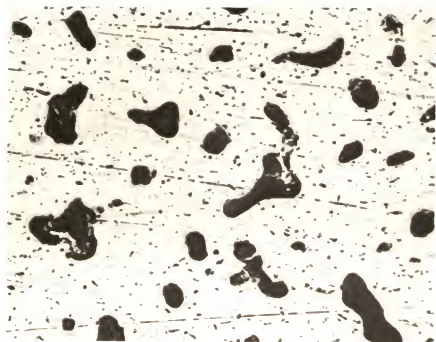
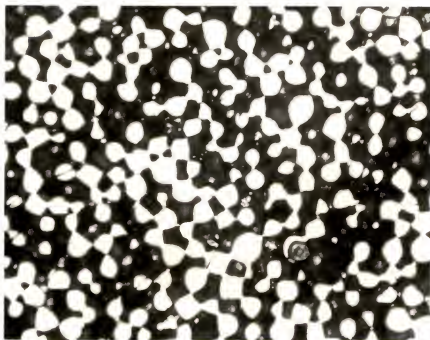
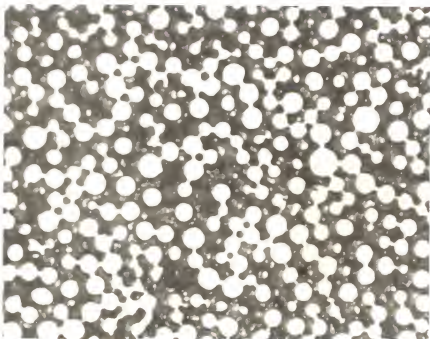


Figure 39, Serial section through 115 micron spherical copper powder sintered to a density of 8.05 gm/cc (125 X).



(a)



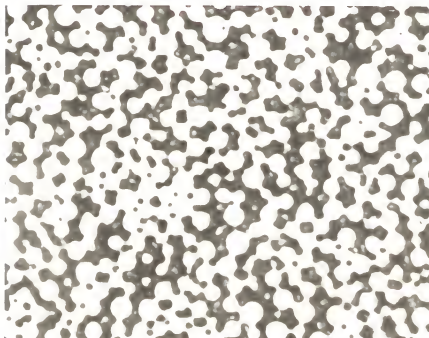
(b)

Figure 40. Serial sections through 48 micron spherical copper powder sintered to a density of 5.91 gm/cc (a) etched (200 X) and (b) unetched (130 X).





(a)



(b)

Figure 41. Serial sections through 48 micron spherical copper powder sintered to a density of 6.62 gm/cc (a) etched (200 X) and (b) unetched (130 X).

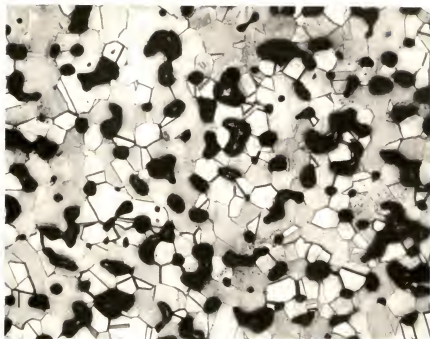


(a)



(b)

Figure 42. Serial sections through 48 micron spherical copper powder sintered to a density of 7.26 gm/cc (a) etched (200 X) and (b) unetched (130 X).

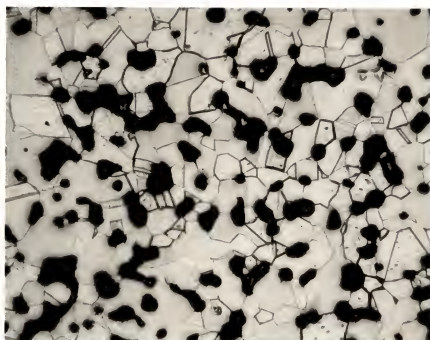


(a)

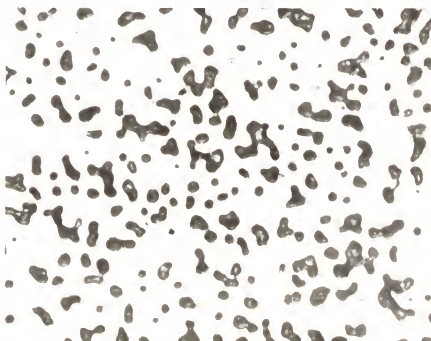


(b)

Figure 43. Serial sections through 48 micron spherical copper powder sintered to a density of 7.74 gm/cc (a) etched (200 X) and (b) unetched (130 X).

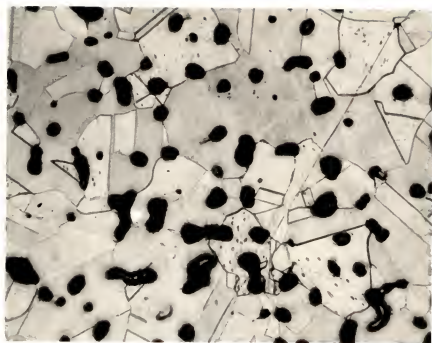


(a)



(b)

Figure 44. Serial sections through 48 micron spherical copper powder sintered to a density of 8.00 gm/cc (a) etched (200 X) and (b) unetched (130 X).

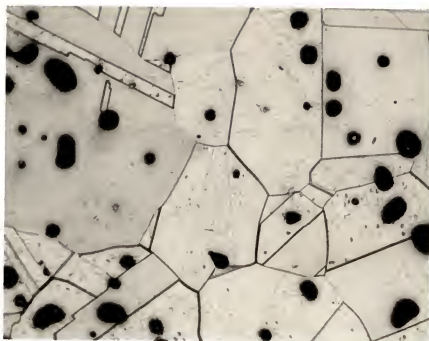


(a)



(b)

Figure 45. Serial sections through 48 micron spherical copper powder sintered to a density of 8.25 gm/cc (a) etched (200 X) and (b) unetched (130 X).

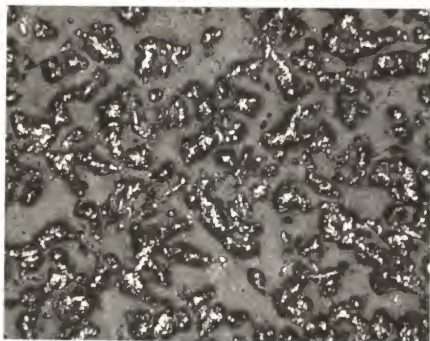


(a)

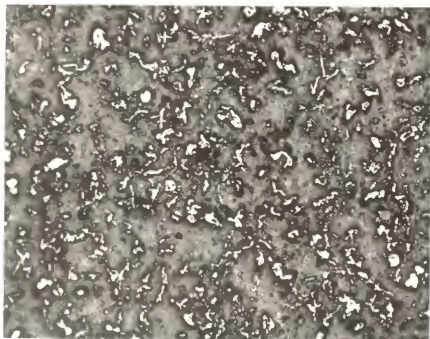


(b)

Figure 46. Serial sections through 48 micron spherical copper powder sintered to a density of 8.40 gm/cc (a) etched (200 X) and (b) unetched (130 X).



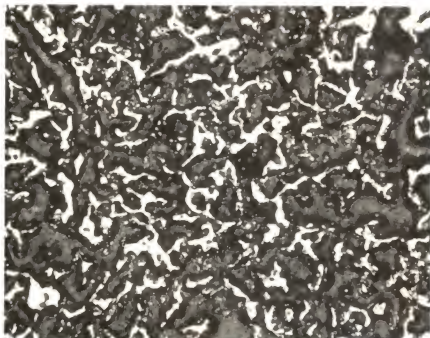
(a)



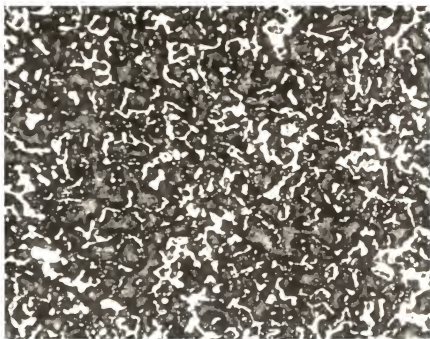
(b)

Figure 47. Serial sections through 48 micron electrolytic copper powder sintered to a density of 1.30 gm/cc and infiltrated with epoxy (a) etched (200 X) and (b) unetched (100 X).





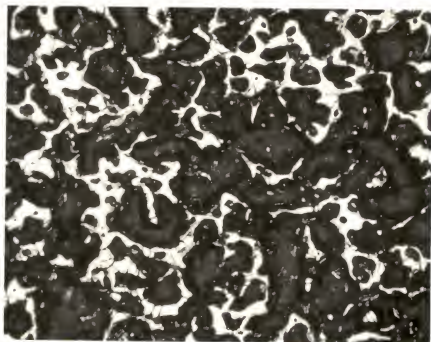
(a)



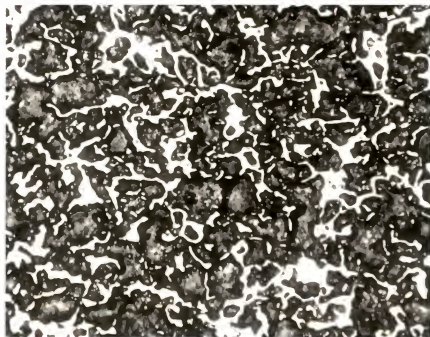
(b)

Figure 48. Serial sections through 48 micron electrolytic copper powder sintered to a density of 2.81 gm/cc and infiltrated with epoxy (a) etched (200 X) and (b) unetched (100 X).





(a)



(b)

Figure 49. Serial sections through 48 micron electrolytic copper powder sintered to a density of 3.99  $\text{g}/\text{cc}$  and infiltrated with epoxy (a) etched (200 X) and (b) unetched (100 X).

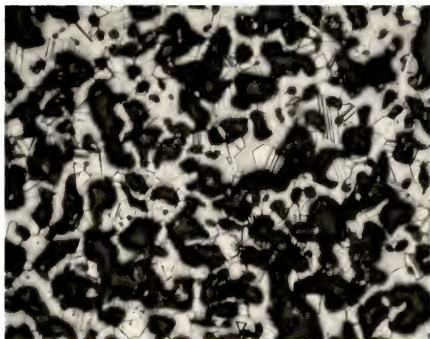


(a)

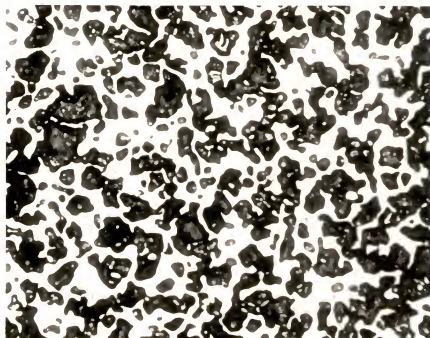


(b)

Figure 50. Serial sections through 48 micron electrolytic copper powder sintered to a density of 4.96 gm/cc and infiltrated with epoxy (a) etched (200 X) and (b) unetched (100 X).

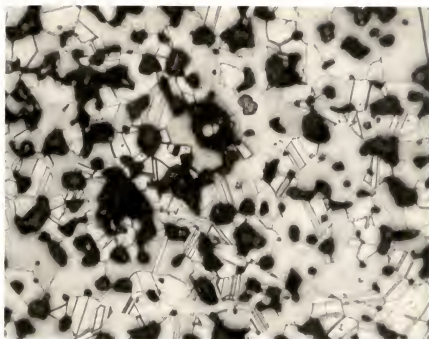


(a)



(b)

Figure 51. Serial sections through 48 micron electrolytic copper powder sintered to a density of 6.05 gm/cc and infiltrated with epoxy (a) etched (200 X) and (b) unetched (100 X).

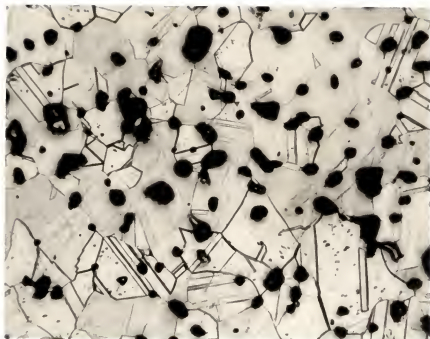


(a)



(b)

Figure 52. Serial sections through 48 micron electrolytic copper powder sintered to a density of 6.95 gm/cc and infiltrated with epoxy (a) etched (200 X) and (b) unetched (100 X).



(a)



(b)

Figure 53. Serial sections through 48 micron electrolytic copper powder sintered to a density of 7.92 gm/cc and infiltrated with epoxy (a) etched (200 X) and (b) unetched (100 X).

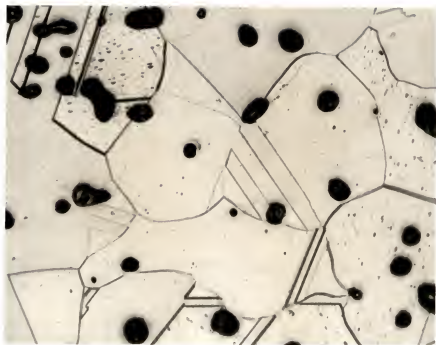


Figure 54. Photomicrograph of 48 micron electrolytic powder sintered to a density of 8.45 gm/cc, etched (200 X).

this structure remained brittle after immersion in the solder so that it was possible to obtain sections which allowed particle contacts to be counted. Some solder is present in the void space of the structures shown in Figures 37 and 38; however, these samples also became brittle after immersion in the liquid solder.

All serial sections for the 48 micron spherical and electrolytic powder samples were prepared by metallographic polishing. The void space of the 48 micron electrolytic powder samples shown in Figures 47 to 53 was filled with epoxy before the samples were sectioned (see Section 3.5).

## 5.2 Topological Properties of the 115 Micron Spherical Powder

### 5.2.1 Genus per Gram Data

The results for those samples of the 115 micron powder for which contacts per particle were counted (see Section 4.2 for method of analysis) are presented in Table 5. The average value of contacts per particle,  $\overline{C/P}$ , is presented along with the standard deviation of  $\overline{C/P}$ . The number of particles counted for each sample is also given, as well as the number of particles which must be counted in order to have 90 per cent confidence that the difference between the experimentally determined value of  $\overline{C/P}$  and the true value is less than 5 per cent. This is according to the Central Limit Theorem of statistical analysis [24].

In the process of determining  $\overline{C/P}$ , the number of particles having a given number of contacts is determined. As a result, the fraction of all particles having a given number of contacts can be calculated. These data and the corresponding frequencies are

Table 5. Data for those samples for which contacts per particle were counted.

Sample Density (gm/cm <sup>3</sup> )	Volume Fraction Porosity	Average Number of Particle C/P	Standard Deviation	Number of Particles Counted	Critical Number of Particles (90% Confidence at 5% Error)	Limits of Value of Genus per Gram - G <sub>p</sub>	
						Lower	Upper
<u>115 Micron Spherical Powder</u>							
5.94	0.337	6.79	1.513	75	75	2.99x10 <sup>5</sup>	3.60x10 <sup>5</sup>
6.15	0.314	6.87	1.429	201	67	3.20x10 <sup>5</sup>	3.68x10 <sup>5</sup>
<u>48 Micron Spherical Powder</u>							
5.91	0.340	6.60	1.195	50	47	4.12x10 <sup>6</sup>	4.76x10 <sup>6</sup>
6.62	0.261	7.08	1.355	60	60	4.57x10 <sup>6</sup>	5.24x10 <sup>6</sup>



presented in Table 6 for the 115 micron spherical powder sintered to a density of 6.15 gm/cc ( $V_V = 0.314$ ). From these data, the frequency distribution of contacts per particle can be plotted as shown in Figure 55.

The genus per unit volume of the samples, for which values of  $\overline{C/P}$  are given in Table 5, was calculated using equation (6). Since each contact lies between two particles, the value of  $C_V/P_V$  is one-half the average number of contacts per particle,  $\overline{C/P}$ . In order to calculate the number of particles per unit volume,  $P_V$ , for each of the two spherical size fractions, it is necessary to know the average diameter,  $\overline{D}$ , of the particles of each size fraction. For the 115 micron powder, the square screen openings are 0.125 and 0.105 mm on a side, respectively. The diameter used in this case is the average of these, 0.115 mm. For the 48 micron powder, the screen openings are 0.052 and 0.044 mm, respectively, and the average diameter in this case is 0.048 mm.

Equation (8) was used to calculate the number of particles per gram,  $P_\rho$ , for the two spherical size fractions. The number of particles per gram for the 48 and 115 micron spherical powders are  $1.93 \times 10^6$  and  $1.405 \times 10^5$ , respectively.

During the course of this work, all values of genus per unit volume were converted to genus per gram by dividing the value of genus per unit volume for the material by the density of the material. This was done because the specific volume of a sinter body generally decreases throughout the course of sintering and this volume change can mask changes occurring in the genus of the structure. For example, a sinter body can undergo shrinkage without any accompanying change

Table 6. Frequency of the number of contacts per particle for a sample of 115 micron spherical copper powder sintered to a density of 6.15 gm/cc ( $V_v = 0.314$ ).

Number of Contacts	Number of Particles	Frequency (%) = (Number of Particles/201) x 100
3	1	0.50
4	7	3.48
5	27	13.44
6	43	21.40
7	62	30.85
8	36	17.90
9	16	7.96
10	9	4.48
Total = 201		Total = 100

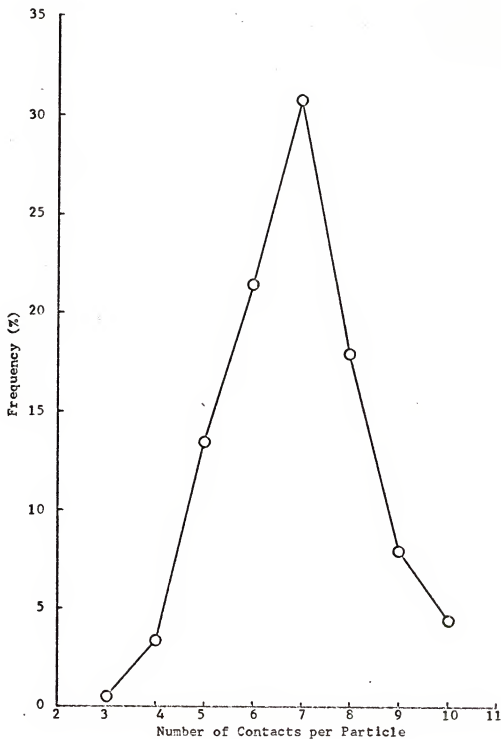


Figure 55. Frequency distribution of contacts per particle for 115 micron spherical copper powder sintered to a density of 6.15 gm/cc ( $V_v = 0.314$ ).

in its topological state; however, as a result of this shrinkage,  $G_V$  increases. Thus,  $G_V$  is not a desirable parameter to employ when monitoring the course of sintering. On the other hand,  $G_P$  is only affected by changes in the topological state of the structure and thus is a suitable parameter.

The values of  $G_P$  calculated from the data in Table 5 are plotted versus volume fraction of porosity,  $V_V$ , in Figure 56 for the 115 micron powder. These data points are designated  $G_P(\overline{C/P})$  to indicate that they were obtained by counting contacts per particle. The indicated spreads in the values of  $G_P(\overline{C/P})$  are a result of the  $\pm 5$  per cent confidence limits on the corresponding values of  $\overline{C/P}$ . The estimated range of  $\pm 1$  per cent in the values of density is also indicated.

Values of  $G_P^{\max}$  and  $G_P^{\min}$  were obtained for the 115 micron powder at densities of 6.67 gm/cc ( $V_V = 0.256$ ) and 7.05 gm/cc ( $V_V = 0.213$ ) by the method of analysis presented in Section 4.9 after this method of analysis was developed. The metal space of these samples was analyzed. In general, the space with the lowest volume fraction should be chosen for analysis, as pointed out in Section 6.13. This was not done for these two samples because the void space of the 7.05 gm/cc ( $V_V = 0.213$ ) sample was analyzed previously by the method of Kronsbein, *et al.* (Section 4.3) to determine  $G_P^{\max}$ . The metal space was therefore analyzed in order to check the results of the previous analysis. The metal space of the 6.67 gm/cc ( $V_V = 0.256$ ) sample was also analyzed since the results of the analysis of the metal space of the 7.05 gm/cc

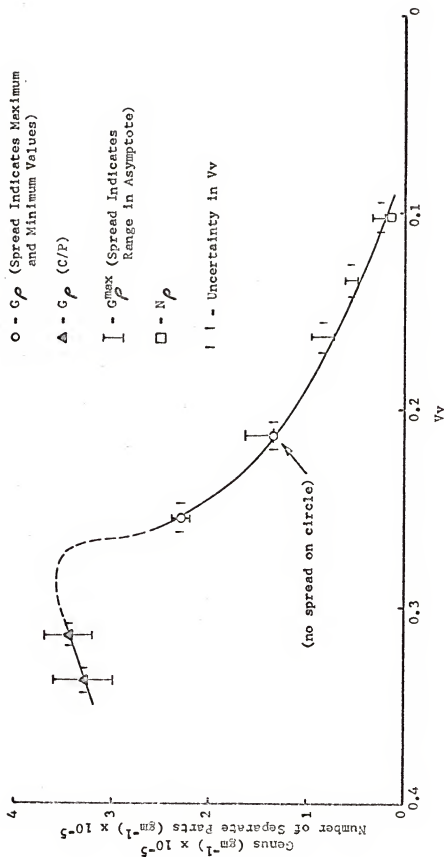


Figure 56. Genus per gram and number of separate parts per gram versus volume fraction of porosity for 115 micron spherical copper powder.

sample agreed well with the analysis of the void space. It is reasonable to expect the analysis of the metal space of a sample with a lower density to contain a smaller error (see Section 6.13). Therefore, the results of the analysis of the metal space of the 6.67 gm/cc sample should be in good agreement with the actual value of genus.

The plots of cumulative genus versus volume analyzed are presented in Figures 57 and 58 for the 6.67 and 7.05 gm/cc samples, respectively. The slopes of the lines through the data points were taken as the desired values of genus per unit volume. The values obtained are presented in Table 7 and in Figure 56. In this figure, the two values are represented by open circles. The value for the 6.67 gm/cc sample has an upper and lower limit obtained from the slopes of the plots of Figure 57. The value for the 7.05 gm/cc sample has no upper and lower limit, as the slopes of the maximum and minimum cumulative genus versus volume analyzed plots, shown in Figure 58, are the same within the scatter of the data. The reason for this is considered in Section 6.13.5.

Values of  $G_V^{\max}$  were also obtained for the 115 micron powder at pore volume fractions of 0.213, 0.163, 0.134 and 0.120 by applying the method of analysis presented in Section 4.3 to the void space of these samples. The analysis of these samples was performed before the technique of taking the slope of a plot of cumulative genus versus volume analyzed was developed. For each of these samples, a plot of the cumulative values of genus per unit volume versus number of sections analyzed was made. The value of

Table 7. Values of genus per gram for 115 micron spherical copper powder sintered to densities of 6.67 and 7.05 gm/cc.

Sample Density	Volume Fraction of Porosity	Maximum Genus per Unit Mass $G_{\rho_{\max}} \times 10^{-5}$	Minimum Genus per Unit Mass $G_{\rho_{\min}} \times 10^{-5}$
6.67	0.256	2.38	2.18
7.05	0.213	1.35*	1.35*

\*Slopes of the maximum and minimum curves could not be differentiated.

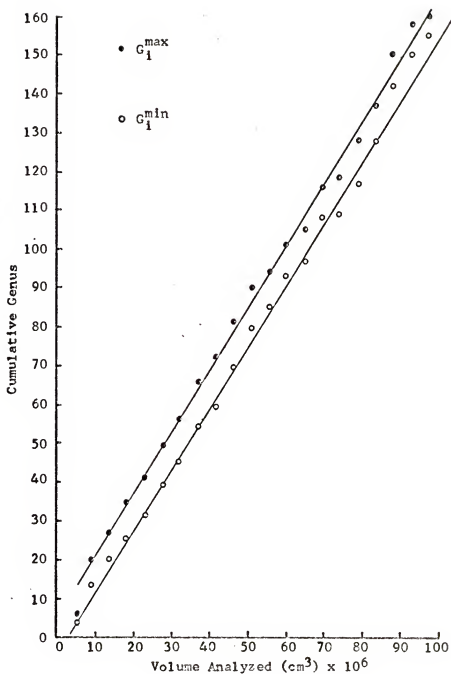


Figure 57. Cumulative genus versus volume analyzed for 115 micron spherical copper powder sintered to a density of 6.67 gm/cc ( $V_v = 0.256$ ).



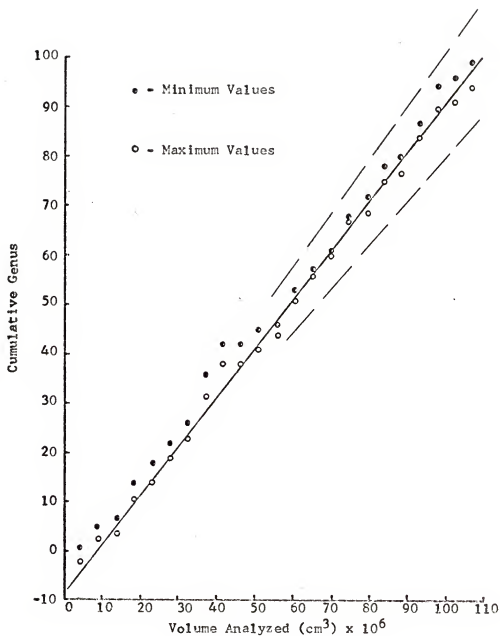


Figure 58. Cumulative genus versus volume of material analyzed for 115 micron spherical copper powder sintered to a density of 7.05 gm/cc ( $V_v = 0.213$ ).

the ordinate at which such a curve approaches zero slope is the desired value of  $G_v^{\max}$ , as indicated in Section 4.3. These curves are shown in Figure 59. The estimated range of the asymptote is indicated next to each curve. The ranges are drawn below the corresponding curves because, according to Steele [3], these curves converge slowly to the asymptotic value (see Appendix 1).

After the technique of taking the slope of a plot of cumulative number versus volume analyzed as the desired volume density had been developed by Steele [3] (see Section 4.6 and Appendix 1), these plots were made for the samples under consideration. However, the number of sections analyzed was not large enough to allow the slopes to be determined to greater accuracy than the ranges indicated for the asymptotes in Figure 59. Therefore, these ranges are used as the limits on the values of  $G_v^{\max}$  for each of the corresponding samples. These values are converted to values of  $G_p^{\max}$  and plotted versus pore volume fraction in Figure 56. These values are also presented in Table 8. The indicated ranges correspond to the maximum and minimum limits of the estimated range of the asymptote. The estimated range of  $\pm 1$  per cent in the values of density is also indicated. The bottom of the spread is taken as the actual value of genus per gram because, as mentioned above, these curves converge slowly to the asymptotic value.

#### 5.2.2 Number of Separate Parts per Gram Data

Only one value of separate parts per gram was determined for the 115 micron powder. The material with a density of 8.05 gm/cc was serial sectioned by standard metallographic polishing procedures

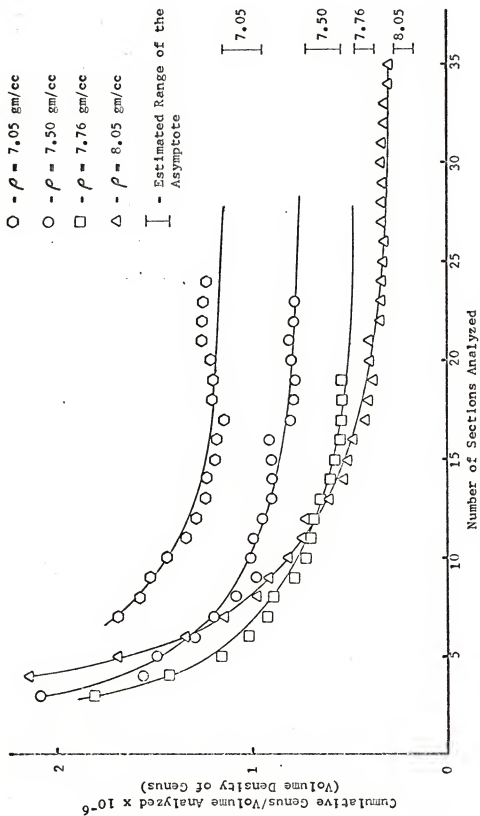


Figure 59. Cumulative genus/volume analyzed versus number of sections analyzed for four samples of 115 micron spherical copper powder sintered to the indicated densities.

(see Section 3.5), which allows the detection of separate parts. The remaining samples of the 115 micron powder were serial sectioned with a microtome after infiltrating the void space with solder (see Section 3.5). Since separate parts are not filled with solder by this process, they can be smeared over, and therefore not observed when the sample is cut by the microtome.

The number of separate parts per gram for the 8.05 gm/cc sample is given in Figure 56 and in Table 8. The number of separate parts per unit volume for this sample was determined from the slope of the plot of cumulative number of separate parts versus volume analyzed shown in Figure 60. Since linearity appears to have been reached in this plot, even with the few data points obtained, the slope is taken as the number of separate parts per unit volume rather than the asymptote of the plot of cumulative volume density of separate parts versus volume analyzed. This latter curve is also shown in Figure 60. The slope of the cumulative number curve is taken as the value of the asymptote indicated in this figure.

The 115 micron size fraction has a small amount of gas porosity in the as-manufactured state. Some gas pores can be seen in Figure 36. It was estimated from serial sections through the low density samples that about one particle in 25 contains an internal gas pore. This is equivalent to  $0.50 \times 10^5$  pores per gram of material. Thus, more than one-third of the separate parts present in the 8.05 gm/cc sample could be gas porosity. The actual contribution of gas porosity is probably less than this as most of the gas pores are small (10 microns or less), and therefore may

Table 8. Genus per gram and number of separate parts per gram data for 115 micron spherical copper powder sintered to four different densities.

Density	Pore Volume Fraction V <sub>v</sub>	Upper Limit		Lower Limit	
		G <sub>v</sub> × 10 <sup>-6</sup> (cc <sup>-1</sup> )	G <sub>p</sub> × 10 <sup>-5</sup> (gm <sup>-1</sup> )	G <sub>v</sub> × 10 <sup>-6</sup> (cc <sup>-1</sup> )	G <sub>p</sub> × 10 <sup>-5</sup> (gm <sup>-1</sup> )
7.05	0.213	1.150	1.631	0.950	1.348
7.50	0.163	0.725	0.967	0.550	0.734
7.76	0.134	0.475	0.612	0.375	0.483
8.05	0.102	0.275	0.342	0.175	0.217

Number of Separate Parts

<u>Density</u>	<u>Pore Volume Fraction V<sub>v</sub></u>	
8.05	0.102	$N_p = 0.15 \times 10^5 (\text{g}^{-1})$

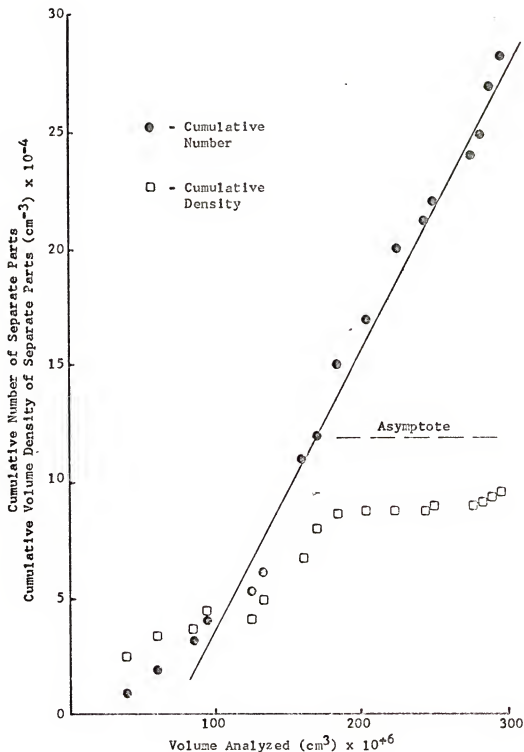


Figure 60. Cumulative number and cumulative volume density of separate parts versus volume analyzed for 115 micron spherical copper powder sintered to a density of 8.05 gm/cc ( $V_v = 0.102$ ).

disappear early in the sintering process. Thus, the number of separate parts per unit volume determined from the slope of the cumulative number plot of Figure 60 is taken as the actual value. It should be noted, however, that gas porosity may contribute to this value.

### 5.3 Topological Properties of the 48 Micron Spherical Powder

#### 5.3.1 Genus per Gram Data

A plot of genus per gram versus volume fraction of porosity for the 48 micron spherical powder is shown in Figure 61. The genus of the two low-density samples was determined from the contacts per particle data presented in Table 5. The void space of each of the other five samples of this size fraction was analyzed by means of Method II, which was presented in Section 4.5. The cumulative genus versus volume analyzed plots for these samples are presented in Figures 62 to 66. The values of  $G_p^{\max}$  and  $G_p^{\min}$  which were determined from the slopes of the lines through the data points are given in Table 9 and plotted versus pore volume fraction in Figure 61. The estimated 1 per cent uncertainty in the values of density is also indicated for each data point in Figure 61. The maximum value of genus is taken as the value of genus for the 6.62 gm/cc ( $V_v = 0.261$ ) sample because a small number of closed channels were observed for this material, as can be seen in Figure 41. Therefore, the genus must decrease with any further sintering. Recall that contacts per particle are not used to determine the genus after channel closure has begun. However, very few closed channels are present in this material so the value of genus

Table 9. Values of genus per gram for the 48 micron spherical copper powder sintered to densities of 7.26, 7.74, 8.00, 8.25 and 8.40 gm/cc.

Sample Density (gm/cm <sup>3</sup> )	Volume Fraction Porosity	$G_p \text{ max} \times 10^{-6}$	$G_p \text{ min} \times 10^{-6}$
7.26	0.190	1.20	1.08
7.74	0.136	0.62	0.49
8.00	0.107	0.32	0.23
8.25	0.079	0.058	0.02
8.40	0.062	0	0



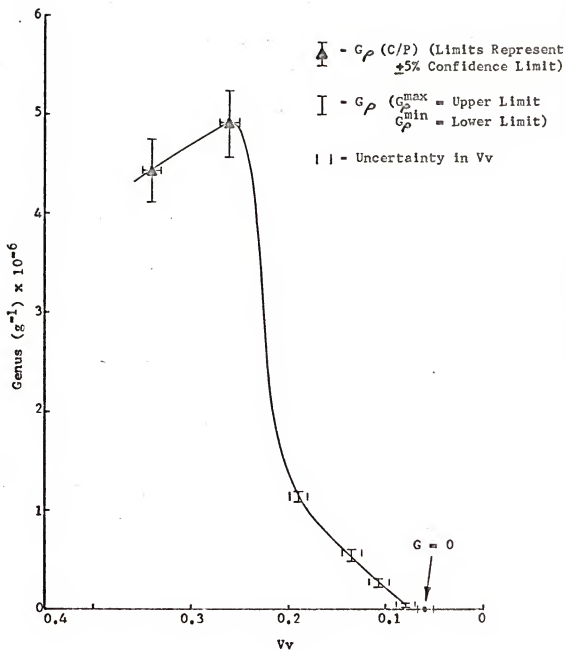


Figure 61. Genus per gram versus volume fraction of porosity for 48 micron spherical copper powder.

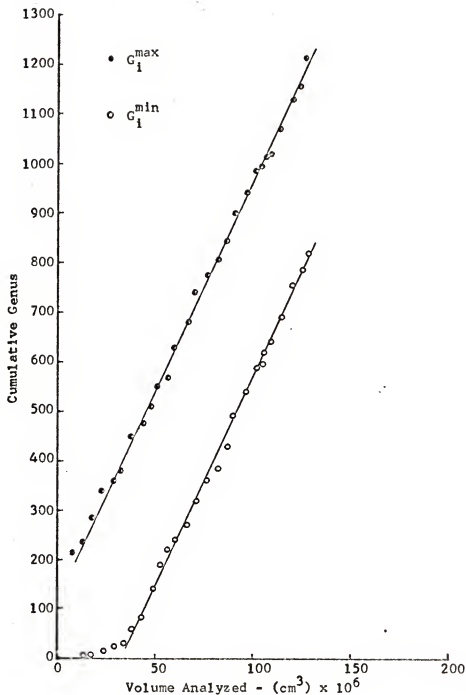


Figure 62. Cumulative genus versus volume analyzed for 48 micron spherical copper powder sintered to a density of 7.26 gm/cc.

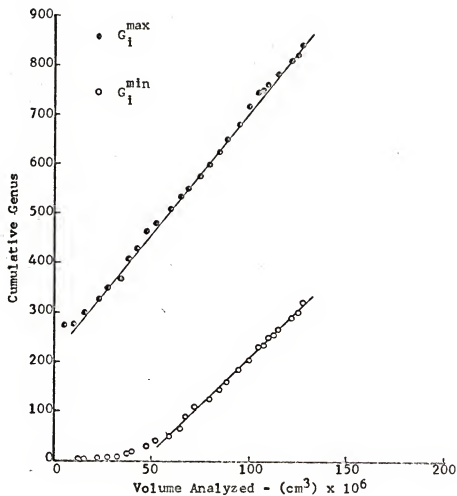


Figure 63. Cumulative genus versus volume analyzed for 48 micron spherical copper powder sintered to a density of 7.74 gm/cc.

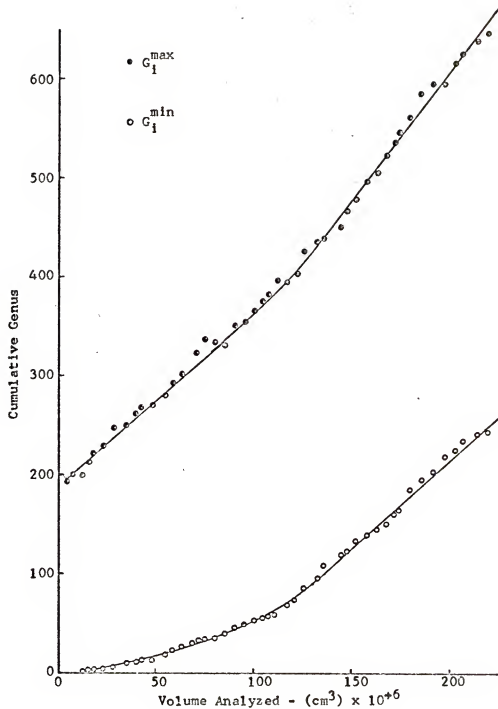


Figure 64. Cumulative genus versus volume analyzed for 48 micron spherical copper powder sintered to a density of 8.00 gm/cc.

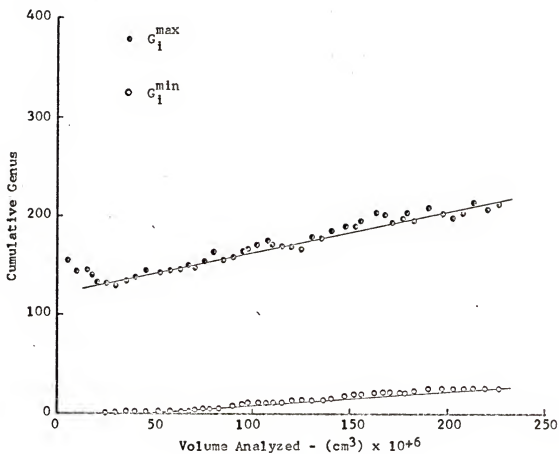


Figure 65. Cumulative genus versus volume analyzed for 48 micron spherical copper powder sintered to a density of 8.25 gm/cc.

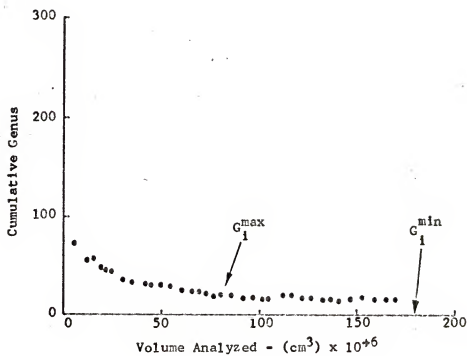


Figure 66. Cumulative genus versus volume analyzed for 48 micron spherical copper powder sintered to a density of 8.40 gm/cc.

obtained by counting contacts per particle contains negligible error as a result of their presence.

### 5.3.2 Number of Separate Parts per Gram Data

The values of separate parts per gram for the five samples of the 48 micron spherical powder with densities greater than 7.0 gm/cc are plotted versus volume fraction of porosity in Figures 67 and 99. The respective plots of cumulative number of separate parts versus volume analyzed are shown in Figures 68 to 72. The solid lines through the data points were used to determine the slopes of the curves. Two plots are shown in each figure; one represents all separate parts observed, and the other separate parts appearing on two or more serial sections. The latter are referred to as large separate parts. The small separate parts, those appearing on only one serial section, are less than 8.6 microns in diameter, which is the average distance between three serial sections. These small separate parts are all nearly spherical in shape. This is attributed to their small size which allows surface rounding to occur rapidly so that any irregularities are quickly removed.

The number of small separate parts per gram varies with increasing density in such a way that it is improbable that they are the result of pits produced during the polishing of the samples. Also recall that the solid-copper ring around the samples was checked to ensure that pits were not formed as a result of the polishing process.

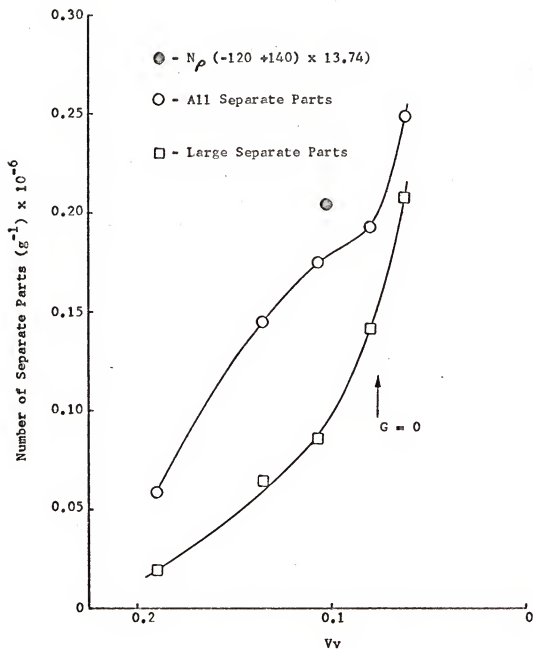


Figure 67. Number of separate parts per gram (all and large) versus volume fraction of porosity for 48 micron spherical copper powder.



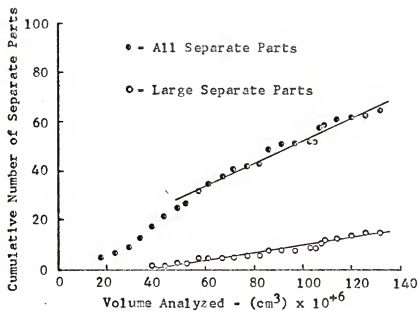


Figure 68. Cumulative number of separate parts versus volume analyzed for 48 micron spherical copper powder sintered to a density of 7.26 gm/cc.

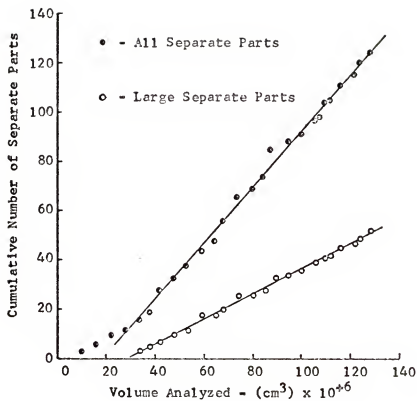


Figure 69. Cumulative number of separate parts versus volume analyzed for 48 micron spherical copper powder sintered to a density of 7.74 gm/cc.

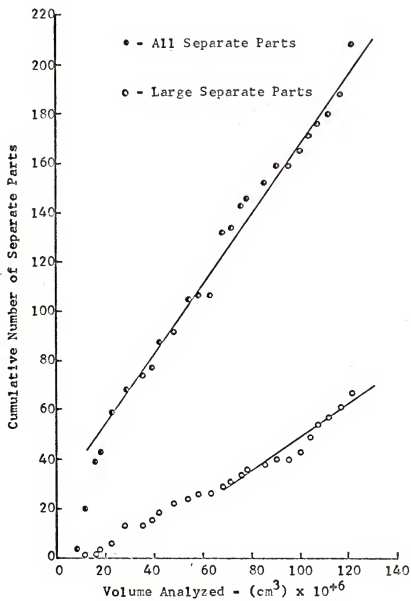


Figure 70. Cumulative number of separate parts versus volume analyzed for 48 micron spherical copper powder sintered to a density of 8.00 gm/cc.

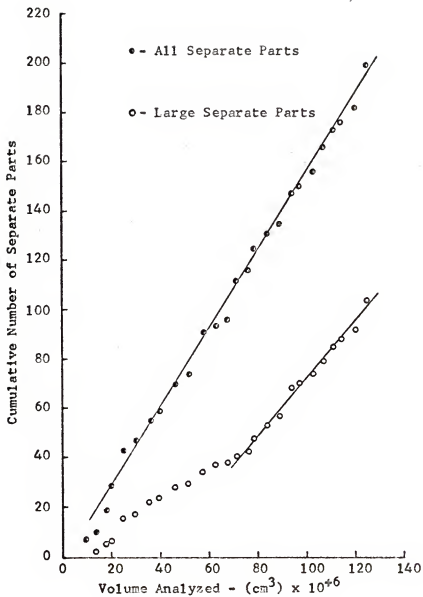


Figure 71. Cumulative number of separate parts versus volume analyzed for 48 micron spherical copper powder sintered to a density of 8.25 gm/cc.

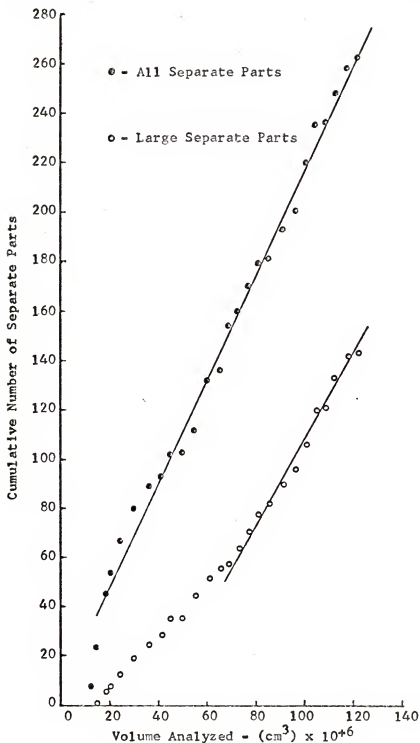


Figure 72. Cumulative number of separate parts versus volume analyzed for 48 micron spherical copper powder sintered to a density of 8.40 gm/cc.

The values of separate parts per gram shown in Figure 67 were determined from the slopes of the respective plots of all separate parts versus volume analyzed. The values of number of separate parts per gram obtained from the slopes of the curves shown in Figures 68 to 72 are given in Table 10. The total number of separate parts, also referred to as all separate parts, is equal to the sum of the number of large and small separate parts.

The total number of separate parts and the number of large separate parts are plotted versus  $V_V$  in Figure 67. The number of small separate parts is plotted versus  $V_V$  in Figure 99. The total number of separate parts is again plotted in Figure 99.

#### 5.4 Topological Properties of the 48 Micron Electrolytic Powder

##### 5.4.1 Genus per Gram Data

A plot of genus per gram versus volume fraction of porosity for the 48 micron electrolytic powder is shown in Figure 73. The genus of the five lowest density samples was determined by analyzing the metal space of the structures by means of Method III (see Sections 4.8 and 4.9). The cumulative genus versus volume analyzed plots for these samples are presented in Figures 74 to 78. The void space of the sample with a density of 6.05 gm/cc was also analyzed. The cumulative genus versus volume analyzed plot for this sample is presented in Figure 79. The genus of the remaining two highest density samples was determined by analyzing the void space of the structures. The cumulative genus versus volume analyzed plots for these samples are presented in Figures 80 and 81.

Table 10. Number of separate parts per gram data for the 48 micron spherical and electrolytic copper powders.

Sample Density (gm/cm <sup>3</sup> )	Volume Fraction Porosity	Total Number of Separate Parts Per Gram x 10 <sup>-6</sup>	Number of Large Separate Parts Per Gram x 10 <sup>-6</sup>	Number of Small Separate Parts Per Gram x 10 <sup>-6</sup>
<u>-270 +325 Mesh Spherical Powder</u>				
7.26	0.190	0.0593	0.0196	0.0397
7.74	0.136	0.145	0.0646	0.080
8.00	0.107	0.175	0.0863	0.088
8.25	0.079	0.193	0.142	0.051
8.40	0.062	0.249	0.208	0.041
<u>-270 +325 Mesh Electrolytic Powder</u>				
4.96	0.446	0	-	-
6.05	0.325	0.105	-	-
6.95	0.224	0.272	-	-
7.92	0.116	0.402	0.281	0.121
8.45	0.057	0.0829 to 0.109	-	-

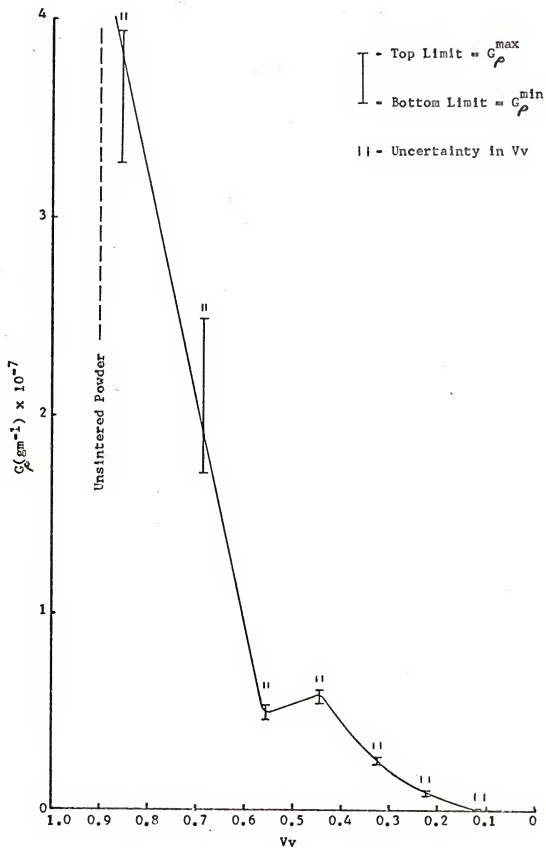


Figure 73. Genus per gram versus volume fraction of porosity for 48 micron electrolytic copper powder.



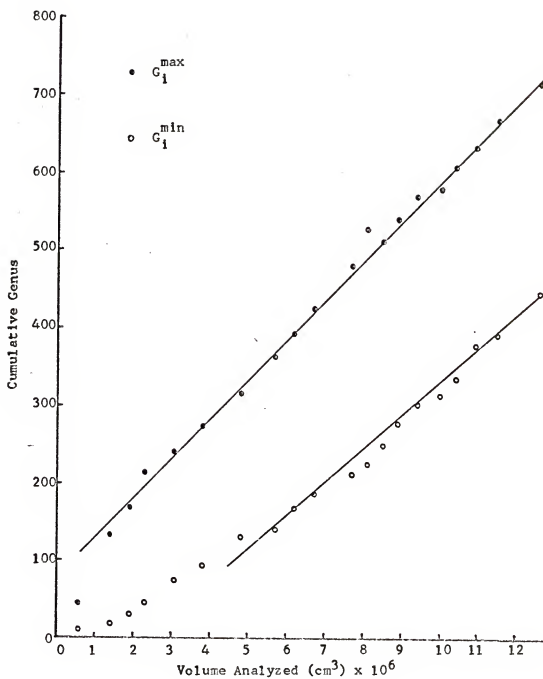


Figure 74. Cumulative genus versus volume analyzed for 48 micron electrolytic copper powder sintered to a density of 1.30 gm/cc obtained by analysis of the metal space.

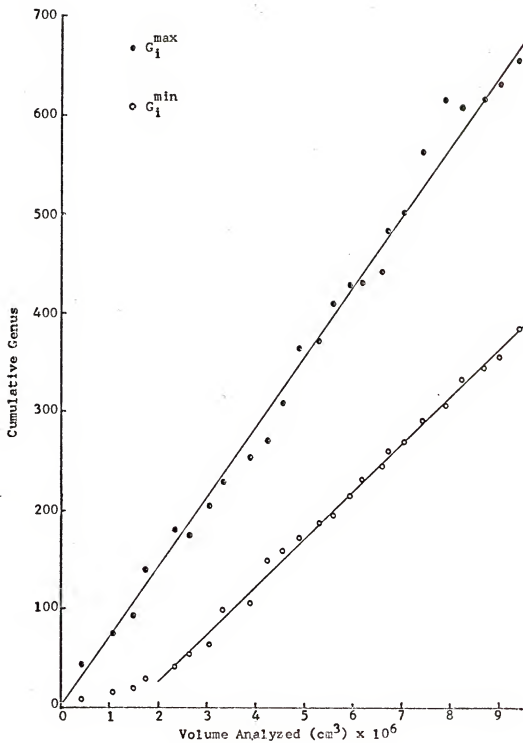


Figure 75. Cumulative genus versus volume analyzed for 48 micron electrolytic copper powder sintered to a density of 2.81 gm/cc obtained by analysis of the metal space.

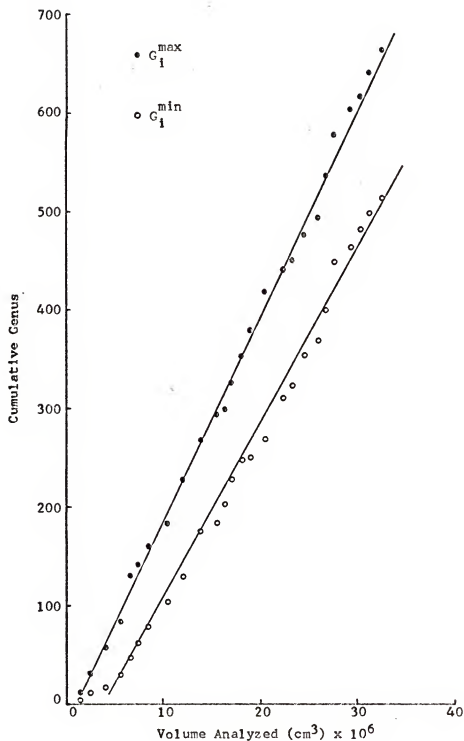


Figure 76. Cumulative genus versus volume analyzed for 48 micron electrolytic copper powder sintered to a density of 3.99 gm/cc obtained by analysis of the metal space.

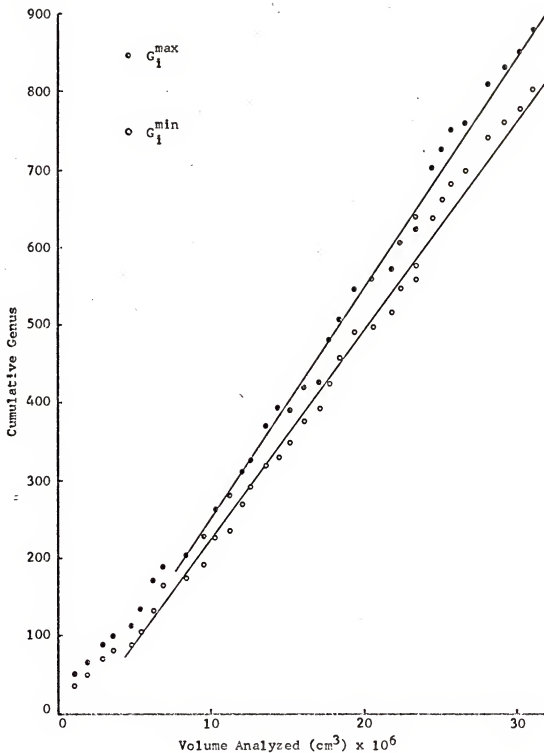


Figure 77. Cumulative genus versus volume analyzed for 48 micron electrolytic copper powder sintered to a density of 4.96 gm/cc obtained by analysis of the metal space.

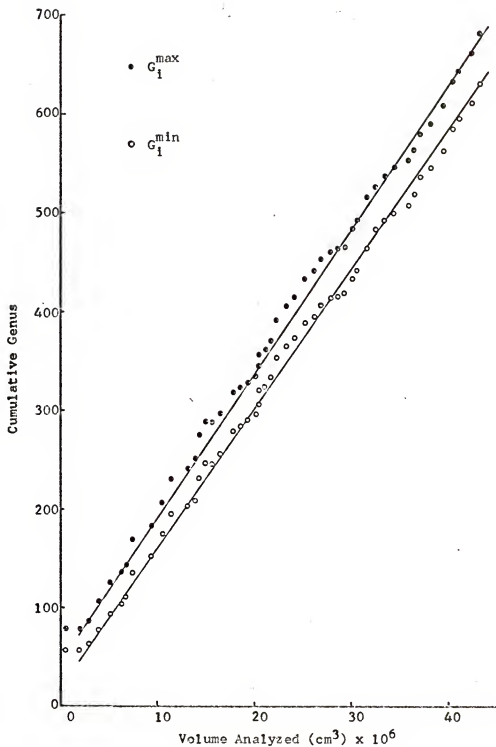


Figure 78. Cumulative genus versus volume analyzed for 48 micron electrolytic copper powder sintered to a density of 6.05 gm/cc obtained by analysis of the metal space.

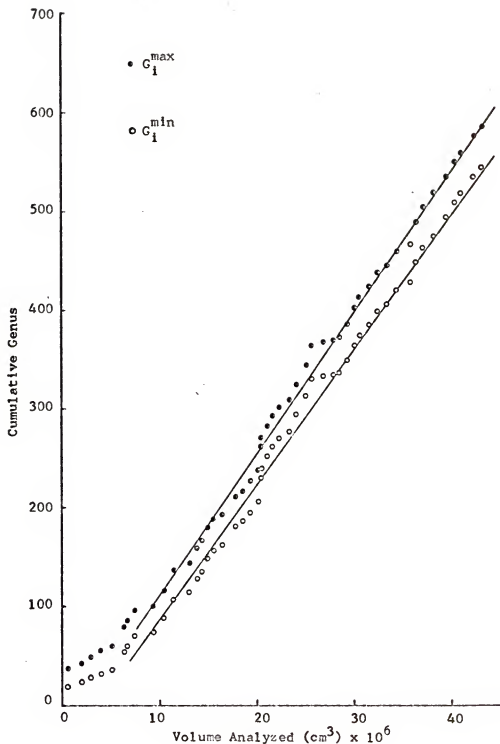


Figure 79. Cumulative genus versus volume analyzed for 48 micron electrolytic copper powder sintered to a density of 6.05 gm/cc obtained by analysis of the void space.

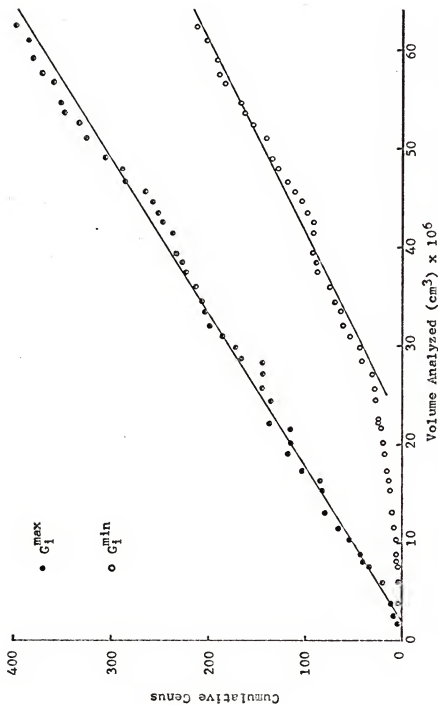


Figure 80. Cumulative genus versus volume analyzed for 48 micron electrolytic copper powder sintered to a density of 6.95 gm/cc obtained by analysis of the void space.

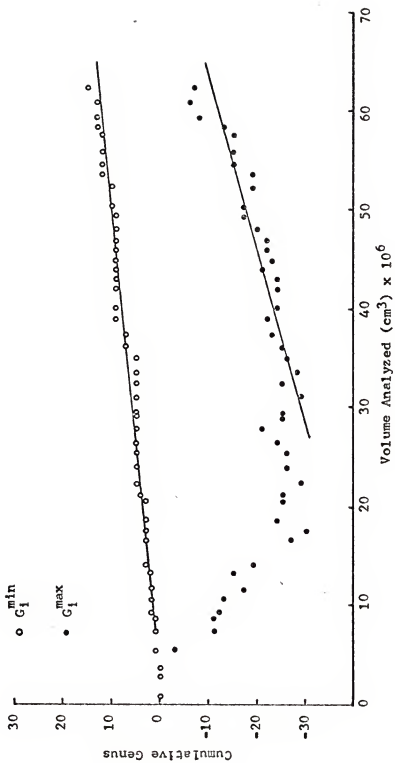


Figure 81. Cumulative genus versus volume analyzed for 48 micron electrolytic copper powder sintered to a density of 7.92 gm/cc obtained by analysis of the void space.



The values of  $G_{\rho}^{\max}$  and  $G_{\rho}^{\min}$  which were determined from the slopes of the lines through the curves in Figures 74 to 81 are given in Table 11 and plotted versus volume fraction of porosity in Figure 73. The estimated 1 per cent uncertainty in the values of density is indicated by the vertical bars above each data point in Figure 73.

#### 5.4.2 Number of Separate Parts per Gram Data

The values of separate parts per gram for the electrolytic powder are given in Table 10 and plotted versus volume fraction of porosity in Figure 82. The respective plots of cumulative number of separate parts versus volume analyzed are shown in Figures 83, 84 and 85. The solid lines through the data points were used to determine the slopes of the curves. The number of small separate parts was determined for only one sample at a density of 7.92 gm/cc. These small separate parts appear on only one serial section and are less than 3.2 microns in diameter. This is the average distance between three serial sections employed in the analysis of the electrolytic powder. As pointed out in Section 5.5, these small separate parts are nearly spherical in shape. The number of large separate parts given in Table 10 for the 7.92 gm/cc sample represents the difference between the total number of separate parts and the number of small separate parts.

The number of separate parts given in Table 10 for the 8.45 gm/cc sample was not obtained by means of the serial sectioning technique. This sample was not included in the seven samples of the electrolytic powder which were serial sectioned together. The

Table 11. Values of genus per gram for the 48 micron electrolytic copper powder.

Sample Density (gm/cm <sup>3</sup> )	Volume Fraction Porosity	$G_p \text{ max} \times 10^{-6}$	$G_p \text{ min} \times 10^{-6}$
1.30	0.855	39.4	32.8
2.81	0.686	24.9	17.1
3.99	0.555	5.33	4.62
4.96	0.446	6.10	5.48
6.05	0.325	2.52	2.27
6.95	0.224	0.917	0.731
7.92	0.116	0.0683	0.0283

$\Delta$  - Electrolytic (Total Number of Separate Parts)

$\square$  - Electrolytic (Small Separate Parts)

$\circ$  - Spherical (Total Number of Separate Parts)

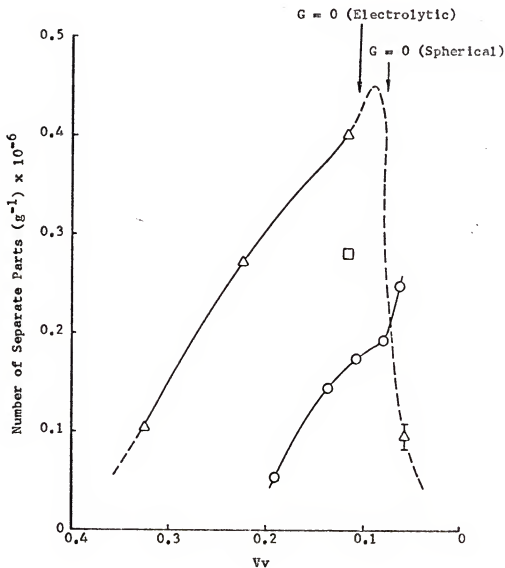


Figure 82. Number of separate parts per gram versus volume fraction of porosity for 48 micron spherical and electrolytic copper powders.

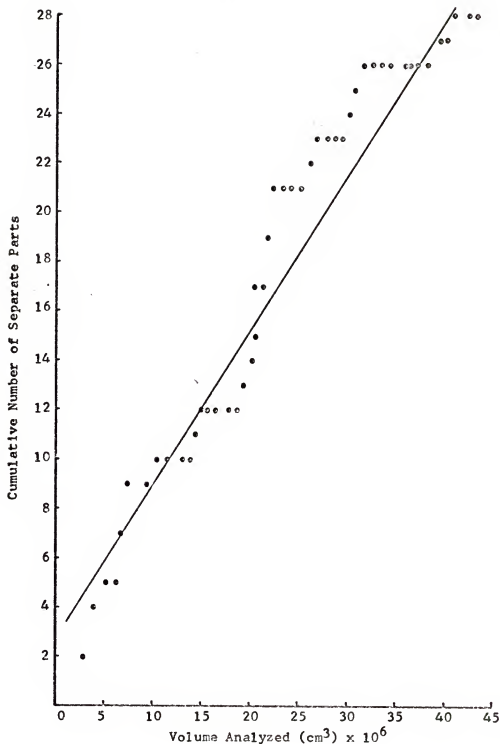


Figure 83. Cumulative number of separate parts versus volume analyzed for 48 micron electrolytic copper powder sintered to a density of 6.05 gm/cc.

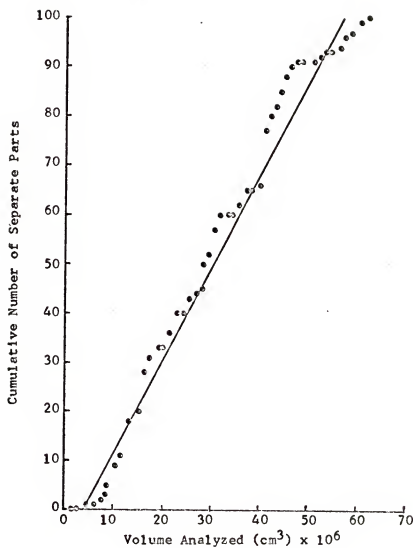


Figure 84. Cumulative number of separate parts versus volume analyzed for 48 micron electrolytic copper powder sintered to a density of 6.95 gm/cc.

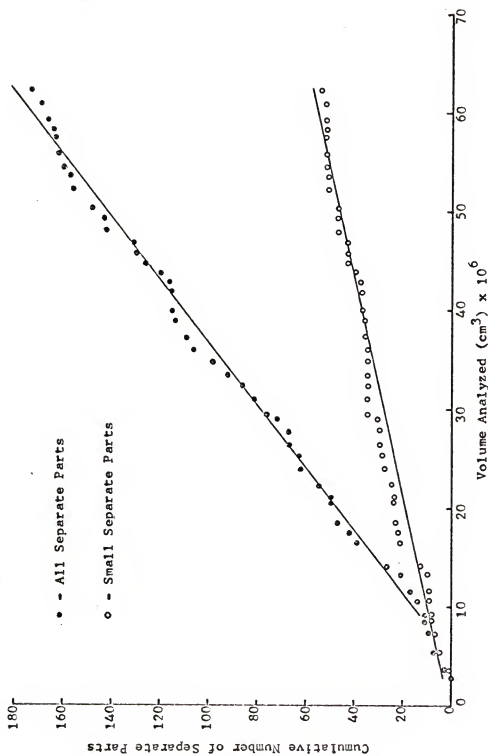


Figure 85. Cumulative number of separate parts versus volume analyzed for 48 micron electrolytic copper powder sintered to a density of 7.92 gm/cc.

analysis of the seven samples was completed before it was decided to analyze the 8.45 gm/cc material. It is apparent from Figure 73 that this structure has a genus of zero and consists entirely of isolated separate parts. It was decided not to serial section this structure as an estimate of the number of separate parts per unit volume could be obtained more easily as follows.

The number of separate parts per unit volume was determined by application of the quantitative metallographic relation [25]

$$N_A = N_V \bar{D} \quad (19)$$

where  $N_A$  is the number of features, in this case separate parts, intersecting unit area of test plane through the structure,  $N_V$  is the number of separate parts per unit volume and  $\bar{D}$  is the average distance in the void space between pairs of parallel planes tangent to the separate parts. The test plane in this case is a microsection through the sinter structure. The value of  $N_A$  is determined by counting the number of separate parts which intersect unit area of microsection. In order to estimate  $N_V$  by means of equation (19),  $\bar{D}$  must be determined. An estimate of  $\bar{D}$  was obtained for the 8.45 gm/cc sample of the electrolytic powder as follows.

The value of the mean pore intercept in the void space,  $\bar{\lambda}$ , is given by the relation [26]

$$\bar{\lambda} = \frac{4V_V}{S_V} \quad (20)$$

where  $V_V$  is the volume fraction of porosity and  $S_V$  is the surface area of void-solid interface per unit volume. For a given microstructure, the value of  $\bar{D}$  is related to  $\bar{\lambda}$  by a geometric factor,  $k$ ,

$$\bar{D} = k\bar{\lambda} \quad (21)$$

where  $k$  depends upon the shape and size distribution of the elements of porosity. For an aggregate of spheres of uniform size,  $k = 3/2$ ; however, the isolated separate parts are neither spherical nor uniform in size, therefore,  $k > 3/2$ .

If  $k$  is assumed to have a value of 1.5 to 2.0 and equations (19), (20) and (21) are applied to the 8.40 gm/cc sample of the spherical copper powder, a value of  $N_V$  which is in good agreement with that determined by means of the serial section analysis is obtained. The range for  $N_V$  given in the fourth row of Table 12, calculated in this way, includes the value of  $N_V$  given in the last row which was obtained from the serial section analysis.

If the value of  $k$  for the 8.45 gm/cc sample of the electrolytic powder is assumed to be 1.5 to 2.0, which is not unreasonable since the separate parts should have approximately the same size and shape distribution as those in the 8.40 gm/cc sample of the spherical powder, then equations (19), (20) and (21) can be used to determine  $N_V$  for this sample. The range for  $N_V$  given in the fourth row of Table 12 was obtained in this way and is used as an estimate of  $N_V$  for the 8.45 gm/cc sample of the 48 micron electrolytic powder.

## 5.5 Metric Properties of the 48 Micron Spherical and Electrolytic Powders

### 5.5.1 Surface Area Data

Plots of surface area of pore-solid interface per unit volume and per unit mass versus volume fraction of porosity are shown in Figure 86 for the 48 micron spherical and electrolytic copper powders.



Table 12. Values of parameters used in the estimation of the number of separate parts per gram for 48 micron electrolytic copper powder sintered to a density of 8.45 gm/cc.

	8.45 gm/cm <sup>3</sup> -270 +325 Mesh Electrolytic	8.40 gm/cm <sup>3</sup> -270 +325 Mesh Spherical
$N_A$ (cm <sup>-2</sup> ) (measured)	4610	8120
$\bar{\lambda}$ (cm <sup>-1</sup> ) $\times 10^4$ [from equation (20)]	35	25
$\bar{D}$ (cm <sup>-1</sup> ) $\times 10^4$ (from $\bar{\lambda}$ )	50 to 65	35 to 45
$N_V$ (cm <sup>-3</sup> ) $\times 10^{-6}$ [from equation (19)]	0.709 to 0.921	1.99 to 2.32
$N_\rho$ (g <sup>-1</sup> ) $\times 10^{-6}$ (converted from the above value)	0.083 to 0.109	0.236 to 0.276
$N_\rho$ (g <sup>-1</sup> ) $\times 10^{-6}$ (from serial section analysis)	-	0.249
$N_V$ (cm <sup>-3</sup> ) $\times 10^{-6}$ (from serial section analysis)	-	2.18

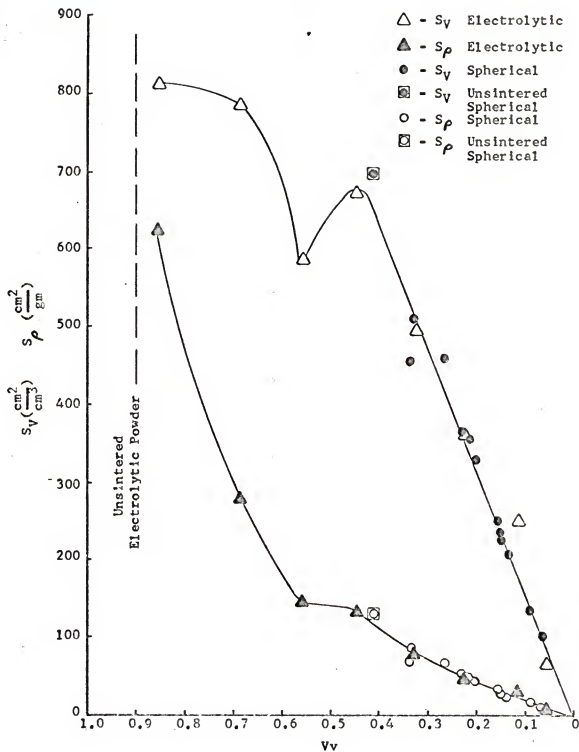


Figure 86. Surface area per unit volume and surface area per unit mass versus volume fraction of porosity for 48 micron spherical and electrolytic copper powders.

These data are also presented in Table 13. The values of surface area per unit volume were obtained from line intercept counts made on microsections through the structures. The surface area per unit volume,  $S_V$ , is given by

$$S_V = 2N_L \quad (22)$$

where  $N_L$  is the average number of intersections that unit length of test line makes with the void-solid interface [26].

The values of surface area per unit mass were obtained by dividing the values of surface area per unit volume by the respective sample densities. The surface area per unit volume of the unsintered spherical powder was calculated from the particle size and the density of the unsintered powder.

### 5.5.2 Curvature Data

Values of total curvature per unit volume,  $M_V$ ,\* are presented in Table 14 and plotted against pore volume fraction in Figure 87. In order to determine the values of total curvature per unit volume, a tangent count [4] is made on a microsection through the structure.

---

\*The total curvature per unit volume is defined by the relation

$$M_V \equiv \bar{H} S_V$$

where  $S_V$  is the surface area per unit volume and  $\bar{H}$  is the average mean surface curvature. The mean surface curvature,  $H$ , of an element of surface is defined here by

$$H \equiv \frac{1}{r_1} + \frac{1}{r_2}$$

where  $r_1$  and  $r_2$  are the principal normal radii of curvature of the surface element [4]. [It should be noted that  $H$  may be defined as  $\frac{1}{2}(\frac{1}{r_1} + \frac{1}{r_2})$ ; e.g., in the mathematical literature.]

Table 13. Surface area per unit volume and per unit mass for 48 micron spherical and electrolytic copper powders sintered to the indicated densities.

Sample Density (gm/cm <sup>3</sup> )	Volume Fraction Porosity V <sub>v</sub>	Surface Area per Unit Volume S <sub>v</sub> (cm <sup>2</sup> /cm <sup>3</sup> )	Surface Area per Unit Mass S <sub>p</sub> (cm <sup>2</sup> /gm)
<u>-270 +325 Spherical (Gregg [27])</u>			
5.20*	0.420	700	133.0
5.90	0.340	458	77.7
5.98	0.332	520	87.0
6.57	0.266	460	70.0
6.90	0.230	362	52.5
7.02	0.216	356	50.7
7.16	0.201	330	46.1
7.55	0.157	250	33.1
7.60	0.152	226	29.8
7.60	0.152	235	30.9
7.73	0.137	218	28.2
8.18	0.088	137	16.8
8.40	0.062	101	12.0**
<u>-270 +325 Electrolytic **</u>			
0.9*	0.900	-	-
1.30	0.855	811	624
2.81	0.686	785	280
3.99	0.555	587	147
4.96	0.446	676	136
6.05	0.325	496	82
6.95	0.224	358	51
7.92	0.116	250	32
8.45	0.057	65	7.7

\*Unsintered powder.

\*\*Values determined during the course of this research.

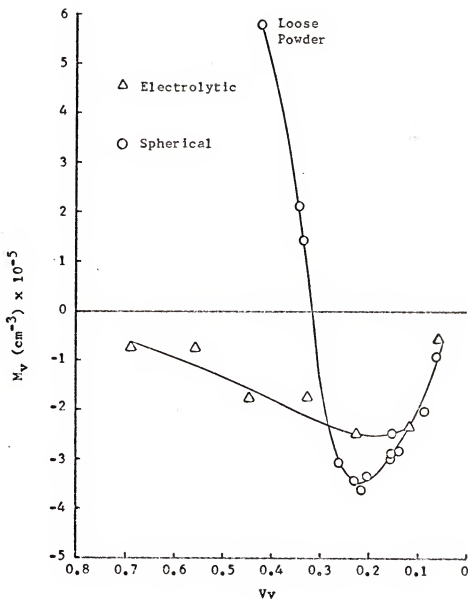


Figure 87. Total curvature per unit volume versus volume fraction of porosity for 48 micron spherical and electrolytic copper powders.

The total curvature per unit volume is then obtained from the relation [4]

$$M_V = 2\pi T_{Anet} \quad (23)$$

where  $T_{Anet}$  is the net tangent count per unit area of microsection [28].

The values of average mean surface curvature,  $\bar{H}$ , are also presented in Table 14. These values are plotted against pore volume fraction in Figure 88. The average mean surface curvature is given by the relation [4]

$$\bar{H} = \frac{M_V}{S_V} \quad (24)$$

where  $M_V$  and  $S_V$  are the total curvature per unit volume and surface area per unit volume, respectively.

### 5.5.3 Grain Size and Grain Boundary Area Data

Values of grain boundary area per unit volume,  $S_{Vgb}$ , are presented in Table 15 and are plotted against pore volume fraction in Figure 89. These data were obtained by determining  $N_{Lgb}$ , the average number of intersections that unit length of test line makes with grain boundaries on a microsection through the respective structures. The values of  $S_{Vgb}$  were then determined from the relation

$$S_{Vgb} = 2N_{Lgb} \quad (25)$$

which is equation (22) applied to grain boundaries rather than pore-solid interface.

The values of grain boundary area per unit mass,  $S_{\rho gb}$ , presented in Table 15, were obtained by dividing the respective

Table 14. Curvature data for the 48 micron spherical and electrolytic copper powders.

Sample Density (gm/cm <sup>3</sup> )	Volume Fraction Porosity V <sub>v</sub>	Total Curvature per Unit Volume M <sub>v</sub> (cm <sup>-3</sup> )×10 <sup>-5</sup>	Average Mean Surface Curvature H(cm <sup>-1</sup> )
<u>-270 +325 Spherical</u>			
5.20	0.420	5.83	833*
5.90	0.340	2.13	466
5.98	0.332	1.41	272
6.57	0.266	-3.09	-682
6.90	0.230	-3.42	-946
7.02	0.216	-3.60	-1010
7.16	0.201	-3.34	-1011
7.55	0.157	-2.97	-1189
7.60	0.152	-2.48	-1098
7.60	0.152	-2.89	-1230
7.73	0.137	-2.82	-1297
8.18	0.088	-2.01	-1468
8.40	0.062	-0.925	-918**
<u>-270 +325 Electrolytic**</u>			
1.30	0.855	-	-
2.81	0.686	-0.704	-89.6
3.99	0.555	-0.754	-128
4.96	0.446	-1.75	-258
6.05	0.325	-1.72	-347
6.95	0.224	-2.47	-689
7.92	0.116	-2.33	-932
8.45	0.057	-0.551	-848

\*Unsintered powder.

\*\*[29].

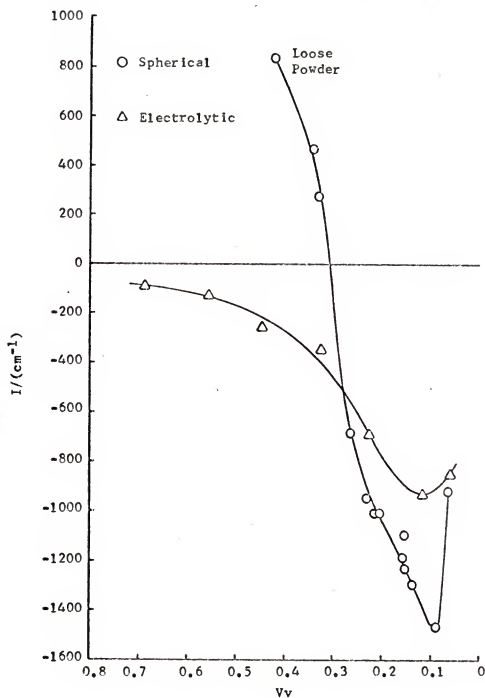


Figure 88. Average mean surface curvature versus volume fraction of porosity for 48 micron spherical and electrolytic copper powders.



Table 15. Grain size and grain boundary area data for the 48 micron spherical and electrolytic copper powders.

Sample Density (gm/cm <sup>3</sup> )	Volume Fraction Porosity Vv	Grain Boundary Area per Unit Volume S <sub>gb</sub> (cm <sup>2</sup> /cm <sup>3</sup> )	Grain Boundary Area per Unit Mass S <sub>p</sub> (cm <sup>2</sup> /gm)	Total Grain Surface Area per Unit Volume ST(V) <sub>gb</sub> (cm <sup>2</sup> /cm <sup>3</sup> )	Total Grain Surface Area per Unit Mass ST(P) <sub>gb</sub> (cm <sup>2</sup> /gm)	Mean Grain Intercept $\bar{\lambda}_{gr}$ (cm)x10 <sup>4</sup>
<u>-270 +325 Spherical</u>						
5.20*	0.420	0	0	700	135	32
5.91	0.340	47	8	644	109	41
6.62	0.261	138	21	726	110	40
7.26	0.190	240	33	810	111	40
7.74	0.136	287	37	783	103	44
8.00	0.107	191	24	557	70	64
8.25	0.079	97	12	344	42	107
8.40	0.062	56	6.7	172	20	172
<u>-270 +325 Electrolytic</u>						
3.99	0.555	197	49	1014	254	17
4.96	0.446	248	50	1172	236	19
6.05	0.325	236	39	968	160	28
6.95	0.224	230	33	818	118	38
7.92	0.116	207	26	663	84	52
8.45	0.057	66	7.8	197	23	193

\*Unsintered powder.

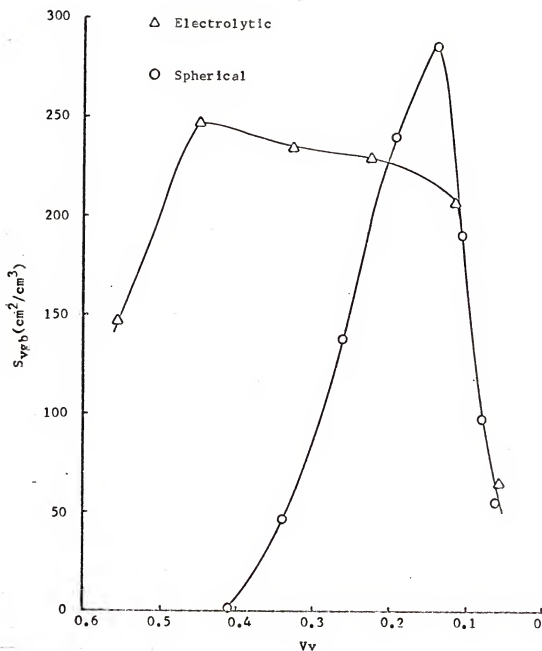


Figure 89. Grain boundary area per unit volume versus volume fraction of porosity for 48 micron spherical and electrolytic copper powders.

values of grain boundary area per cc by the sample densities. The values of grain boundary area per gram are plotted against pore volume fraction in Figure 90.

Values of total grain surface area per unit volume,  $S_{VT}$ , are also presented in Table 15. These values are given by

$$S_{VT} = S_V + 2S_{Vgb} \quad (26)$$

since grains in a sinter body are bounded by the pore-solid interface as well as by grain boundaries. The factor of two in equation (26) is present because each grain boundary is incident on two grains, one on each side of the grain boundary. The values of  $S_{VT}$  are plotted against pore volume fraction in Figure 91. The values of total grain surface area per unit mass,  $S_{PT}$ , presented in Table 15, were obtained by dividing the respective values of total grain surface area per cc by the sample densities. The values of total grain surface area per gram are plotted against pore volume fraction in Figure 92.

Values of the mean grain intercept,  $\bar{\lambda}_{gr}$ , are also presented in Table 15. This parameter is given by the relation [26]

$$\bar{\lambda}_{gr} = \frac{4V_V(\text{solid})}{S_{VT}} \quad (27)$$

where  $V_V(\text{solid})$  is the volume fraction of metal in the sinter body. This is equal to one minus the pore volume fraction. The dependence of the mean grain intercept on pore volume fraction is shown in Figure 93 for both 48 micron powders.

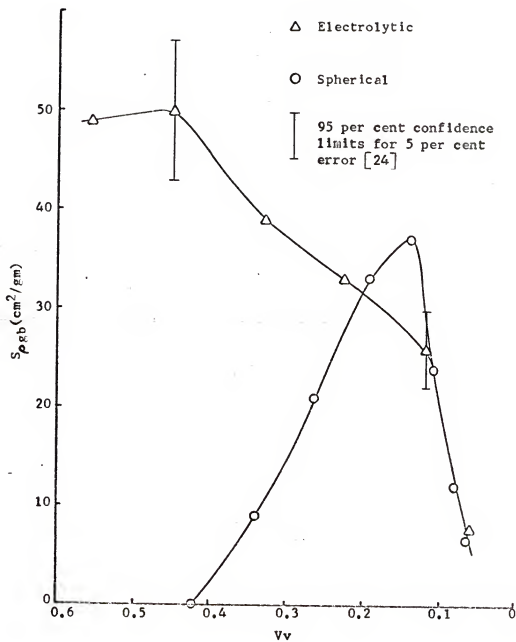


Figure 90. Grain boundary area per unit mass versus volume fraction of porosity for 48 micron spherical and electrolytic copper powders.

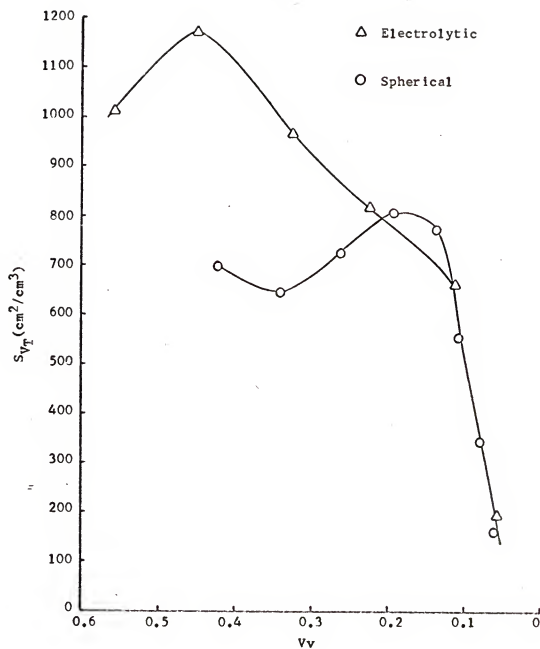


Figure 91. Total grain surface area per unit volume versus volume fraction of porosity for 48 micron spherical and electrolytic copper powders.

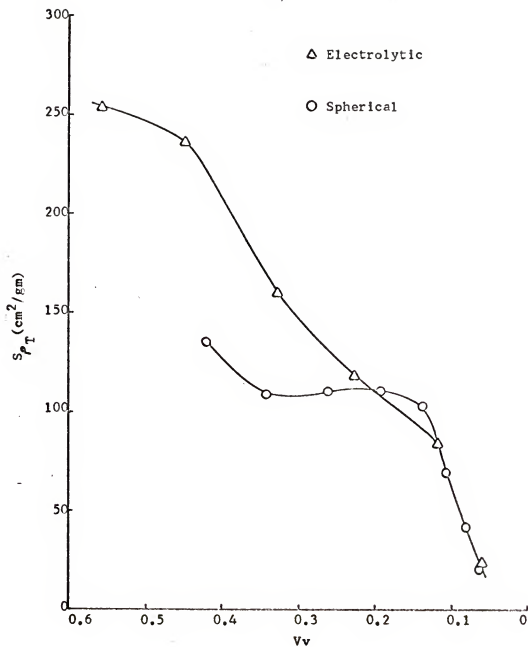


Figure 92. Total grain surface area per unit mass versus volume fraction of porosity for 48 micron spherical and electrolytic copper powders.

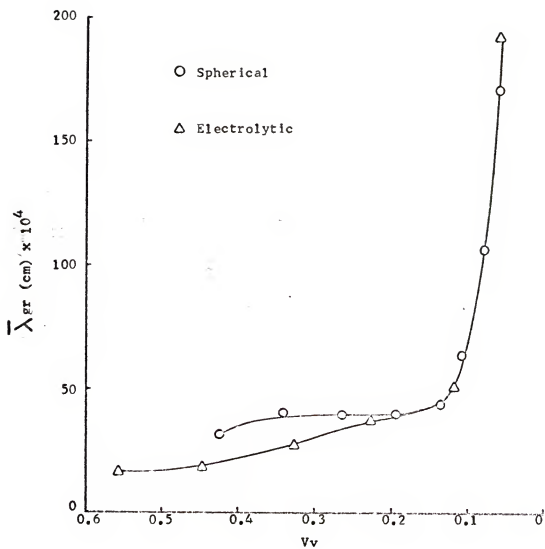


Figure 93. Mean grain intercept versus volume fraction of porosity for 48 micron spherical and electrolytic copper powders.

## CHAPTER VI

### DISCUSSION

#### 6.1 Introduction

The results presented in Chapter V were obtained by the methods of analysis presented in Chapter IV. As pointed out in Section 4.1, these methods evolved during the period of time over which experimental measurements were being made. As each method was used, it was modified until a newer, less cumbersome or more general method was developed. As a result, the data discussed in this chapter were obtained by a number of different techniques, and in some cases by a combination of techniques. Reference is made to the method or methods employed in each case throughout this chapter.

#### 6.2 Variation of the Genus and Number of Separate Parts with Density for Spherical and Electrolytic Copper Powders

##### 6.2.1 Genus of Spherical Powders

6.2.1.1 First stage sintering. During the first stage of the sintering process, before channel closure has started, the number of contacts per particle can be determined by the method of Section 4.2. From these data, for a number of particles, the distribution of the number of contacts per particle can be established. This was done for one sample of the 115 micron spherical powder, as pointed out in Section 5.2,



From the results presented in Table 5, it is apparent that the average number of contacts per particle initially increases with increasing sample density. The 90 per cent confidence limits for 5 per cent error for the data points on which the initial increase is based overlap for both spherical size fractions, as shown in Figures 56 and 61. Since both size fractions exhibit this behavior, the increase is taken as an actual effect and is not attributed to statistical variation in the data.

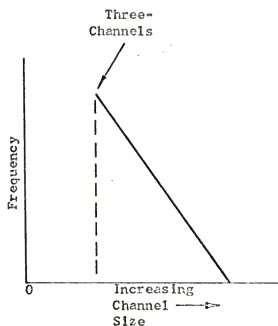
This behavior is expected as a result of shrinkage of the sinter body. In a stack of unsintered particles, there are many pairs of particles which are separated by very small distances relative to the diameter of the particles. As the stack of particles is sintered, and shrinkage occurs, some of these pairs of particles are brought into contact. Each event of this type increases the average number of contacts per particle and also increases the genus of the sinter body by one.

6.2.1.2 Second and third stage sintering. Throughout the first stage of sintering, the contacts between particles increase in size until channel configurations are formed. These channels become smaller as the end of the first stage is reached. Second stage sintering is initiated when these channels begin to close, producing the decrease in genus with increasing density indicated in Figures 56 and 61 for the two size fractions of spherical powder. The decrease in genus with increasing density after the maximum is reached in these two curves is entirely a result of the channel closure process.

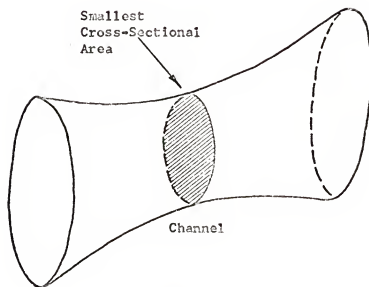
The rate of decrease is large initially, and then decreases with increasing density. This behavior would be expected from a void space having a distribution in channel sizes similar to that shown in Figure 94a where the frequency is largest for small channels. The channels in a sinter body can be classified according to the size of their smallest cross-sectional area, as illustrated in Figure 94b. The smallest channels, referred to as three-channels, are bounded by three particles, each of which is in contact with the other two.

A large number of three-channels are present in an unsintered stack of a single size fraction of spherical particles. These are the smallest channels possible in such a system. When the stack of particles is prepared by pouring the powder into a container, the stacking of the particles is not perfect and some channels are present which are larger than three-channels. Therefore, a distribution of channel sizes exists in such a stack which is qualitatively similar to that shown in Figure 94a. Under these conditions, the variation of the genus with pore volume fraction on sintering would be similar to that shown in Figures 56 and 61 for the following reasons.

The density change associated with the closure of a small channel should be smaller than that associated with the closure of a large channel. Therefore, the small channels would be expected to close earlier in the sintering process than the larger channels. As a result, a sinter structure with a distribution of channel sizes similar to that shown in Figure 94a would be expected to exhibit a rapid decrease in genus with increasing density early in the sintering



(a)



(b)

Figure 94. (a) Schematic size distribution of channels.  
 (b) Channel with smallest cross-sectional area denoted.

process and then a smaller rate of decrease later in the process. The large initial decrease is associated with the closure of the large number of small channels and the smaller rate of decrease, later in the process, is associated with the smaller number of larger channels. This behavior is qualitatively similar to that exhibited by the spherical powders in Figures 56 and 61.

When the channel size distribution becomes narrower, two changes take place in the general features of the genus versus volume fraction of porosity curve. First, the range of density over which channel closure takes place becomes smaller until, for a close-packed stack of particles, all three-channels close at the same density. This is illustrated schematically in Figure 95. Second, the increase in genus during the neck growth stage of sintering is reduced until, for a close-packed stack of particles, there is no initial increase in genus. This is also illustrated schematically in Figure 95. Conversely, when the channel size distribution becomes wider and the particle stacking becomes more irregular, the range of density over which channel closure takes place becomes larger, and the increase in genus during the neck growth stage also becomes larger.

When irregularly shaped particles and size distributions of particles are considered, other channel size distributions are possible. This will be considered during the discussion of the 48 micron electrolytic powder in Section 6.2.3.

The genus of the 7.05 gm/cc ( $V_v = 0.213$ ) sample of the 115 micron spherical powder was determined by two independent methods. The metal space was analyzed by applying the method of Section 4.9

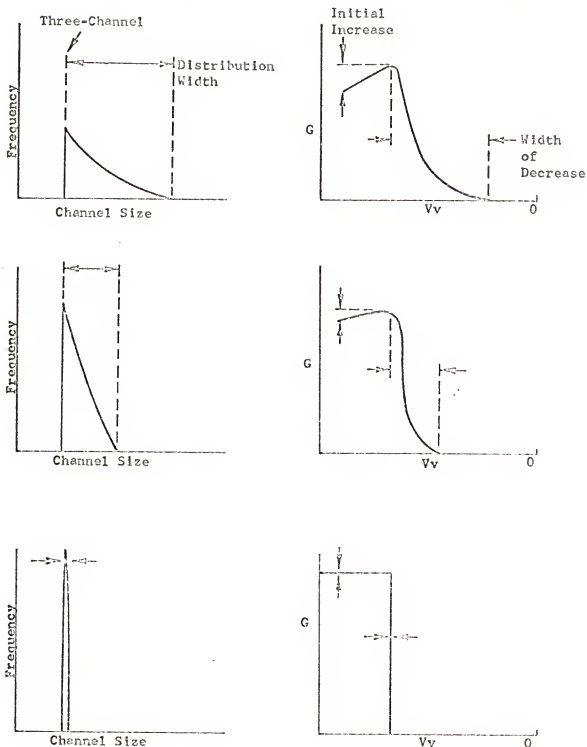


Figure 95. Illustration of the effect of a decrease in the width of the channel size distribution on the variation of the genus with pore volume fraction.

to obtain the value represented by the open circle in Figure 56. The void space was analyzed by the method presented in Section 4.5 to obtain the value represented by the vertical bar in Figure 56. The latter value was obtained by estimating the range of the asymptote for the curve for the 7.05 gm/cc sample in Figure 59. The estimate of the asymptote is probably somewhat high (see Appendix 1); therefore, the value obtained from analysis of the metal space is taken as the actual value. The agreement between the results of the two methods of analysis is good. The values obtained by analyzing the void and metal spaces should be the same since these manifolds have the same connectivity (see Section 2.3).

#### 6.2.2 Variation of the Number of Separate Parts During Sintering for a Single Size Fraction of Spherical Copper Powder

The values of separate parts per gram for the 48 micron spherical powder shown in Figure 106 indicate that as the genus decreases, the number of separate parts increases. Separate parts do not appear until after channel closure begins, as this is the process by which they are produced.

The number of separate parts present at any given time during the sintering process depends on several factors. When a large, irregularly shaped, separate part is isolated, it may remain as a single separate part or it may, as a result of channel closure, break up to form a number of separate parts. A schematic example of this is shown in Figure 96. The separate part, shown at the top of the figure, can break up as a result of channel closure into the three separate parts shown in the bottom right-hand portion of the figure, or it can remain as a single separate part,

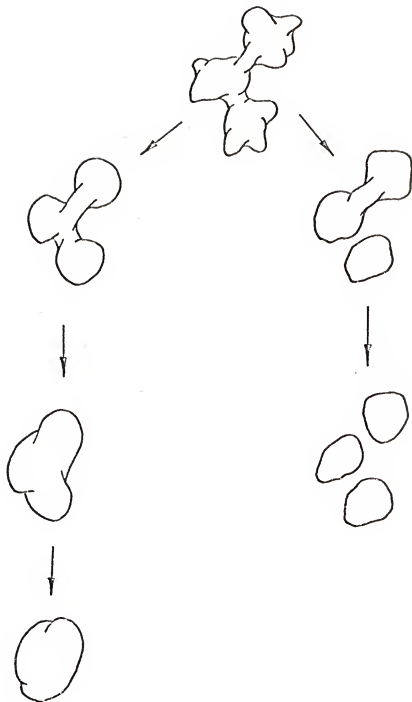


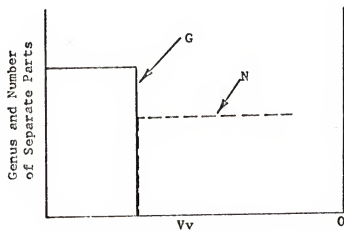
Figure 95. Illustration of possible paths of variation in the shape of an irregularly shaped isolated separate part.

as shown in the bottom left-hand portion of the figure. During the latter process, the channels become larger as a result of surface rounding until the separate part becomes roughly spherical in shape.

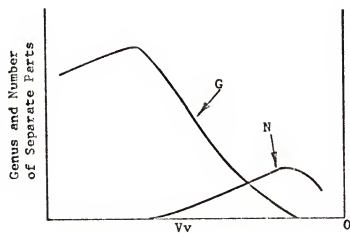
For the ideal case, considered previously, when a close-packed stack of equal size spherical particles is sintered, the plot of the number of separate parts versus volume fraction of porosity, shown in Figure 97a, results. The genus drops to zero, and a number of separate parts appears at the same density. When the stacking of the particles is somewhat irregular, the drop in the genus occurs over a range of density, as indicated in the preceding section, and the increase in the number of separate parts occurs over nearly the same range of density, as indicated in Figure 97b. The number of separate parts must pass through a maximum and decrease to zero at bulk density. No separate parts can be isolated until channel closure starts; therefore, separate parts are only present during second- and third-stage sintering and only simply connected separate parts are present during third-stage sintering. A simply connected separate part is topologically equivalent to a sphere.

A significant feature of the separate parts observed during the course of this work is that only one was multiply connected out of a total of 1187 observed (see Section 4.5.2). The single, multiply connected separate part was topologically equivalent to a torus. From this experimental observation, it is apparent that essentially all separate parts are simply connected. As mentioned in Section 4.5.2, this is substantiated by the computer model results presented in Section 6.7 which indicate that for a network





(a)



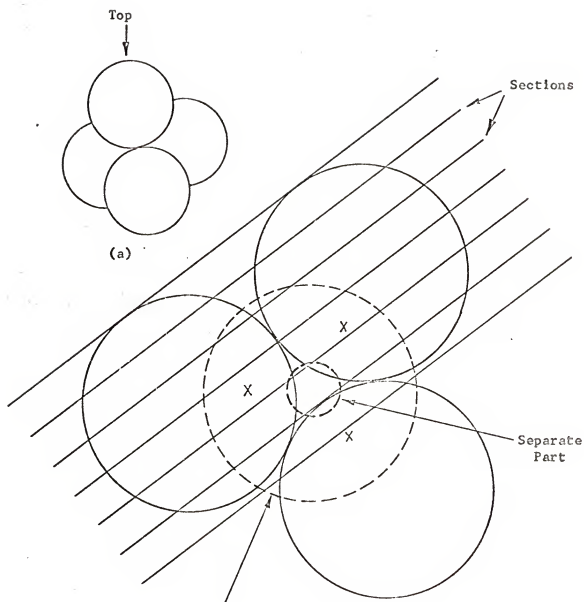
(b)

Figure 97. Hypothetical plots of genus and number of separate parts versus pore volume fraction for (a) perfect stacking and (b) imperfect stacking.

undergoing random branch removal, the probability of isolating multiply connected separate parts is very small.

Consider the small separate parts data obtained during the course of this research. Figure 98a shows three spherical particles, each in contact with the other two, with a fourth particle placed on top, all of which are equal size spheres. When all channels incident on such a hole, referred to as a tetrahedral hole, close, a separate part, such as that indicated in Figure 98b, is formed. The size shown in Figure 98b should be approximately correct for such a separate part, relative to the diameter of the spherical particles. When six to seven sections in a distance equal to the diameter of the spherical particles are passed through the four particles, as shown in Figure 98b, the diameter of the separate part is greater than the distance between two serial sections. Recall that six to seven sections in a distance equal to the diameter of the particles were used in the analysis of the 48 micron spherical powder; thus, separate parts formed from tetrahedral holes can be classified as small or large depending on whether they are intersected by one or two serial sections. The size of the separate part must be smaller than that shown in Figure 98b before it becomes possible for it to remain unobserved during the analysis.

Consider the curves of Figures 67 and 99. The ratio of the number of small to the number of large separate parts decreases with increasing density, as shown in Figure 100. This behavior is also indicated by the computer model results presented in Section 6.7. This effect can be attributed in part to the fact that it is necessary to close a larger number of channels in order to isolate



X = Points of Contact Between Particles

(b) Top View

Figure 98. Illustration of the size of a small separate part relative to the spacing between serial sections.

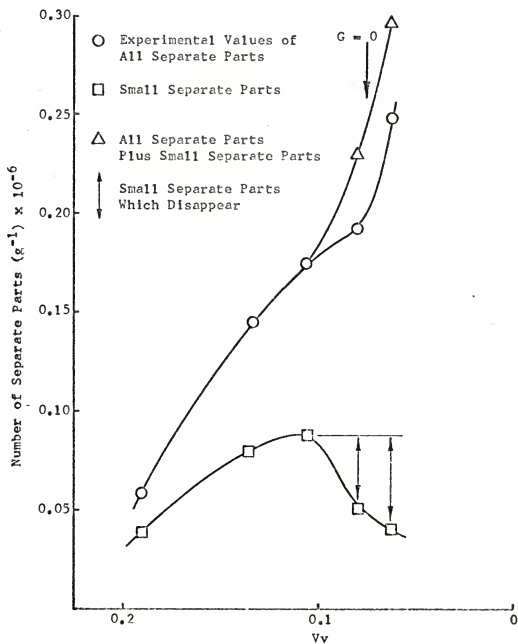


Figure 99. Number of separate parts (all and small) versus volume fraction of porosity for 48 micron spherical copper powder.

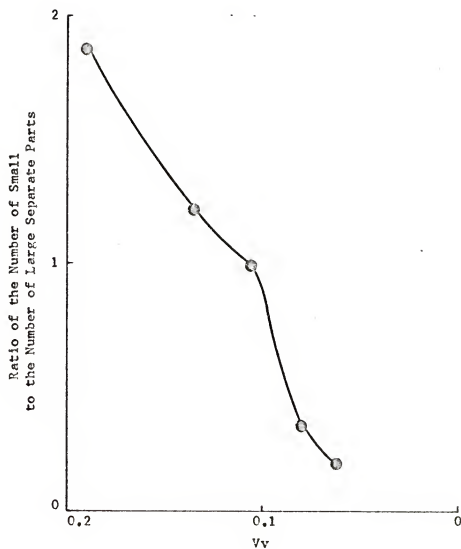


Figure 100. Ratio of the number of small to the number of large separate parts versus volume fraction of porosity for 48 micron spherical copper powder.

a large separate part (two or more nodes) than to isolate a small separate part (one node). As a result, it is expected that when only a small number of channels have closed, it would be most probable for small separate parts to be isolated, and as more channels close, it should become increasingly probable for large separate parts to be isolated.

It is likely, however, that the decrease in the ratio of the number of small to the number of large separate parts with increasing density is produced for the most part by the disappearance of small separate parts, especially during the end of second stage and throughout third-stage sintering.

Consider the variation of the number of small separate parts per gram with increasing density, shown in Figure 99. The number of small separate parts per gram first increases, reaches a maximum value and then decreases with increasing density. This variation provides further verification (see Section 3.5) that these small separate parts are not produced by pitting during polishing of the sample surface. This is because such a pitting effect would not be expected to have such a large difference from sample to sample since the three highest density samples were polished together.

The disappearance of the small separate parts could be the result of their growing smaller until they are no longer observed and/or their growing larger until they are no longer counted as small, but as large separate parts. The evidence which presently exists indicates that the small separate parts grow smaller and disappear rather than grow larger. Experimental work by Rhines, et al. [30] on the sintering of copper and a theoretical treatment

by Van Bueren and Hornstra [31] support the disappearance of small separate parts.

Since the small separate parts disappear, the number which have disappeared for a given pore volume fraction, indicated by arrows in Figure 99, must be added to the experimentally observed total number in order to obtain an estimate of the actual total number of separate parts isolated. This was done to obtain the values indicated by triangles in Figure 99. This figure indicates that the rate of increase in the experimentally observed total number of separate parts with decreasing pore volume fraction exhibits a rapid increase at a pore volume fraction of about 0.075. This can be explained as follows.

In the density range where the genus approaches zero ( $V_V = 0.075$ ), portions of the void space form tree-like configurations, such as that illustrated in Figure 101a, as a result of the random closure of channels [3]. As each channel in a tree closes, such as the one indicated by the arrow in Figure 101a, the number of separate parts is increased by one as two separate parts are then present.

When a channel closes in a portion of the structure which has a non-zero value of genus, the number of separate parts may remain unchanged. This is the case when the channel indicated by the arrow in Figure 101b closes. Therefore, the greatest increase in the number of separate parts per channel closure event will occur in the density range where the genus reaches zero. Since the rate of decrease in genus, or rate of channel closure, with increasing density is large, even in the density range where the genus reaches zero (see Figures 56 and 61), the rate of increase in the number

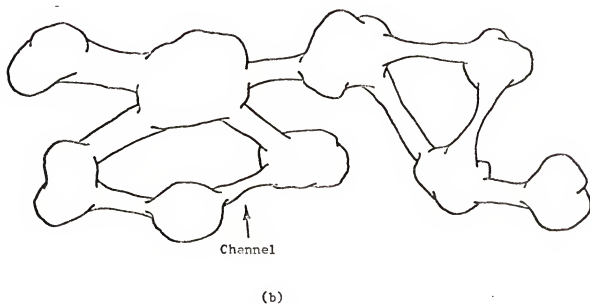
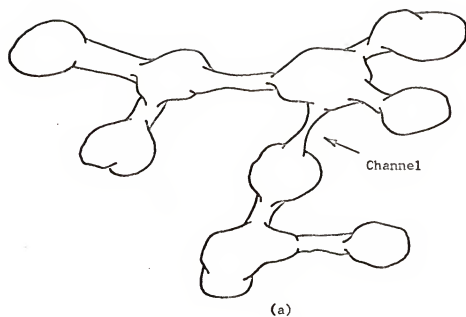


Figure 101. Schematic separate parts illustrating the effect of channel closure on the number of separate parts.



of separate parts with increasing density is largest in this density range.

The number of separate parts per gram is zero at bulk density; therefore, the number of separate parts per gram must pass through a maximum and then decrease with increasing density. This decrease was observed for the 48 micron electrolytic powder, as shown in Figure 82. The geometric process by which the number of separate parts decreases is the disappearance of small separate parts.

#### 6.2.3 Variation of the Genus During Sintering for 48 Micron Electrolytic Copper Powder

Consider the plot of genus per gram versus volume fraction of porosity for the 48 micron electrolytic powder shown in Figure 73. The particles of this powder are very irregular in shape, as shown in the photomicrograph in Figure 6. As a result, the unsintered powder has a very low density ( $V_V = 0.9$ ), about 10 per cent of the theoretical density of copper.

The lowest density sample analyzed,  $V_V = 0.85$ , has the largest value of genus per gram. The genus rapidly decreases from this value with increasing density until a pore volume fraction of about 0.55 is reached. It then increases until a pore volume fraction of about 0.45 is reached, after which it decreases to zero at about 0.10 pore volume fraction.

The large initial value of genus per gram is the result of the irregular shape of the electrolytic powder particles. The region of contact between two adjacent particles of this powder probably consists of a number of contacts, as illustrated in Figure 102.

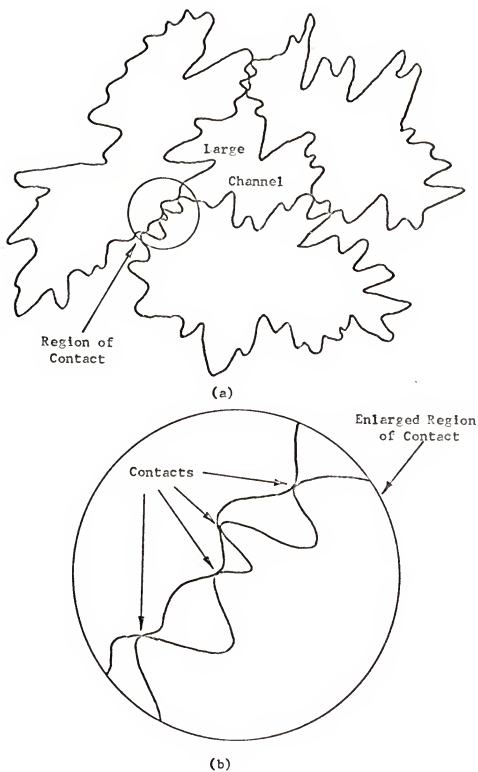


Figure 102. (a) Cross section through three irregular powder particles.  
(b) Enlarged region of contact between two irregular powder particles.

It should be noted that the unsintered electrolytic powder may have either a larger or smaller value of genus per gram than that of the lowest density sample analyzed. At the onset of sintering, the genus of this powder could decrease as it does for the lowest density samples of Figure 73; however, contacts between particles could form as a result of shrinkage, as they did for the single size fractions of spherical powder. This could produce an initial increase in the genus with increasing density. Which phenomenon occurs is not resolved by the presently available data.

The rapid initial decrease in genus with increasing density is the result of the closure of small channels and/or pulling apart of contacts between particles. Schematic examples of these events are illustrated in Figure 103 and 104. The region of contact between two irregularly shaped particles is shown in Figures 103a and 104a. These figures are the same, and, in each, three points of contact between the particles are indicated. On exposure to the sintering conditions, the configuration shown in Figures 103b and 104b results, indicating that the points of contact have grown into areas of contact. In Figure 103b, two channels between the particles are indicated. In Figure 104b, the two filamentary regions adjacent to the channels are indicated.

In Figure 103c, the channels have grown smaller, and, in Figure 103d, they have closed. As a result, the genus of the structure is decreased by two.

In Figure 104c, one of the filamentary regions has pulled apart, and, in Figure 104d, both filamentary regions have pulled apart. As a result, the genus of the structure is decreased by two.

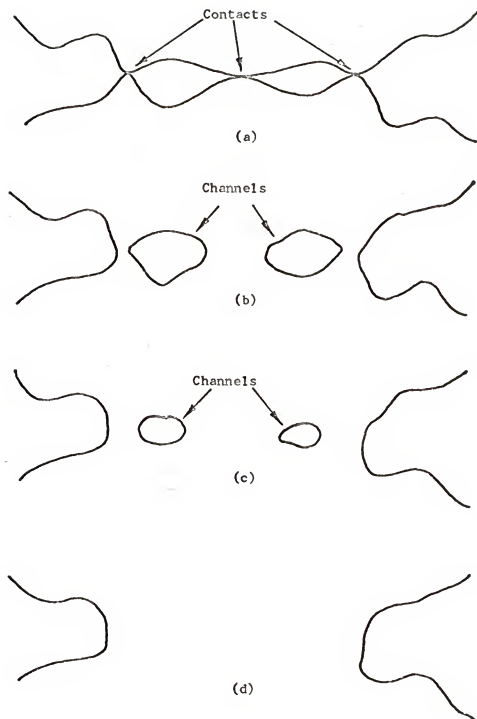


Figure 103. Illustration of the closure of small channels between irregularly shaped particles.

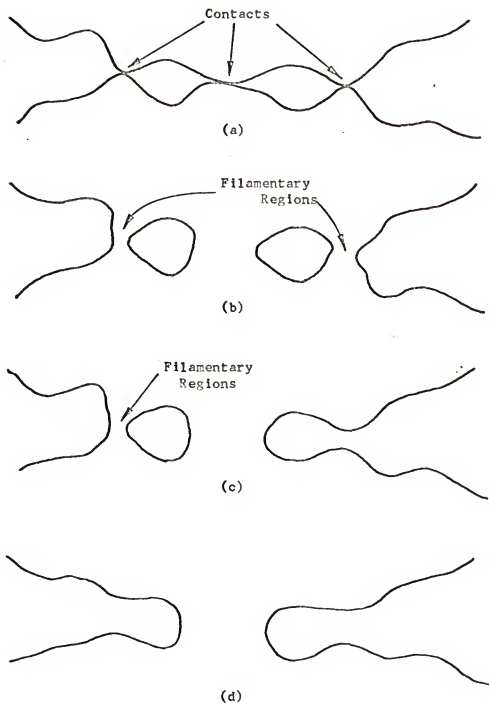


Figure 104. Illustration of the pulling apart of filaments between irregularly shaped particles.

Both the closure of small channels and pulling apart of filaments have the same effect on the genus. This is apparent from the fact that the configurations shown in Figures 103d and 104d are topologically equivalent. Both events can reduce the surface area of the sample and, hence, are energetically feasible.

Since these phenomena cannot be distinguished from consideration of the genus or changes in the genus with density, the data presented in Figure 73 are not sufficient to determine which, if either, process is dominant.

An attempt was made to determine what geometric process is taking place by reconstructing a small volume of the electrolytic powder sintered to a density of 2.81 gm/cc as follows. A small area of each of 15 serial sections through the structure was enlarged and reproduced on Xerox transparencies. The transparencies were then stacked, one above the other, to produce the three-dimensional model, a photograph of which is shown in Figure 105. The dimensions of the portion of the sinter structure shown are 220 microns by 220 microns by 22.8 microns high. Several small channels and filamentary regions are present in this portion of the sinter body. As a result, it cannot be said that either channel closure or the collapse of filaments predominates at this point during sintering of the electrolytic powder.

When the electrolytic powder is about 45 per cent dense ( $V_v = 0.55$ ), the initial rapid decrease in genus is complete. With further sintering, the variation in genus with increasing density is qualitatively similar to that for the spherical copper powders; the genus first increases with increasing density, reaches a maximum,



Figure 105. Photograph of a stack of 15 serial sections through 48 micron electrolytic copper powder sintered to a density of 2.81 gm/cc.

and then decreases to zero. It is apparent from this similarity of the change in genus with density for the electrolytic and the spherical powders that the increase in genus in the range of density from  $V_v = 0.55$  to  $V_v = 0.45$  is a result of the formation of new contacts, or branches, caused by shrinkage of the sinter body. As pointed out previously (see Section 6.2.1), this phenomenon takes place in a single-size fraction of spherical powder during the first stage of sintering. The range of density over which this occurs is quite different for equal size fractions of spherical and electrolytic powders, as can be seen from the curves of Figure 106.

The formation of new contacts in the electrolytic powder probably takes place from the onset of sintering. The resulting rate of increase in genus with increasing density is small relative to the initial rate of decrease in genus produced by closure of small channels and removal of filaments. This is illustrated by the hypothetical curves shown in Figure 107. Curve A represents the genus resulting from small contacts between particles, and curve B represents genus produced by the formation of new contacts. The sum of these two curves is the observed genus given by the solid curve.

After the small channels and filaments have been removed (curve A = C), contacts are still forming. Therefore, the genus begins to increase. This continues until large channels (see Figure 102) begin to close. This produces the final decrease of the genus to zero.

If the initial decrease in genus was spread over a greater range of density, then the increase in genus produced by the



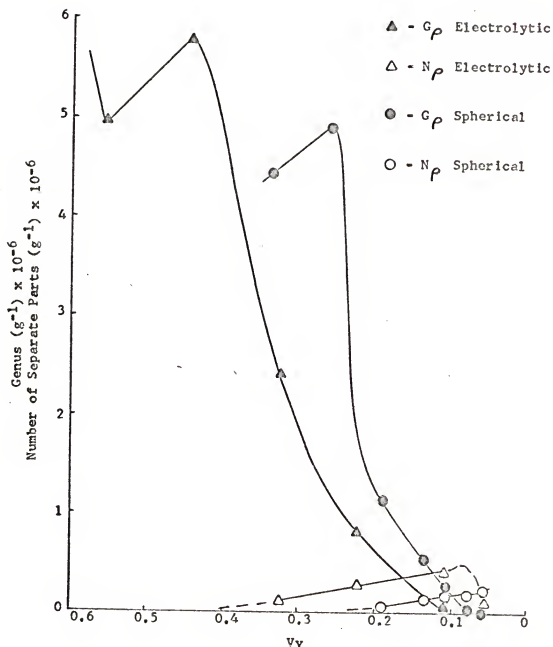


Figure 106. Genus per gram and number of separate parts per gram versus volume fraction of porosity for 48 micron spherical and electrolytic copper powders.

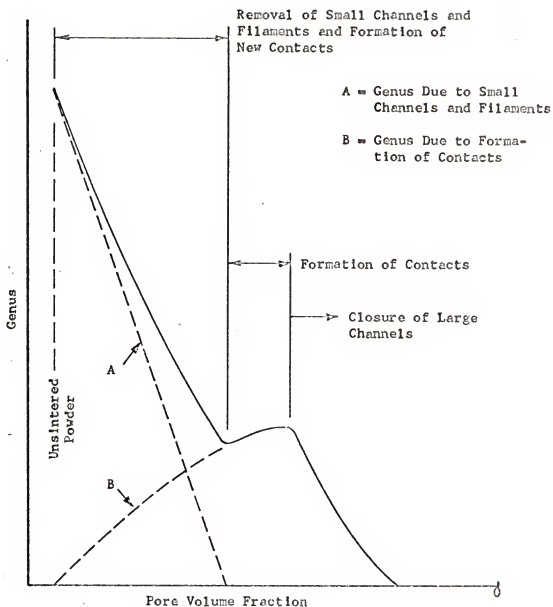


Figure 107. Illustration of the various factors which contribute to the genus of the 48 micron electrolytic copper powder.

formation of contacts might not be observed. The variation of the genus during sintering depends on the distribution of channel sizes in the powder, as was shown for the single size fraction of spherical powder in Section 2.3. In order to obtain a plot such as the one shown in Figure 73, a channel size frequency distribution such as that shown in Figure 108 must exist in the loose electrolytic powder.

The large number of small channels close early in the sintering process and account for the large initial rate of decrease in the genus with increasing density. Small filaments, which pull apart early in the sintering process, have the same effect on the genus as the closure of small channels; thus, the number of small channels must include the number of filaments which pull apart.

In order for the genus to then increase with increasing density, there must be a range of channel sizes with a low frequency of occurrence, as illustrated in Figure 108a. As a result, there is a range of density for which few channels are closing, yet shrinkage is still taking place. This causes contacts to be formed, thus increasing the genus of the structure, as pointed out previously. Still later in the sintering process, large channels begin to close producing the final decrease in the genus to a value of zero. A powder having a channel size frequency distribution, such as that shown in Figure 108b, would probably not exhibit such an increase in genus.

The large initial value of genus for the electrolytic powder indicates that the number of contacts per particle may be considerably greater than that for the spherical powder. In order to determine

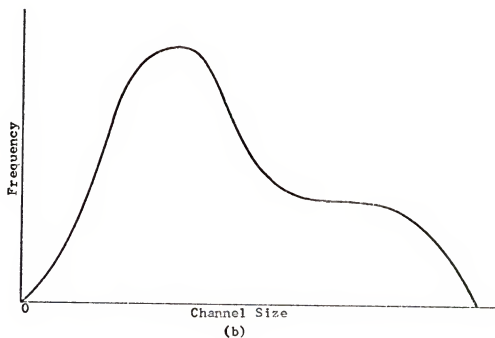
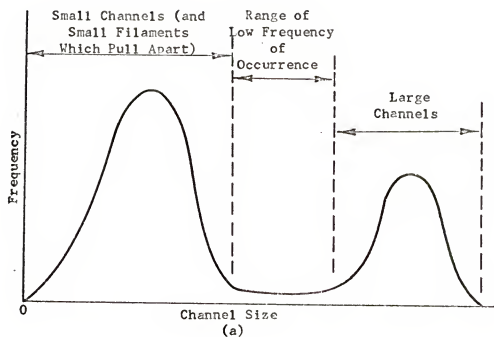


Figure 108. Two schematic channel size distributions.

the average number of contacts per particle,  $\overline{b/n}$ , the number of particles per gram must be determined. Equation (7) can then be solved for  $C_p/P_p$ , which is equal to  $\overline{b/n}$ .

The average mass of the electrolytic powder particles was determined by the method described in Section 3.3. One hundred particles were measured. The average value of the cube of the particle diameter was determined so that the average volume of an electrolytic powder particle could be calculated. From this, the number of particles per gram of powder was found to be  $5.71 \times 10^6$  (there are  $1.93 \times 10^6$  particles per gram of 48 micron spherical copper powder). With this value for the electrolytic powder and the value of genus per gram for the lowest density sample analyzed, equation (7) was solved to obtain an estimate of the average number of contacts per particle. The lowest density sample of the electrolytic powder was found to have 14 to 15 contacts per particle.

The number of contacts per particle for the electrolytic powder at a pore volume fraction of 0.555 was also obtained in this way. For this pore volume fraction, there are approximately four contacts per particle. Thus, during the initial decrease in genus with increasing density, about 10 or 11 contacts are removed per particle. This implies that each contact present at a pore volume fraction of 0.555 consisted of three to four contacts at a pore volume fraction of 0.855.

The contacts which remain between the electrolytic particles at a pore volume fraction of about 0.55 can be considered as large, or coarse, relative to the small channels and filaments just mentioned. It is this relatively coarse structure which controls

the evolution of the geometric structure of the sinter body with further sintering. The remainder of the change in genus with density is similar to that for a single size fraction of spherical powder, as discussed in Section 6.2.1; however, the large channels in the electrolytic powder begin to close at a lower density than in the spherical powder. This may be due, in part, to a difference in the channel size distributions for these powders. Consider the schematic curves shown in Figure 109. The spherical powder has a lower limit in channel size, as mentioned previously and indicated in the top curve. The electrolytic powder has channels of all sizes between zero and some maximum, as shown in the lower curve. If some large channels in the electrolytic material are smaller than the lower limit of channel size for the spherical powder, as indicated by the arrow above the lower curve of Figure 109, these channels would be expected to close at a lower density than larger channels. Thus, the final decrease in genus for the electrolytic powder would be expected to start at a lower density than the decrease in genus for the spherical powder.

The variation of the properties of the electrolytic and spherical powders will be considered further in Section 6.5.

#### 6.2.4 General Features of the Variation in the Number of Separate Parts for the 48 Micron Electrolytic Copper Powder

The qualitative features of the variation of the number of separate parts for the 48 micron electrolytic powder with pore volume fraction are similar to those for a single size fraction of spherical powder. The plots of Figure 106 show that separate parts

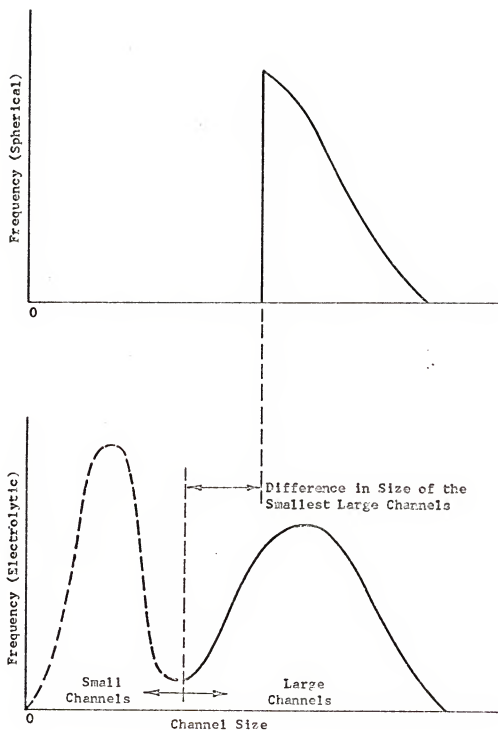


Figure 109. Comparison of some features of the channel size distributions of the spherical and electrolytic powders.

do not appear until after closure of large channels begins, and, that as the genus decreases, the number of separate parts increases. As pointed out previously, the number of separate parts must pass through a maximum and then decrease with increasing density. The data for the electrolytic powder verify this, as can be seen from the curves of Figures 82 and 106. The highest density sample (8.45 gm/cc,  $V_V = 0.57$ ) has a density greater than that at which the maximum number of separate parts is present.

It cannot be determined from the data for the electrolytic powder if an increase in the rate of production of separate parts with increasing density occurs after the genus reaches zero. Recall that this was observed in the spherical powder (see Figures 67 and 82), and it probably occurs in the electrolytic powder also.

Only one value of the number of small separate parts per gram was obtained for the electrolytic powder; hence, their variation with density was not determined. This value was used as a rough check on the proportion of small separate parts. It was unnecessary to determine the variation in the number of small separate parts with pore volume fraction, as was done for the 48 micron spherical powder, because the absence of a significant polishing error was established by the data for the spherical powder (see Section 6.2.2).

Small separate parts were counted for the 7.92 gm/cc ( $V_V = 0.116$ ) sample of the electrolytic powder, and about 70 per cent of the total number of separate parts were classified as small. The largest separate parts counted as small are smaller for the electrolytic than for the spherical powder because the serial sections are closer together for the electrolytic than for the spherical powder. If the



same spacing had been used for the electrolytic as for the spherical powder, more than 70 per cent of the separate parts found in the electrolytic powder would have been classified as small. At the same point in the evolution of the topological properties, that is, just before the genus reaches zero, 70 per cent of the separate parts in the spherical powder are classified as small; therefore, the fraction of small separate parts is probably greater for the electrolytic than for the spherical powder. It cannot be determined, however, from the experimental data whether or not the difference is significant. It can only be stated that the fraction of small separate parts is large (0.7 or greater) for both powders.

### 6.3 General Features of the Cumulative Genus Versus Volume of Material Analyzed Curves

The cumulative genus versus volume of material analyzed curves generally exhibit an approach to linearity and then linearity with increasing volume of material analyzed. The way in which linearity is approached and the slope of the linear portion depends on the features of the deformation retract of the space from which the curve was obtained. Although the most important property of these curves is the slope of the linear portion, the manner in which the linear portion is approached yields some information about the structure under consideration. Another factor which is important is the size of the area on each serial section which is analyzed. This is considered in Section 6.13.1.

#### 6.3.1 $G_1^{\min}$ Curves

First, consider the  $G_1^{\min}$  versus volume analyzed plots shown in Figures 57, 58, 62 to 66 and 74 to 81. These curves all reach

linearity after some thickness of material has been analyzed. Since the area analyzed is the same on each section, the volume analyzed is directly proportional to the thickness analyzed. The thickness at which linearity is reached depends on the features of the network being analyzed in the following way.

Recall that internal circuits, that is, circuits inside the volume of material analyzed, must be observed in order to change  $G_1^{\min}$ . These circuits have some average size\* and a distribution of sizes for any given network. The circuit size in a sinter structure may be somewhat ambiguous since the position of the deformation retract cannot be uniquely determined. Another factor is that some circuits may be very irregular in shape in the third dimension, and therefore they may be difficult to characterize. However, the development presented here depends only upon the qualitative aspects of a circuit size, and therefore the results of this development are not affected as long as the qualitative concept of circuit size is established.

For a sinter structure, the minimum size of the circuits is finite; thus, a finite volume of material must be analyzed before they are observed. It is for this reason that the initial slope of all  $G_1^{\min}$  curves is zero. As the volume analyzed is increased, larger circuits are observed along with the smaller ones, and the

---

\*A circuit can be characterized according to its size by its average diameter. This is the average distance between pairs of parallel tangents to the circuit, as illustrated in Figure 110a for a torus. For the present purpose, the smallest circuit must be used rather than the actual deformation retract, as illustrated in Figures 110b for a torus and 110c for an irregularly shaped circuit. This is because it is this smallest circuit which is experimentally observed.

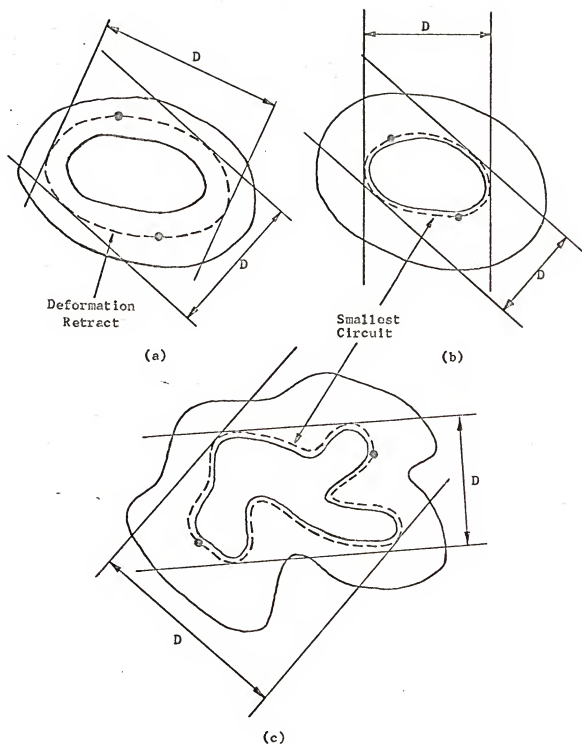


Figure 110. Illustration of a measure of circuit size.

slope of the curve increases. The linear portion of the curve is reached when a thickness has been analyzed such that the largest circuits in the network are observed. The final slope of the linear portion of the curve depends on the volume density of the circuits in the network (and the size of the area analyzed on each serial section, as discussed in Section 6.13.1).

The volume or thickness which has been analyzed when the  $G_1^{\min}$  curve first reaches linearity also depends on the size distribution of the circuits in the network. For both the 48 micron electrolytic and spherical powders, the thickness analyzed to reach linearity first increases and then decreases with increasing sample density, as shown in Figure 111. This is the result of an increase and then a decrease in the size of the largest circuits with increasing density. This can be explained as follows.

At low density, the circuits are small and their distribution in size is narrow. A schematic network and distribution of circuit sizes is shown in Figure 112a. As channel closure starts and branches are removed, the size of the largest circuits increases, as illustrated in Figure 112b. As channel closure continues, a configuration is reached in the network where, for a given channel closure event, it becomes more probable that large circuits will be removed from the network. This situation arises when the number of channels associated with large circuits becomes greater than the number of channels associated with small circuits. As channel closure continues under these conditions, the size of the largest circuits becomes smaller, as illustrated in Figure 112d. Thus, the size of the largest circuits first increases and then decreases with increasing density.

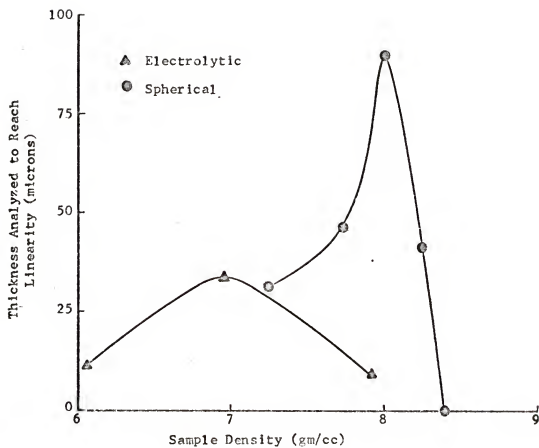
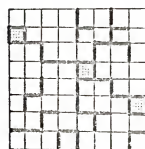
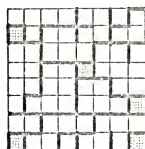
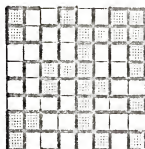
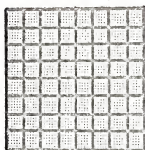
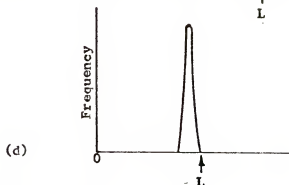
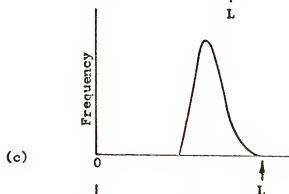
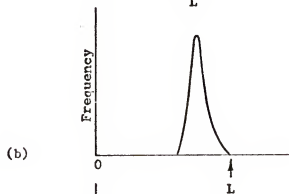
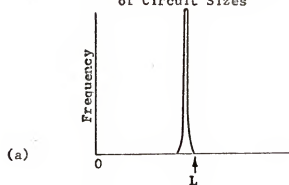


Figure 111. Thickness analyzed to reach linearity versus sample density for 48 micron electrolytic and spherical copper powders.

Schematic Node -  
Branch NetworkFrequency Distribution  
of Circuit Sizes

L = Largest Circuit Size

Figure 112. Frequency distribution of circuit size for four schematic node-branch networks.

As a result of this variation in the size of the largest circuits, it is apparent that the thickness of material which must be analyzed to reach linearity should depend on the genus of the structure. When these thicknesses are plotted against genus, the features of the curves are the same for both the 48 micron electrolytic and spherical powders, as shown in Figure 113. The maximum occurs at approximately the same value of genus for both powders.

### 6.3.2 $G_i^{\max}$ Curves

Consider the  $G_i^{\max}$  versus volume analyzed curves shown in Figures 57, 58, 62 to 66 and 74 to 81. These curves generally reach linearity after less volume has been analyzed than in the case of the  $G_i^{\min}$  versus volume analyzed plots; in fact, most of the  $G_i^{\max}$  plots are linear from the start of the analysis.

In general, any initial non-linearity of the  $G_i^{\max}$  versus volume analyzed curves can be explained as follows. A number of tree-like regions and separate parts of the void space will intersect the first two serial sections analyzed, and hence form loops with the external node. A tree-like region and a tree-like separate part are shown schematically in Figures 114 and 101a, respectively. As successive serial sections are considered, these tree-like regions and separate parts end and the loops they form with the external node are removed. Therefore, after some thickness has been analyzed, the effect of these tree-like regions and separate parts through the top of the sample is no longer felt, and a slope of the  $G_i^{\max}$  plot, dependent upon the circuit size distribution of the material under consideration, is then established. This thickness depends on the size and number of the separate parts and

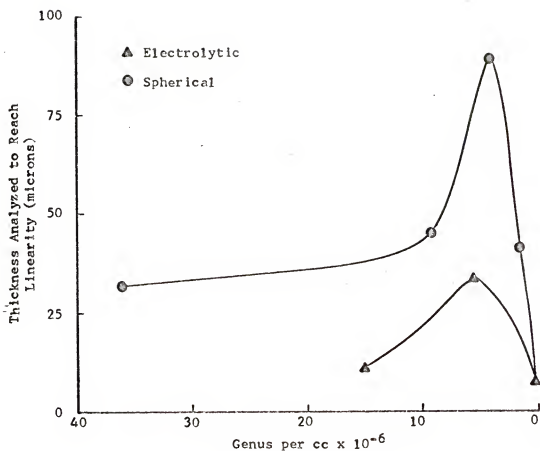


Figure 113. Thickness analyzed to reach linearity versus genus per cc for 48 micron spherical and electrolytic copper powders.



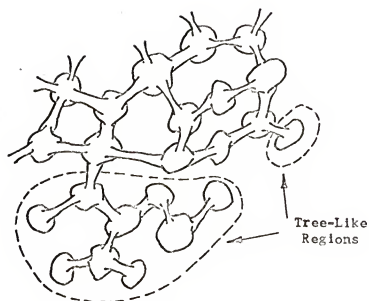


Figure 114. Illustration of tree-like regions attached to multiply connected regions of the void space.

tree-like regions present and on the value of genus per gram for the structure.

As the genus decreases (i.e., as channel closure takes place), increasing numbers of tree-like regions and separate parts are produced. Recall that when separate parts are first isolated, they are predominantly small. As channel closure continues, it becomes more probable for larger separate parts and tree-like regions to be isolated. As a result, a greater thickness must be analyzed before their effect on the  $G_i^{\max}$  versus volume analyzed curves is removed as the sample density increases.

As mentioned previously (see Section 6.1), a number of different methods were employed to obtain the data presented in Chapter V. As a result, a number of different  $G_i^{\max}$  and  $G_i^{\min}$  versus volume analyzed curves were obtained. The features of these curves will now be considered individually.

The curve for  $G_i^{\max}$  lies below the  $G_i^{\min}$  curve in Figure 81 because only changes in  $G_i^{\max}$  and  $G_i^{\min}$  were plotted and not the actual values of these parameters. Also, as a result of this, most of the cumulative genus curves for the electrolytic powder start at zero genus. For the three which do not, one for the 4.96 and two for the 6.05 gm/cc sample, the number of circuits on the first section was taken as the starting point for both the  $G_i^{\max}$  and  $G_i^{\min}$  curves. The initial value for  $G_i^{\max}$  is greater than that for  $G_i^{\min}$  for these samples as a result of connections to the external node across the sides of the sample.

The  $G_i^{\max}$  curves for the 48 micron spherical powder also start at some positive value because all branches through the top and

bottom of these samples were assumed to be connected to an external node.

The initial non-linearity of the  $G_i^{\max}$  plots for the 6.95 and 7.92 gm/cc samples of the electrolytic powder and the 8.00, 8.25 and 8.40 gm/cc samples of the 48 micron spherical powder is a result of the presence of separate parts and/or tree-like regions of the void space.

The  $G_i^{\max}$  plot for the 8.00 gm/cc sample of the 48 micron spherical powder has a positive slope throughout; however, linearity is not reached until about the same point in the analysis at which linearity is reached in the  $G_i^{\min}$  curve. The positive slope is a result of the relatively large value of genus for this material; an initial negative slope occurs in structures with lower values of genus per unit volume, as pointed out below. The slow approach to linearity is a result of the presence of large circuits in the network, just as in the case of the  $G_i^{\min}$  curve.

The presence of tree-like regions and separate parts can produce an initial decrease in the  $G_i^{\max}$  versus volume analyzed curve. The decrease produced by this effect is apparently small compared to the increase in  $G_i^{\max}$  for the 8.00 gm/cc material; however, part of the slow approach to linearity could be attributed to this effect.

The  $G_i^{\max}$  plot for the 8.25 gm/cc sample of the 48 micron spherical powder has an initial negative slope and reaches linearity more rapidly than the 8.00 gm/cc material. The more rapid approach to linearity indicates that the largest circuits are smaller in the 8.25 gm/cc than in the 8.00 gm/cc material (see the preceding

section). The initial decrease is the result of the low value of genus and the presence of tree-like regions and separate parts. This is also the case for the 7.92 gm/cc sample of the electrolytic powder.

The  $G_1^{\max}$  plot for the 8.40 gm/cc sample of the 48 micron spherical powder also has a negative initial slope. The value of genus for this sample is zero, and the initial decrease in  $G_1^{\max}$  is a result of the presence of separate parts which intersect the top of the sample.

#### 6.4 General Features of the Cumulative Number of Separate Parts Versus Volume of Material Analyzed Curves

Some of the cumulative large and total separate parts versus volume analyzed curves exhibit an approach to linearity (as opposed to linearity from zero volume analyzed). The total separate parts curves for the 7.74 gm/cc sample of the 48 micron spherical powder, the 8.05 gm/cc sample of the 115 micron spherical powder and the 7.92 gm/cc sample of the 48 micron electrolytic powder all exhibit this behavior, as shown in Figures 69, 60 and 85, respectively. This approach to linearity is a result of the fact that a number of sections must be analyzed before large separate parts can be detected. As a result, the large separate parts curves do not start until four to seven sections have been analyzed.

It is necessary to consider at least four sections before a large separate part can be detected. If the number of large separate parts per gram is small, as in the case of the 7.26 gm/cc ( $V_V = 0.190$ ) sample of the 48 micron spherical powder shown in Figure 67, then it may be necessary to consider more than four sections before any large separate parts are found. For this sample,

the large separate part curve increases only every two to three sections; thus, the minimum of four sections plus two to three sections per increase in the curve gives six to seven sections before a large separate part may appear. Seven sections were analyzed before a large separate part was observed in the 7.26 gm/cc sample of the 48 micron spherical powder (Figure 68), and five sections were required for the 7.74 gm/cc sample (Figure 69).

It is only necessary to consider three sections in order to detect small separate parts. Since the number of small separate parts is generally a large fraction of the total number of separate parts, the total separate part curves are approximately linear from zero volume analyzed, with the exception of those mentioned above.

The plots of cumulative number of large separate parts versus volume analyzed for the 8.00, 8.25 and 8.40 gm/cc samples of the 48 micron spherical powder shown in Figures 70, 71 and 72, respectively, exhibit a change in slope at about  $70 \times 10^{-6} \text{cc}$  analyzed. This occurs only for the large separate parts curves and not for the total separate parts curves. This change in slope takes place at the same point in the analysis at which a new camera adaptor was obtained. The use of this new equipment produced a considerable improvement in resolution as the result of increased sharpness of focus. Recall that large separate parts appear on two or more sections. Because of the increased resolution, more separate parts were classified as large and fewer as small separate parts. This has no effect on the total number of separate parts observed. The three samples showing this effect were mounted together and sectioned at the same time; consequently, the change in slope occurs at the same value of volume analyzed for all three samples.

6.5 Comparison of the Genus Versus Volume Fraction of Porosity Curves for the 115 Micron Spherical, 48 Micron Spherical and 48 Micron Electrolytic Copper Powders

Consider Figure 115 in which genus per gram and number of separate parts per gram are plotted versus pore volume fraction for the 48 micron and 115 micron spherical powders. The values for the 115 micron powder are multiplied by a scale factor, 13.74. This value is obtained as shown in Appendix 3. The points in Figure 115 lie on the same curves over the entire density range; thus, the path of evolution of genus for these two size fractions of spherical copper powder is the same for the entire sintering process. This experimental observation and the development in Appendix 3 indicate that the genus of single size fractions of spherical powder are related throughout the sintering process by a scale factor which is established by the dimensions of the powders. This behavior indicates that the initial geometry of the stack of powder controls the evolution of the topological properties throughout the sintering process.

Only one value of separate parts per gram was obtained for the 115 micron powder. Thus, it cannot be concluded that the evolution of the number of separate parts per gram is the same for the two powders. However, the one value for the 115 micron powder, multiplied by 13.74, does agree well with the 48 micron powder data, as can be seen in Figures 67 and 115.

Consider the genus per gram versus volume fraction of porosity plot for the 48 micron electrolytic powder in Figure 106. After the initial decrease is complete, the variation in genus is similar to that

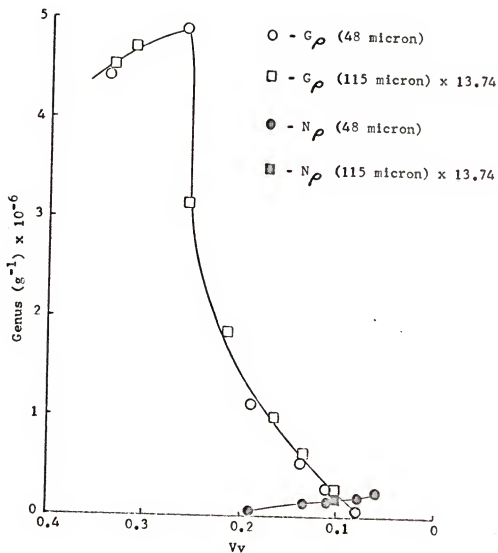


Figure 115. Comparison of genus per gram versus volume fraction porosity for 48 and 115 micron spherical copper powders.

which takes place for the spherical powders. That is, the genus then increases to a maximum and then decreases to zero with increasing density. That part of the variation of the genus of the 48 micron electrolytic powder which is similar to that of the spherical powders is shown in Figure 106, along with the variation in the genus of the 48 micron spherical powder.

Both powders exhibit an increase in genus as a result of the formation of contacts on shrinkage and then a decrease in genus to a value of zero produced by channel closure. These changes take place at lower density in the electrolytic than in the spherical powder. The reasons for this are as follows.

At a pore volume fraction of 0.55, the small scale features in the electrolytic powder have been removed by surface rounding, closure of small channels and/or pulling apart of filaments. The structure of the electrolytic powder at this point can be roughly visualized as that of a stack of a single size fraction of spherical powder particles, approximately 36 microns in diameter, from which enough particles have been removed at random without changing the positions of the remaining particles so that the average number of contacts per particle is reduced to four. A spherical particle 36 microns in diameter has approximately the same mass as the average mass of the electrolytic powder particles (see Section 6.2.3), and there are approximately four contacts per particle in the 48 micron electrolytic powder at a pore volume fraction of 0.55 (see Section 6.2.3). A stack of spherical particles formed in this way would have a pore volume fraction of approximately 0.65, and the genus and average number of contacts per particle would be the same as



for the electrolytic powder at a pore volume fraction of 0.55. These structures could be made even more similar by assuming some densification and surface rounding in the stack of spherical particles so that the pore volume fraction and average mean surface curvature would also be the same.

On sintering, such a structure would follow the path of change in genus per gram with decreasing pore volume fraction shown in Figure 106 for the 48 micron electrolytic powder. From this it is apparent that the difference in pore volume fraction at which geometrically similar changes occur in Figure 106 is a result of a difference in particle stacking. A size difference changes only the scale and not the shape of the path the genus per gram follows with decreasing pore volume fraction (see the first part of this section and Appendix 3).

Comparison of the variation in genus per gram for the 48 micron spherical and electrolytic powders can also be made in terms of sintering time. The unsintered density of the electrolytic powder is less than that of the spherical powder, and the sintering time necessary to reach a given density is less for the spherical than for the electrolytic powder, as can be seen from the curves in Figure 116. The variation in genus per gram with sintering time is approximately the same for both powders, as shown by the plots in Figure 117. This is reasonable in that the scale of these systems is nearly the same. The slight differences in the behavior may be due to differences in the channel size distributions; however, this is not considered further, as the differences in the behavior of the curves in Figure 117 may or may not be significant.

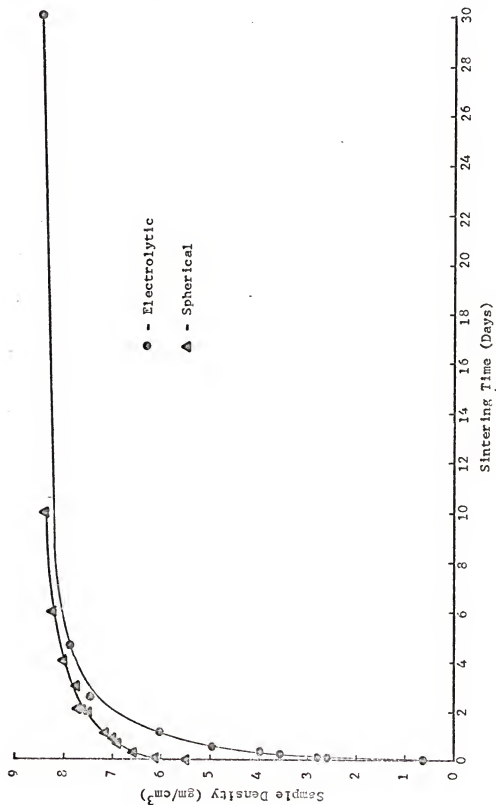


Figure 116. Sample density versus sintering time for 48 micron spherical and electrolytic copper powders.

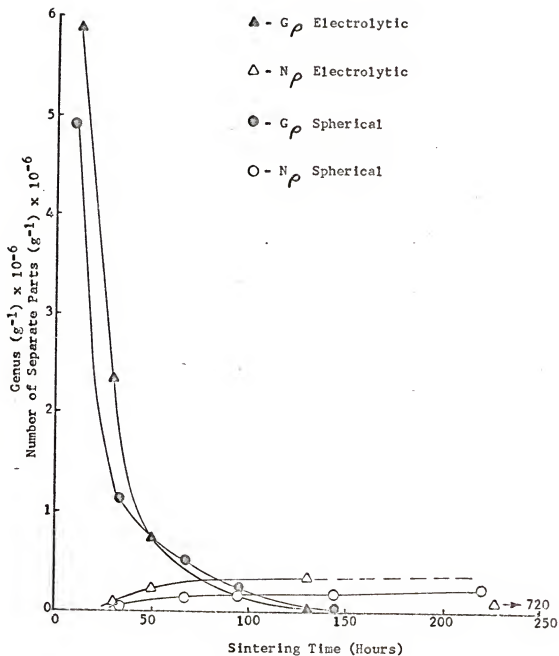


Figure 117. Genus per gram and number of separate parts per gram versus sintering time for 48 micron spherical and electrolytic copper powders.

6.6 Comparison of the Number of Separate Parts per Gram Versus Volume Fraction of Porosity Curves for the 48 Micron Spherical and Electrolytic Copper Powders

The features of the number of separate parts per gram versus pore volume fraction curves for the 48 micron spherical and electrolytic powders are similar, as shown in Figures 82 and 106. Separate parts are not formed in either powder until after channel closure begins. The number of separate parts per gram then increases at a rate which decreases slightly with increasing density until the genus reaches zero. After this, the rate increases with increasing density, as indicated by the data for the spherical powder. This increase probably occurs in the electrolytic powder also; however, the data do not resolve this effect.

The number of separate parts per gram passes through a maximum and then decreases, as indicated by the data for the electrolytic powder. This final decrease must take place as no separate parts are present at bulk density.

These features of the variation in the number of separate parts per gram with pore volume fraction coupled with the variation in the genus indicate that the evolution of the topological properties on sintering is qualitatively similar for both the 48 micron spherical and electrolytic powders for pore volume fractions less than 0.55, although the various changes do not occur at the same pore volume fraction for both powders. As a result, the number of separate parts per gram is greater for the electrolytic powder up to a pore volume fraction of about 0.06, at which point the number of separate parts per gram in the electrolytic powder becomes less than that for the spherical powder.

When the number of separate parts per gram is plotted versus sintering time for these powders, as in Figures 117 and 118, the curves do not cross. Separate parts appear at about the same sintering time for both powders, then the number increases less rapidly with increasing time until the genus reaches zero. This point also occurs at about the same time for both powders. The data for the spherical powder indicate that the rate increases after the genus reaches zero, and the data for the electrolytic powder indicate a final decrease in the number of separate parts per gram.

Thus, the variation of the number of separate parts per gram with time for both powders is quite similar except that the number of separate parts per gram is greater for the electrolytic powder for all sintering times. This is a result of the higher maximum value of genus for the electrolytic powder; this maximum being the largest value of genus before the final decrease in genus begins and not the initial value for the electrolytic powder (see Figure 106). This can be explained as follows.

Equation (7) can be applied to the void space network when branches are taken as channels and nodes are taken as the regions in the void space where channels meet which, after channel closure is complete, remain as separate parts (recall that  $C_P/P_P = \overline{b/n}$ , the average number of branches per node in the deformation retract). If it is assumed that the samples of the spherical and electrolytic powders which have the maximum values of genus in Figure 106 are similar in that  $\overline{b/n}$  is approximately the same for both structures, then the larger maximum value of genus for the electrolytic powder

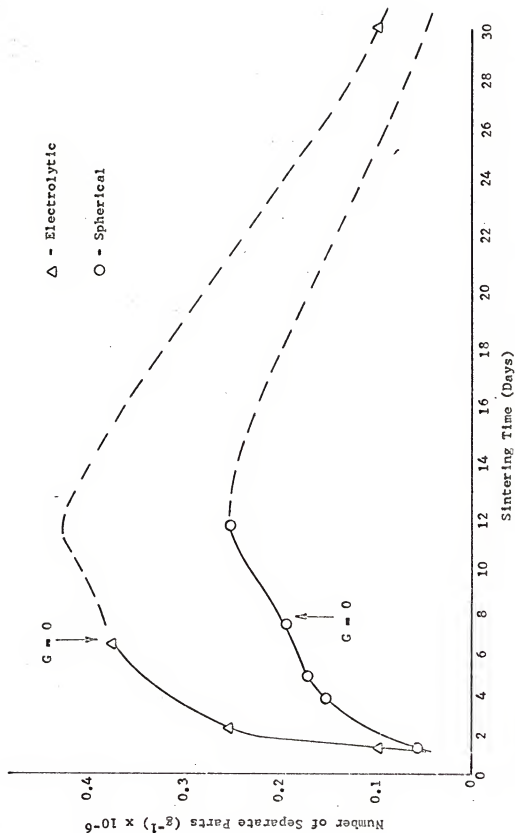


Figure 113. Number of separate parts per gram versus sintering time for 48 micron spherical and electrolytic copper powders.

is accompanied by a larger value of  $N_p$ , according to equation (7). Since  $N_p$  is equal to the number of separate parts present after channel closure is complete, more separate parts will be formed in the electrolytic than in the spherical powder, as observed experimentally.

It is also possible that  $\overline{b/n}$  is less for the electrolytic than for the spherical powders. In this case,  $N_p$  would have to be larger still in order to have the same value of  $G_p$ , as indicated by equation (7). This will be considered further in Section 6.8.

### 6.7 Computer Model

A computer model developed by Steele [3] allows the determination of a number of the topological properties of a node-branch network undergoing random removal of branches. The model is based on the representation of the network by a matrix which allows, by operating on the matrix, the determination of the topological properties of the network as a function of the fraction of branches removed from the network. The properties of interest here are the connectivity, number of separate parts and the size of the separate parts, i.e., the number of nodes in each separate part.

The networks considered by Steele consisted of cubic stacks of six-branch nodes. Such a network can be constructed as follows. A small cube is taken as a node and each of its faces as branches (see Appendix 4). A space-filling stack of these cubes then forms a network of nodes, represented by the small cubes, and branches, represented by the faces, of the small cubes in mutual contact. Two networks are considered; one with all branches which cross the surface of the stack capped at the surface, and the other with all

branches which cross the surface incident on an exterior node. These two cases provide an upper and a lower limit for the connectivity of the stack. This is analogous to the experimental case where an upper and a lower limit for the genus of a sinter structure is determined.

The stacks, or networks, analyzed by Steele had three, four and five vertices, or nodes, on an edge and their properties were determined for the two cases: (1) with and (2) without an exterior node.

The variation in the connectivity and number of separate parts is given in terms of the fractional values of these properties. The fractional connectivity for any given fraction of branches removed is the value of connectivity divided by the initial maximum value of the connectivity,  $G_0$ . The fractional number of separate parts for any given fraction of branches removed is the number of separate parts divided by the final maximum number of separate parts,  $N_0$ . The maximum number of separate parts is equal to the number of nodes or cubes in each network.

These fractional Betti numbers are plotted versus fraction of branches removed in Figures 119 and 120 for the  $3 \times 3 \times 3$ ,  $4 \times 4 \times 4$  and  $5 \times 5 \times 5$  networks with and without the exterior node, respectively. These data were obtained by making a number of computer runs and averaging the results. As the size of the network increases, the slope of the initial part of the  $G/G_0$  curves and the final part of the  $N/N_0$  curves approaches the dotted lines. These dotted lines represent the initial slope of the  $G/G_0$  curve and the final slope of the  $N/N_0$  curve for a network of infinite size. These limiting slopes were obtained by plotting the



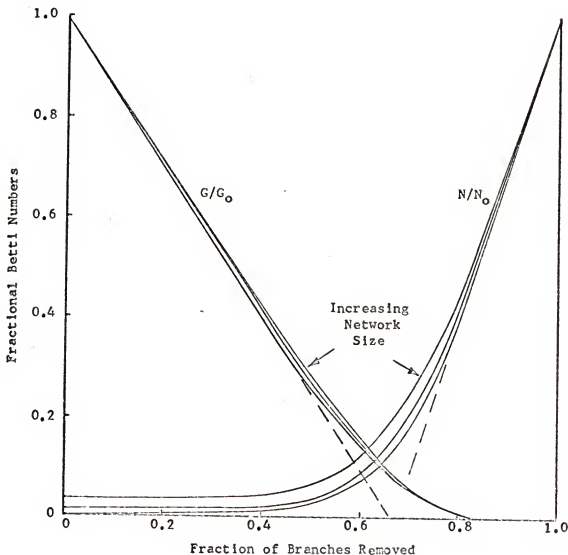


Figure 119. Average variation in  $G/G_0$  and  $N/N_0$  for the  $3 \times 3 \times 3$ ,  $4 \times 4 \times 4$  and  $5 \times 5 \times 5$  network models with the exterior node. The arrows indicate the direction in which the curves shift with increasing number of nodes, which is toward the limiting slopes shown by the dashed lines. (Steele [3]).

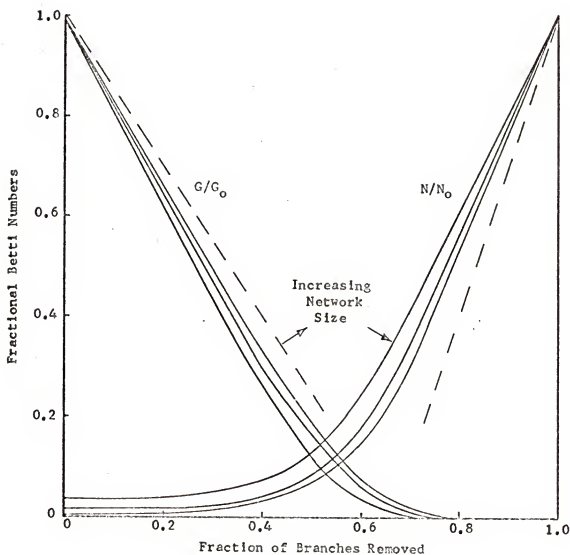


Figure 120. Average variation in  $G/G_0$  and  $N/N_0$  for the  $3 \times 3 \times 3$ ,  $4 \times 4 \times 4$  and  $5 \times 5 \times 5$  network models without the exterior node. The arrows indicate the direction in which the curves shift with increasing number of nodes, which is toward the limiting slopes shown by the dashed lines. (Steele [3]).

values of the slopes for each size network versus  $1/n$ , where  $n$  is the number of nodes or cubes on an edge of the network, and taking the limiting value as  $1/n$  goes to zero.

From the curves of Figures 119 and 120, the following estimates can be made for very large networks:

1. Twenty-five per cent of the branches must be randomly removed before the first isolated separate part is formed.
2. Ninety-two to 95 per cent of the branches must be randomly removed before the connectivity is reduced to zero.

The distribution of the nodes among the separate parts as a function of the fraction of branches removed was also obtained by Steele, again by making a number of computer runs and averaging the results. The separate parts are classified by type according to the number of nodes they contain. The data represent the fraction of the total number of nodes in the network which are contained in separate parts of the given type. Figures 121 and 122 show the distribution of the types of separate parts formed for the  $5 \times 5 \times 5$  network with and without the external node, respectively. The two curves for each type of separate part, with and without the external node, converge as the size of the network increases.

The distribution of the connectivity of the isolated separate parts was also obtained. The distributions obtained for the  $5 \times 5 \times 5$  network are shown in Figure 123. These data were also obtained by making a number of computer runs and averaging the results. These curves show that the multiple connectivity present at any fraction of branches removed is almost entirely contained within a single part. This part is the main connected portion of the network.

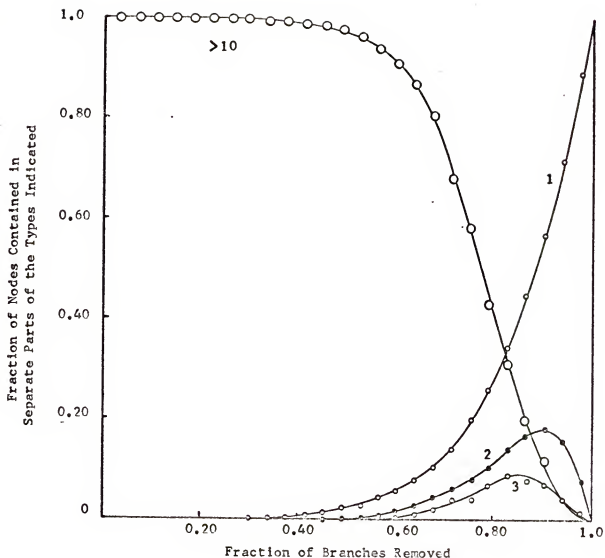


Figure 121. Average distribution of nodes among different types of separate parts for the  $5 \times 5 \times 5$  network with the exterior node. The curves represent the fraction of nodes contained in separate parts having the number of nodes indicated (1 for isolated nodes, 2 for isolated pairs of nodes, etc.). (Steele [3]).

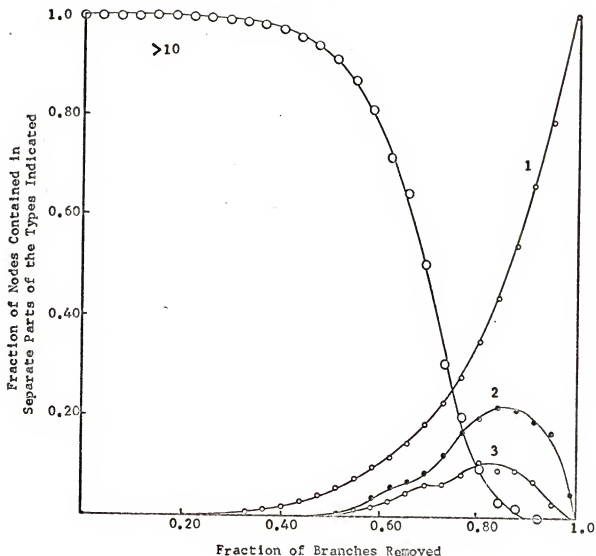


Figure 122. Average distribution of nodes among different types of separate parts for the  $5 \times 5 \times 5$  network without the exterior node. The curves represent the fraction of nodes contained in separate parts having the number of nodes indicated (1 for isolated nodes, 2 for isolated pairs of nodes, etc.). (Steele [3]).

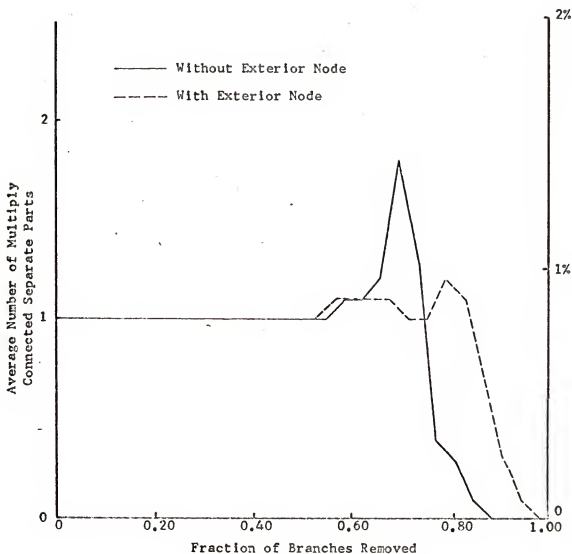


Figure 123. Average number of multiply connected separate parts in the  $5 \times 5 \times 5$  network models with and without the exterior node. (Steele [3]).

The number of multiply connected separate parts increases between 70 and 80 per cent of the branches removed. In this range, the connectivity is less than 10 per cent of its maximum value and is approaching zero. It is in this range of genus for an actual sinter structure that tree-like regions are expected to be formed in the void space network. Recall also that separate parts are being formed rapidly and most effectively per channel closure event in this range of genus. Therefore, it is expected that since some connectivity remains in the network, separate parts possessing multiple connectivity would most likely be found at this point in the sintering process.

The distribution of the types of and the connectivity of the separate parts predicted by Steele's model indicate that random branch removal maintains a single, highly connected network from which single nodes or pairs of nodes predominantly are isolated. This is in agreement with the experimental result that only one multiply connected separate part was found during the course of this work, and that a large fraction of the separate parts are small.

Therefore, both the computer model and the experimental results indicate that a tree or trees are formed by the void space network of a sinter body as the genus approaches zero, and that the number of multiply connected separate parts formed is small.

#### 6.8 Correlation Between the Computer Model Data and the Experimental Data

In order to compare the results of the computer model with the experimental data, it is necessary to determine fractional values

of genus for the experimental data. The value used as the denominator is the largest value of genus reached before second-stage sintering begins,  $G_{op}$ . The resulting fractional values are given in Tables 16, 17 and 18 for the 115 micron spherical, 48 micron spherical and 48 micron electrolytic powders, respectively.

A correlation between the variation in the experimental values of the fractional Betti numbers and the fraction of branches removed can be obtained under the following conditions [3]:

1. Assume a simple cubic void-channel network; that is, each void has six channels incident on it. A void is taken as a portion of the void space which would remain after all channels in the structure had closed.
2. Each channel closure event produces either a unit decrease in the genus or a unit increase in the number of separate parts.
3. The maximum number of channels is thus  $G_0 + N_0$ , which is equal to  $3/2 G_0$  for a simple cubic network (six branches per node).

Under these conditions, the number of channels closed at any density is equal to the sum of the decrease in genus from the maximum value and the increase in the number of separate parts from zero. The data thus obtained are presented in Tables 16, 17 and 18 for the 115 micron spherical, 48 micron spherical and 48 micron electrolytic powders, respectively. The fractional values of genus and number of separate parts are plotted versus fraction of branches removed for these three powders in Figure 124. The values of fractional genus for all three powders are forced to follow the same curve until about 30 per cent of the branches are removed when the first separate parts



Table 16. Computer model data for the 115 micron spherical copper powder.

$$G_{op} = 3.56 \times 10^5 \text{ gm}^{-1*}$$

$$N_{op} = G_{op} / 2^{**} = 1.78 \times 10^5 \text{ gm}^{-1}$$

$$\begin{aligned} \text{Maximum Number of Channels}^{**} = \\ G_{op} + N_{op} = 3/2 G_{op} = 5.34 \times 10^5 \text{ gm}^{-1} \end{aligned}$$

Density (gm/cm <sup>3</sup> )	$G_p \times 10^{-5} (\text{gm}^{-1})$	$G_p / G_{op}$	$N \times 10^{-5}$ (gm <sup>-1</sup> )	$N_p / N_{op}$	Fraction of Channels Closed
6.67	2.28	0.64	0	0	0.24
7.05	1.35	0.38	0	0	0.41
7.50	0.734	0.21	0.08***	0.04	0.545
7.76	0.483	0.14	0.105***	0.059	0.60
8.05	0.217	0.061	0.15	0.084	0.65

\*Obtained by dividing maximum value in Figure 115 by 13.74.

\*\*This assumes six branches per node in the void space.

\*\*\*Obtained by taking value for -270 +325 mesh spherical powder divided by 13.74.

Table 17. Computer model data for the 48 micron spherical copper powder.

$$G_{op} = 4.90 \times 10^6 \text{ gm}^{-1}$$

$$N_{op} = G_{op} / 2^* = 2.45 \times 10^6 \text{ gm}^{-1}$$

$$\begin{aligned} &\text{Maximum Number of Channels}^* = \\ G_{op} + N_{op} &= 3/2 G_{op} = 7.35 \times 10^6 \text{ gm}^{-1} \end{aligned}$$

Density (gm/cm <sup>3</sup> )	$G_p \times 10^{-6} \text{ (gm}^{-1}\text{)}$	$G_p / G_{op}$	$N_p \times 10^{-6}$ (gm <sup>-1</sup> )	$N_p / N_{op}$	Fraction of Channels Closed
7.26	1.14	0.23	0.059	0.024	0.52
7.74	0.55	0.11	0.15	0.061	0.61
8.00	0.28	0.057	0.18	0.073	0.65
8.25	0.038	0.0078	0.19	0.078	0.69
8.40	0	0	0.25	0.102	0.70

\*This assumes six branches per node in the void space.

Table 18. Computer model data for the 48 micron electrolytic copper powder.

$$\begin{aligned}
 G_{op} &= 5.79 \times 10^6 \text{ gm}^{-1} \\
 N_{op} &= G_{op} / 2^* = 2.90 \times 10^6 \text{ gm}^{-1} \\
 \text{Maximum Number of Channels}^* &= \\
 G_{op} + N_{op} &= 3/2 G_o = 8.69 \times 10^6 \text{ gm}^{-1}
 \end{aligned}$$

Density (gm/cm <sup>3</sup> )	$G_p \times 10^{-6} (\text{gm}^{-1})$	$G_p / G_{op}$	$N_p \times 10^{-6}$ (gm <sup>-1</sup> )	$N_p / N_{op}$	Fraction of Channels Closed
6.05	2.40	0.415	0.105	0.036	0.403
6.95	0.824	0.142	0.272	0.094	0.603
7.92	0.048	0.0083	0.402	0.139	0.707

\*This assumes six branches per node in the void space.

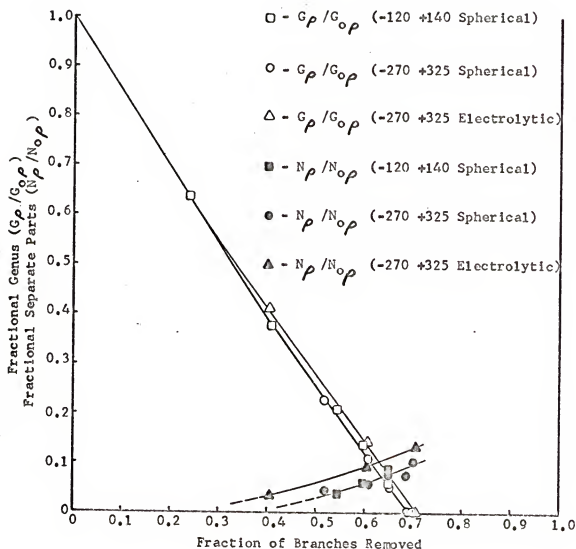


Figure 124. Correlation of the computer model results and the experimental data for the 115 micron spherical and 48 micron spherical and electrolytic powders.

are isolated. This is because the initial portion of these curves is controlled by the number of channels incident on each void, six in this case according to the previous assumption. Note that this coordination number is for the void and not the solid space. The coordination number for the solid space was considered earlier in this chapter (Sections 6.2.1 and 6.2.3). Steele shows that the initial slope of these curves is given by

$$\text{Slope} = \frac{-1}{1 - (2/\overline{b/n})} \quad (28)$$

where  $\overline{b/n}$  is the number of branches or channels incident on each node or void, respectively. Since  $\overline{b/n}$ , the coordination number, is assumed to be six, the data in Figure 124 must all lie on a line whose slope is  $-3/2$  when less than about 30 per cent of the branches have been removed.

Separate parts are observed experimentally after approximately 25 to 30 per cent of the channels have closed, which agrees closely with the results of the computer model (see Section 6.7). As separate parts begin to form, the data deviate from linearity because the fraction of branches removed is increased without an accompanying decrease in genus. Since the values of fractional number of separate parts are greater for the electrolytic than for the spherical powders, for the same fraction of branches removed, the fractional values of genus for the electrolytic powder lie to the right of those for the spherical powders in Figure 124.

The fact that the fractional number of separate parts is greater for the electrolytic than for the spherical powders indicates that the coordination number is less for the void space

network of the electrolytic powder than for the spherical powders. This can be shown as follows.

Consider equation (7). The average number of branches per node is given by

$$\overline{b/n} = \frac{CN}{2} \quad (29)$$

where CN is the coordination number. Substituting this in equation (7) and solving for  $N_{op}$  gives

$$N_{op} = \frac{2G_{op}}{CN - 2} \quad (30)$$

where  $N_{op}$  and  $G_{op}$  are the maximum values of number of nodes per gram and genus per gram, respectively. Therefore,  $G_{op}$  is the value of genus before channel closure begins, and  $N_{op}$  is the number of separate parts which would be present if all channels closed. Taking the inverse of equation (30) and multiplying both sides by  $N_p$ , the number of separate parts per gram, gives

$$\frac{N_p}{N_{op}} = \frac{N_p (CN - 2)}{2G_{op}} \quad (31)$$

The ratio  $N_p/N_{op}$  is the fractional value of the number of separate parts per gram.

Now consider the situation when the fractional separate parts curves for the spherical and electrolytic powders of Figure 124 are forced to superimpose rather than the fractional genus curves in Figure 124. This can be done for each value of fraction of branches removed as follows. Consider the values for 60 per cent of the branches removed. Here  $N_p/N_{op}$  is 0.06 for the spherical powders, and  $N_p$  is  $0.27 \times 10^6$  for the electrolytic powder. Taking 0.06 as the value of  $N_p/N_{op}$  for the electrolytic powder forces the values of fractional separate parts to coincide for the electrolytic and

spherical powders. Putting these values into equation (31) and solving for CN, a value of 4.57 is obtained. The value of 4.57 is not significant since a coordination number of 6.0 was assumed for the spherical powders. This result only indicates that the coordination number for the void space of the 48 micron electrolytic powder is less than that for a single size fraction of spherical powder by a factor of approximately  $4.57/6 = 0.76$ .

The computer model results for the  $5 \times 5 \times 5$  network are shown in Figure 125 with the experimental curves of Figure 124 superimposed. The experimental data do not approach zero fractional genus with increasing fraction of branches removed as slowly as the computer model data, nor do the fractional separate parts data increase as rapidly with increasing fraction of branches removed as the computer model data. This is because fewer separate parts are actually formed than predicted by the computer model. This could be due to the occurrence of either or both of two phenomena: (1) the disappearance of separate parts; or (2) the failure of channels between some voids to close. For example, three voids and the channels between them could form one separate part, as illustrated in the left side of Figure 96. This phenomenon is referred to as agglomeration of separate parts by Steele [3]. This agglomeration process can occur in connected portions of the void-space network and is not necessarily associated with the presence of separate parts. In either case, agglomeration reduces the number of channels independent of the channel closure process, that is, without the closure of channels.

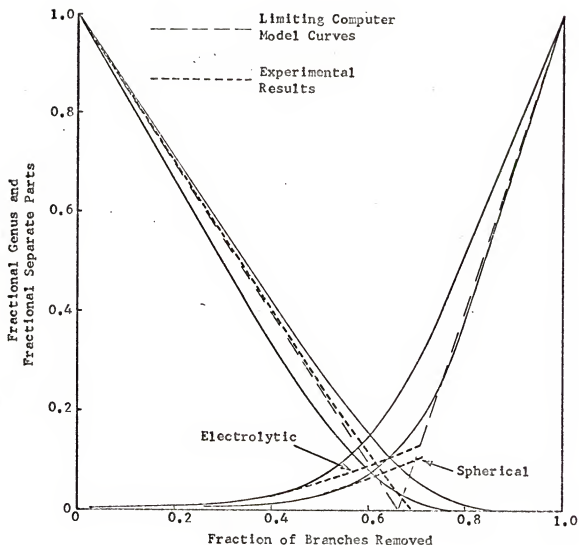


Figure 125. Comparison of the computer model results and the experimental results for the 115 micron spherical and 48 micron spherical and electrolytic powders.



Further evidence for the disappearance of separate parts and/or agglomeration is indicated by the curves in Figure 126 which show the relation between fraction of channels closed and volume fraction of porosity during second-stage sintering for the spherical and electrolytic powders. The fact that the spherical powders lie on the same curve again shows the similarity in their sintering behavior. The tendency for all three powders to reach bulk density at a value for fraction of channels closed less than 1.0 indicates that either separate parts have been removed or agglomeration is removing channels.

The curves of Figure 126 also show that the density change per channel closure event increases with density for all three powders. This figure indicates that channel closure and densification are associated, but not necessarily mutually dependent upon each other. This is apparent since densification takes place during first-stage sintering before channel closure begins and during third-stage sintering when all channels have closed and only simply connected, nearly spherical separate parts remain in the structure. The observed increase in density change per channel closure event is a result of fewer channels closing while densification continues by some mechanism or mechanisms which do not depend on channel closure. For example, it may be possible for some channels to close entirely as a result of surface rounding, in which case no densification is involved. However, it may be necessary for densification to occur before other channels can close, densification being necessary before the dimensions of these channels reach an unstable configuration.

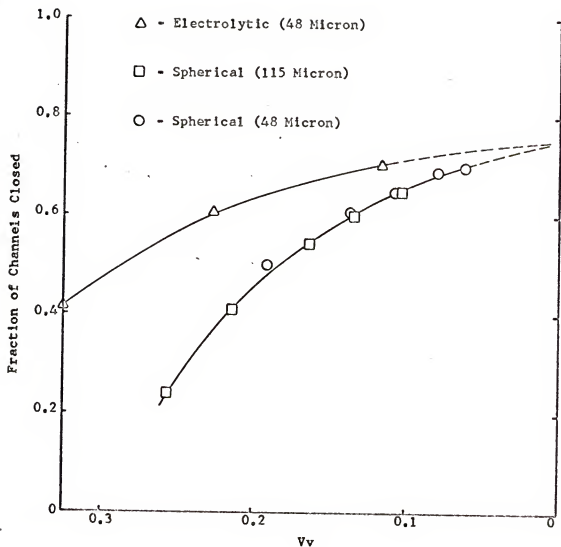


Figure 126. Fraction of branches removed versus volume fraction of porosity for the 115 micron spherical and 48 micron spherical and electrolytic powders.

### 6.9 Variation in the Void-Solid Interface Area During Sintering for the 48 Micron Spherical and Electrolytic Copper Powders

Surface area per unit mass,  $S_p$ , and per unit volume,  $S_v$ , are plotted versus pore volume fraction in Figure 86 for the 48 micron spherical and electrolytic powders. Values of surface area per gram lie on one curve, and values of surface area per cc lie on another curve for both powders. The surface area per cc curve exhibits linear behavior in the range of pore volume fraction from 0.275 to 0.05. This covers the channel closure stage or second stage of sintering for the spherical powder. Equation (20) indicates that the mean pore intercept,  $\bar{\lambda}$ , is constant over the density range where the plot of surface area per unit volume versus pore volume fraction exhibits linear behavior. Since the data for both the 48 micron spherical and electrolytic powders lie on the same curve in the range of pore volume fraction from 0.275 to 0.05, the mean pore intercept is the same for these powders in this density range.

The curve for the electrolytic powder starts at about 15 per cent of bulk density with the largest value of surface area per cc and then decreases with increasing density until a pore volume fraction of 0.55 is reached. It then increases with increasing density until a pore volume fraction of 0.45 is reached, after which it follows the same, approximately linear, decrease exhibited by the spherical powder. These features can be explained as follows.

The initial decrease in surface area per cc for the electrolytic powder is accompanied by a large decrease in genus as the result of closure of small channels and/or pulling apart of filaments (see Section 6.2.3). Both of these phenomena are accompanied by a

decrease in surface area. The fact that the rate of decrease of surface area per cc increases in this density range is a result of two competing effects. First, surface area is pulled into a given unit of volume occupied by the sinter structure as the result of shrinkage of the sinter body. This effect tends to increase the surface area per cc with increasing density. Second, channel closure and/or pulling apart of filaments and surface rounding produce a decrease in the surface area. The rate of shrinkage decreases with increasing density; thus the rate at which surface area is pulled into unit volume of structure decreases with increasing density. The rate of channel closure and/or pulling apart of filaments remains approximately constant, as shown in Figure 73. As a result of this variation in these competing effects, the increase in the rate of decrease, as exhibited by the electrolytic powder, is expected. This is illustrated schematically in Figure 127. Curve A shows the increase in surface area per cc produced by shrinkage, and curve B shows the variation in surface area per cc produced by actual structural changes. The sum of curves A and B gives curve C, the actual variation in the surface area per cc, which has the same shape as the initial part of the curve of surface area per gram for the electrolytic powder shown in Figure 86.

In the following discussion, the changes referred to are with respect to increasing density.

The increase in surface area per cc in the range of pore volume fraction from 0.55 to 0.45 is a result of the first effect mentioned above, that is, shrinkage of the sinter structure pulling more surface area into unit volume of the structure. That this

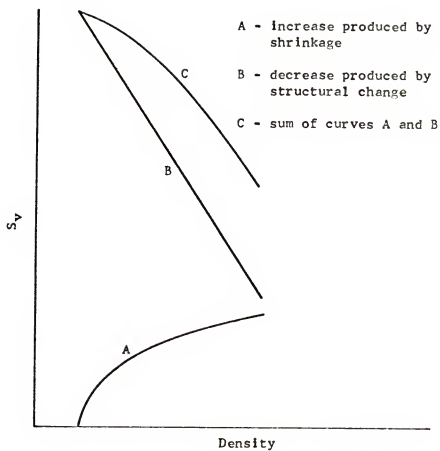


Figure 127. Illustration of the variation in the surface area per unit volume with sample density during the initial decrease in genus for the 48 micron electrolytic powder.

effect can produce the observed increase in surface area is shown by the following.

At a density of 3.99 gm/cc, there is  $147 \text{ cm}^2/\text{gm}$  of surface area. If the value of surface area per gram remained the same at a density of 4.95 gm/cc, there would be  $730 \text{ cm}^2/\text{cc}$  rather than the observed  $676 \text{ cm}^2/\text{cc}$  present at a density of 4.96 gm/cc. Therefore, it is possible for the observed increase in surface area per unit volume to occur while the total surface area of the sinter structure decreases. That the total possible increase does not take place is probably due to the removal of some surface area as a result of surface rounding.

The observed increase in surface area per unit volume is therefore a result of the condition that phenomena which remove surface area are not occurring rapidly enough to overcome the increase accompanying shrinkage. This is in agreement with the observation that, while the surface area per unit volume is increasing, the genus is also increasing. Thus, channel closure and the accompanying reduction in surface area is not occurring at a significant rate relative to the rate of increase in surface area per unit volume resulting from shrinkage.

The increase in surface area per cc with increasing density observed for the electrolytic powder apparently does not occur in the 48 micron spherical powder during first-stage sintering. However, a number of spherical powders apparently exhibit a small or zero slope in a plot of surface area per cc versus sample density for a period during first-stage sintering [32]. The spherical powder has necks with large curvature gradients present during first-stage

sintering; hence, considerable surface rounding takes place. This is accompanied by a decrease in surface area which is apparently greater than the increase in surface area per unit volume produced by shrinkage. The amount of surface rounding is considerably less for the electrolytic powder as curvature gradients have had time to sinter out to some extent before the range of density over which surface area per unit volume increases is reached.

Further support for this basis for the difference in the behavior of the spherical and electrolytic powders lies in the curvature plots of Figures 87 and 88. The electrolytic powder exhibits little change in total curvature or average mean surface curvature in the range of density where the surface area per unit volume is increasing. The spherical powder, however, exhibits a large change in both these parameters during first-stage sintering as a result of surface rounding.

The linear decrease in surface area per unit volume with increasing density exhibited by the electrolytic powder occurs during second-stage sintering. This covers the density range over which large-scale channels are closing. This linear behavior is well documented by DeHoff, *et al.* [32] and Rhines, *et al.* [33].

The surface area per cc versus pore volume fraction curve deviates negatively from linearity during the third stage of sintering. This deviation from linearity is a result of the conglomeration process [2]; i.e., small separate parts decrease in size and disappear while larger separate parts grow. This produces a coarsening of the size distribution of the separate parts which is accompanied by an increase in the mean pore intercept. Equation

(20) indicates that if  $\bar{\lambda}$  increases with decreasing pore volume fraction, the surface area per unit volume versus pore volume fraction curve must deviate negatively from linearity. Therefore, the experimental observations agree with the expected occurrence of the conglomeration process.

The surface area per gram curve for the electrolytic and spherical powders shown in Figure 86 has the following features. For pore volume fractions greater than 0.55, the electrolytic powder exhibits a rapid decrease in surface area per gram with increasing density. The rate of this decrease is largest at low density and decreases with increasing density. This is probably a result of decreasing curvature gradients which is accompanied by a decrease in the rate of surface rounding. At a pore volume fraction of 0.55, closure of small channels and/or pulling apart of filaments is complete. This results in a slower rate of decrease of surface area per gram starting at a pore volume fraction of 0.55. The surface area per gram decreases in the range of pore volume fraction from 0.55 to 0.45 in contrast to the increase in surface area per cc in this density range. This is in agreement with the fact that the energy which produces sintering is obtained through a reduction in surface energy or surface area throughout the sintering process.

When a pore volume fraction of 0.45 is reached, the surface area per gram begins to decrease more rapidly as a result of the closure of large channels. The rate of this decrease becomes less, due to the decreasing rate of channel closure, until a pore volume fraction of 0.12 is reached. At this point, the rate of decrease once again increases.



The break in the surface area per gram curve at a pore volume fraction of about 0.12 occurs when channel closure ceases. Conglobation of separate parts and the accompanying coarsening of the size distribution of separate parts produce the accelerated rate of decrease in the surface area per gram curve below a pore volume fraction of 0.12. The spherical powder appears to follow the same curve; however, the data are not sufficient to resolve whether or not a break occurs when channel closure ends in this material.

Consider again the linear behavior of the surface area per unit volume versus pore volume fraction curves during second-stage sintering. The void-solid interface present during second-stage sintering has been referred to as a conditional minimal surface [34]. The conditional minimal surface has the minimum surface area consistent with the existing conditions of genus and pore volume fraction of the structure.

As each channel closes, a new minimal surface is created subject to the new conditions of genus and pore volume fraction. Each channel closure event may produce the same ratio of surface area removed to density increase independent of channel size [34]. As a result of these geometric constraints on the void-solid interface and the channel closure event, linear behavior is expected during second-stage sintering.

Consider Figure 128, which shows a plot of the number of channels removed versus surface area per gram for the 48 micron spherical and electrolytic powders. There is a marked difference in the behavior of these powders. The slope of the curve for the electrolytic powder is relatively constant, indicating the existence

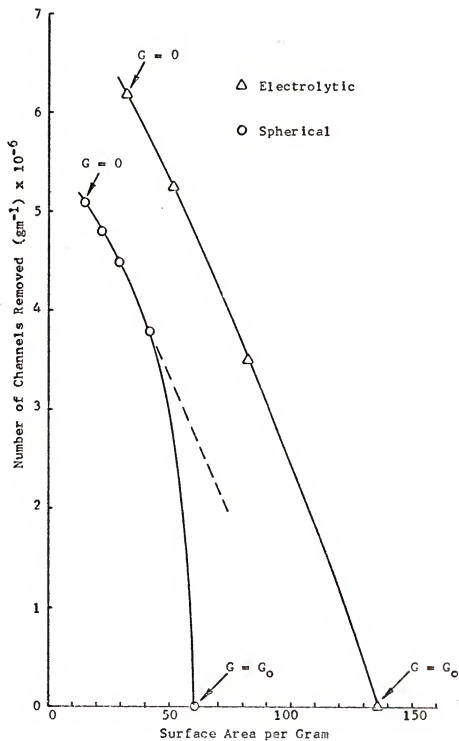


Figure 128. Number of channels removed versus surface area per gram for 48 micron spherical and electrolytic copper powders.

of similar conditions as far as channel closure is concerned throughout the channel closure process. A minimal surface would be expected to behave in this way.

The spherical powder exhibits considerably greater deviation from linearity than the electrolytic powder in Figure 128. The greatest deviation occurs during the first portion of the channel closure process if the curve established by the remaining four data points is taken as an indication of minimal behavior. This deviation of the spherical powder data from minimal behavior, indicated by the dotted line, can be described as a "channel excess" condition; that is, there are more channels in the surface than the curvature of the surface can support. These channels are probably, for the most part, the built-in three-channels of the structure. They close rapidly with increasing density, as indicated in Figure 61, and with little accompanying surface area change, as indicated by Figure 128.

The surface area removed per channel closure event is nearly the same for both powders at high density, as indicated by the slopes of the curves in Figure 124 at high density (low  $S_p$ ). Recall that the mean pore intercept is also the same for these powders throughout second-stage sintering (see Section 6.9). These structures are compared further in terms of curvature of the void-solid interface and grain boundary structure in Sections 6.10 and 6.11, respectively.

#### 6.10 Variation in Total Curvature per Unit Volume and Average Mean Curvature During Sintering for the 48 Micron Spherical and Electrolytic Copper Powders

The variation in total curvature per unit volume and average mean surface curvature for the spherical powder agrees well with the geometric changes discussed previously. Both parameters begin at a

large positive value, as shown in Figures 87 and 88, and decrease rapidly with increasing density. This decrease continues throughout first-stage sintering and is the result of the positively curved surfaces of the particles being replaced by necks which have one negative and one positive radius of curvature (saddle surface).

When channel closure begins, the average mean surface curvature continues to decrease because positive curvature is being replaced by negative curvature, as shown schematically in Figure 129. In Figure 129a, an open channel is shown which has one negative and one positive radius of curvature. When this channel closes, two negative radii of curvature result, as shown in Figure 129b. Thus, the average mean surface curvature decreases as a result of channel closure. This decrease continues until channel closure is complete. The ensuing conglomeration of separate parts and the coarsening of their size distribution cause negative curvature to be replaced by less negative curvature; therefore, the average mean surface curvature becomes less negative late in the sintering process.

The total curvature per unit volume for both the electrolytic and spherical powders first becomes more negative, reaches a minimum and then becomes less negative with increasing density, as shown in the curves of Figure 87. The total curvature per unit volume becomes less negative because the surface area decreases. As the surface area per unit volume tends toward zero, the total curvature per unit volume must also tend toward zero. This is in spite of a negative increase in the value of average mean surface curvature in the same density range for both the spherical and electrolytic powders.

The average mean surface curvature of the electrolytic powder exhibits essentially the same features as the spherical powder. A decrease takes place up to a pore volume fraction of 0.55 due to

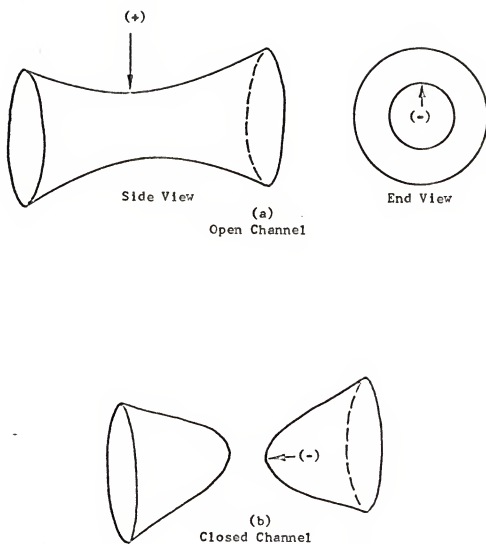


Figure 129. Illustration of the curvature change associated with the channel closure event.

the closure of small channels and surface rounding. In the range of pore volume fraction from 0.55 to 0.45, the decrease continues as a result of surface rounding. Few, if any, channels are closing in this density range. Another effect occurring in this density range which reduces the average mean surface curvature is the formation of contacts. An event of this type removes areas of positive curvature and replaces them with a neck which has one negative radius of curvature.

The decrease in average mean surface curvature continues during the closure of large channels. After channel closure is complete and third-stage sintering is reached, the average mean surface curvature begins to increase, as in the case of the spherical powder.

#### 6.11 Variation in Grain Boundary Structure During Sintering for the 48 Micron Spherical and Electrolytic Copper Powders

The features of the dependence of grain boundary area per cc and grain boundary area per gram on pore volume fraction, as shown in Figures 89 and 90, respectively, are similar for both the spherical and electrolytic powders. The electrolytic powder exhibits an increase in the range of pore volume fraction from 0.55 to 0.45. The increase is larger for the grain boundary area per cc curve because grain boundary area is pulled into unit volume as the result of shrinkage; however, the increase is not produced entirely by this effect as the grain boundary area per gram curve also increases. This increase is caused by neck growth, as nearly all particles are joined at a grain boundary, and by the formation of contacts, most of which produce more grain boundary area.

From a pore volume fraction of 0.45 to 0.12, the grain boundary area per cc and per gram for the electrolytic powder decreases with increasing density. In this density range, channels are closing and void space is being eliminated. The grain boundaries should be pinned less effectively, and, as a result, grain growth occurs. The grain boundary area per cc decreases less rapidly than the grain boundary area per gram due to the shrinkage effect.

At a pore volume fraction of about 0.14, exaggerated grain growth begins and both grain boundary area per cc and grain boundary area per gram decrease rapidly with increasing density.

The spherical powder exhibits somewhat different behavior. Both the grain boundary area per cc and the grain boundary area per gram increase with increasing density during first-stage sintering and during the first portion of second-stage sintering. These parameters decrease after exaggerated grain growth begins at a pore volume fraction of about 0.14. The increase in these parameters during first-stage and well into second-stage sintering is expected to accompany neck growth which occurs during this period.

There is one essential difference in the behavior of these parameters for the spherical and electrolytic powders. In terms of variation in the grain boundary area, the electrolytic powder exhibits three distinct regions of behavior, (1) neck growth and contact formation, (2) channel closure and (3) exaggerated grain growth, while the spherical powder has only two, (1) neck growth and contact formation and (2) exaggerated grain growth.

Channel closure in the spherical powder does not begin until a pore volume fraction of about 0.25 is reached. Since exaggerated

grain growth occurs at a pore volume fraction of about 0.14, channel closure only occurs over a narrow range of pore volume fraction. Necks are still growing in this range, and their influence on the variation in grain boundary area is apparently dominant in this range. Exaggerated grain growth then takes place before normal grain growth becomes a significant factor in this powder. From this behavior, it is apparent that channel closure has little influence on the variation in grain boundary area for the spherical powder, whereas channel closure is dominant over a large portion of the sintering process in the electrolytic powder.

The fact that exaggerated grain growth occurs at the same pore volume fraction for both powders indicates that the connectivity of the void space is not an important controlling factor in regard to inhibiting exaggerated grain growth. The genus per gram of these powders is different by about a factor of two at a pore volume fraction of 0.14 (see Figure 106).

The total grain surface area per cc and per gram behaves as shown in Figures 91 and 92, respectively. These curves can be explained by combining the discussion above with that of Section 6.11. Note that the data in Figures 89, 90, 91 and 92 lie on the same curves for both powders for pore volume fractions less than about 0.12.

The variation of mean grain intercept during sintering is shown in Figure 93 for both powders. The spherical powder exhibits some increase in mean grain intercept in the range of pore volume fraction from 0.42 to 0.25 as a result of neck growth. In the density range accompanying channel closure, little or no change takes place from a pore volume fraction of 0.25 to 0.2; however, an increase



takes place in the range from 0.2 to 0.14. The electrolytic powder exhibits little change in the mean grain intercept while contacts are forming ( $V_v = 0.55$  to 0.45). An increase takes place in the range of pore volume fraction from 0.45 to 0.14 as channels are closing. The following conclusions can be drawn from this behavior.

The grain size, as indicated by the mean grain intercept, increases and the grain boundary area decreases as channels close in the electrolytic powder. The grain size in the spherical powder does not begin to increase until a volume fraction of about 0.2 is reached. Channels begin to close at a pore volume fraction of 0.25; however, the conditional minimal configuration (see Section 6.9) is not reached until the pore volume fraction decreases to about 0.2. The conditional minimal configuration is reached in the electrolytic powder at a pore volume fraction of 0.45, which is when the grain size increase accompanied by channel closure begins for this powder. Therefore, it is apparent that the conditional minimal configuration is important in regard to normal grain growth.

From the preceding discussion, it is concluded that the important factors regarding normal grain growth are probably the curvature and genus of the void-solid interface. The curvature and genus both decrease rapidly with increasing density for the spherical powder until the conditional minimal configuration is reached. The rapid decrease in curvature indicates that surface rounding associated with neck growth is still an important factor even after channel closure begins in the spherical powder. The increase in grain boundary area per gram associated with this neck growth is apparently larger than the decrease in grain boundary

area per gram produced by grain growth accompanying channel closure. Therefore, the grain boundary area per gram continues to increase in the spherical powder after channel closure begins. This continues until exaggerated grain growth starts at a pore volume fraction of about 0.14.

After the conditional minimal configuration is reached, further channel closure is apparently accompanied by normal grain growth in the electrolytic powder. This is not observed in the spherical powder because the conditional minimal configuration is reached at approximately the same pore volume fraction at which exaggerated grain growth begins.

Steele [3] has pointed out that genus and grain growth may be related. The experimental data discussed in this section indicate that this is apparently the case for normal grain growth; however, exaggerated grain growth is apparently not affected by differences in genus.

#### 6.12 General Features of the Sintering Process

From the discussion presented in the preceding sections, it is apparent that the variation of a number of the metric properties during sintering can be better understood through consideration of the topological properties. The combination of the metric and topological properties yields the following general description of the sintering process.

The sintering process can be divided into three distinct stages of structural change, each of which is characterized by a different geometric process and path of structural change.

The geometric change which characterizes the first stage depends in part on the shape of the powder particles. The changes which occur during the first stage are restricted to the region of the contacts between particles. In the irregular electrolytic powder, small channels close, filaments pull apart and contacts between particles increase in size. This is accompanied by the removal of short-range surface irregularities. The first stage in the less irregularly shaped spherical powders is characterized by growth of contacts between particles, that is, neck growth, and by the removal of short-range surface irregularities. The genus decreases in the irregular powder and increases or remains nearly constant in the spherical powder. Therefore, this stage cannot be generally characterized according to the variation in the topological properties. The surface area per gram decreases, while the surface area per unit volume may increase, decrease or remain unchanged. The average mean surface curvature becomes more negative and the mean grain intercept remains nearly constant or increases slightly. The grain boundaries remain pinned in the neck regions between particles.

Channel closure characterizes the second stage of sintering. As a result of channel closure, the genus decreases toward zero and separate parts are isolated. The average mean surface curvature continues to become more negative. The surface area per unit volume decreases linearly with pore volume fraction, and the mean pore intercept remains constant during the second stage. Before channel closure begins, triple lines in the grain structure are nearly all of the type void-solid-solid and the grain boundaries

are pinned by the void space network. As channels close, triple lines of the type solid-solid-solid are formed. As a result, the grain structure becomes less anchored by the void space network, and grain growth begins. This continues until the genus is nearly zero, at which time exaggerated grain growth begins and the mean grain intercept begins to increase rapidly.

The third stage of sintering is reached when channel closure is complete. This stage is characterized by conglomeration of the isolated separate parts. The surface area per unit volume deviates negatively from linearity with decreasing pore volume fraction, and the average mean surface curvature becomes less negative. The mean pore intercept increases slightly, and the mean grain intercept continues to increase rapidly as a result of exaggerated grain growth.

### 6.13 Sampling Error Involved in the Determination of the Genus and Number of Separate Parts

#### 6.13.1 Difference Between $G_V^{\max}$ and $G_V^{\min}$

Recall that a maximum and minimum limit of the value of genus is determined by means of Method III presented in Chapter IV. That these values bracket the actual value of genus is demonstrated by means of an ideal node-branch network in Appendix 4. It is also shown in Appendix 4 that as the area of each serial section that is analyzed is increased, the difference between the maximum and the minimum values obtained for the genus decreases. As a result, it can be stated that as the surface-area-to-volume ratio of the sample analyzed decreases, the difference between the experimentally determined maximum and minimum values of genus also decreases.

It was found experimentally that if 150 to 200 features or void areas are contained in the area analyzed on each serial section, then the difference between  $G_V^{\max}$  and  $G_V^{\min}$  is less than 15 per cent of the value of  $G_V^{\max}$ . Therefore, if  $G_V^{\max}$  and  $G_V^{\min}$  are averaged, the resulting value will be within about 7 per cent of the actual value of genus per unit volume.

#### 6.13.2 Correlation Error

Some error is involved in comparing adjacent serial sections during the experimental analysis as it cannot always be unambiguously established that a certain event has occurred between sections. As a result, it is necessary to make some arbitrary decisions during the analysis, the number of which increases relative to the total number of observations as the spacing between serial sections is increased. The error accompanying the correlation of adjacent serial sections may be reduced to an acceptable level by choosing the spacing of the sections so that the number of arbitrary decisions which must be made is a reasonably small fraction of the total value of the parameter being monitored. This spacing must be established for each structure examined. If a spacing of approximately 0.1 of the particle diameter is used, then one event in about 250 has to be established arbitrarily.

As the spacing is decreased, a greater number of sections must be considered in order to analyze the same total thickness, or volume of material. Therefore, as the spacing is decreased, the total time spent in correlating the serial sections is increased proportionally.

The maximum error resulting from arbitrary decisions during the course of this work is present in the results for the lowest density samples of the 48 micron electrolytic powder due to the highly irregular void-solid interface of these samples (see Figures 47, 48 and 49). This error for these samples is probably at most a few per cent, and for the remaining samples, it is probably less than 1 per cent.

#### 6.13.3 Total Number of Serial Sections Which Must Be Analyzed to Obtain a Given Level of Accuracy

The number of serial sections which must be analyzed before the linear portion of the cumulative plots is reached depends on the circuit size or the size of the separate parts in the structure relative to the spacing between the serial sections. Linearity is not reached until a thickness has been analyzed such that the largest circuits or separate parts in the sample are detected. After linearity is reached, an additional number of sections must be analyzed in order to determine the slope of the linear portion. This number of sections can be established by applying a least-squares analysis to the linear portion of the curve. It was found experimentally during the course of this work that less than 50 serial sections must be analyzed in order to establish the slope to within a few per cent accuracy.

#### 6.13.4 Error Resulting from Inhomogeneity of the Sinter Structures

It is apparent from the nature of sintered materials that their structures are inhomogeneous, at least over short distances, as a result of local irregularities in the particle stacking, and

over greater distances in compacted structures and in structures consisting of a size distribution of particles from which the smaller particles may separate prior to sintering. If a sample containing several hundred particles is analyzed, small-scale inhomogenieties are averaged out. For most of the samples analyzed during the course of this work, on the order of 100 particles were contained in the area of each serial section considered; therefore, the total number of particles included in the volume analyzed is about 400 to 500. Long-range inhomogenieties, such as gravitational effects [35], should not be important as far as the results obtained during the course of this work are concerned.

All samples analyzed during the course of this work were taken some distance (at least 1/8 inch) from the surface of the respective sinter bodies so that rapid closure of channels adjacent to the surface [30] would not affect the results. Therefore, it is expected that the results of this work are representative of the bulk properties of the respective sinter structures.

#### 6.13.5 Error Resulting from Uncertainty in the Position of the Deformation Retract

Recall that the node-branch networks on which the theory and experimental analysis are based consist of nodes and branches which are points and lines, respectively, and hence occupy no volume as do the void or material spaces of an actual sinter body. The position of the deformation retract cannot be uniquely established for an actual sinter structure, and its position becomes increasingly uncertain as the volume fraction of the space it represents increases. Therefore, some error is introduced into the experimental

results. Consider, for example, Figure 130 which shows a portion of the void or material space of a sinter structure. Assume that if the void-solid interface was shrunk uniformly until only nodes and branches were present, the superimposed network shown in Figure 130a would be formed. If this portion of the network were sectioned in the direction indicated so that the side of the sample passed along the dotted line with the sample to the right of the dotted line, then an error would be introduced as follows. Consider first the maximum limit of the genus. In this case, the branches crossing the sample surface at the points indicated by arrows in Figure 130a would be connected to the exterior node. During the actual analysis, the position of the branches cannot be precisely established due to the three-dimensional character of a channel; thus, the node-branch configuration shown in Figure 130b is assumed. As a result, the number of branches incident on the external node is less than it should be, and in general the experimentally determined maximum limit of genus is less than the true maximum limit.

This effect causes the experimentally determined minimum limit of genus to be in error also. In this case, the branches crossing the surface of the sample in Figure 130a are assumed to be capped at the sample surface, and there is no connection through the network between points 1 and 2. In the actual analysis, however, the network shown in Figure 130b is obtained with the branch to the external node capped at the sample surface, indicating points 1 and 2 as connected. Therefore, the experimentally determined minimum value of genus is greater than the true minimum limit.

Note that both the maximum and minimum experimentally determined values of genus are changed by the effect described



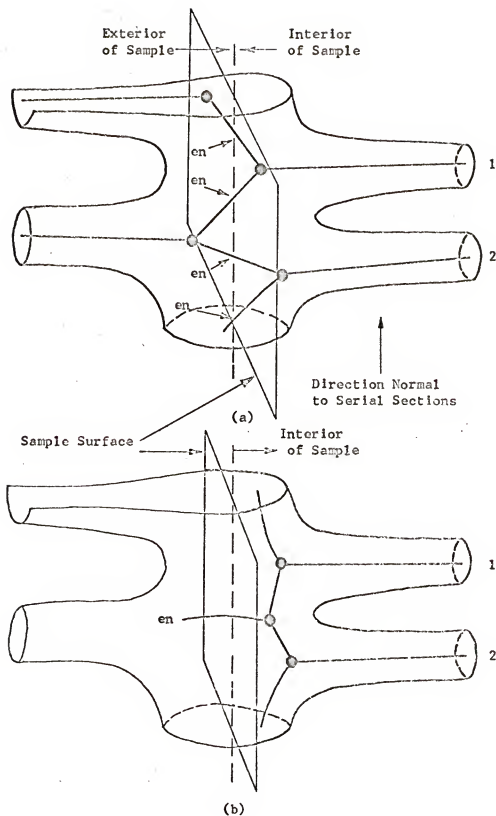


Figure 130. Schematic void space configuration employed to illustrate the error resulting from uncertainty in the position of the deformation retract.

above in such a way that they approach each other as the error increases. The maximum value will always be greater than the minimum value as the result of branches connected to the external node; however, it is possible for the minimum value to be greater than the actual value of the genus or for the maximum value to be less than the actual value as a result of this effect. Since this effect decreases the maximum and increases the minimum values of genus, the experimentally determined values should lie closer to the actual value of genus than in the ideal case. The experimentally determined values will not lie further from the actual value than for the ideal case.

It is likely that the maximum and minimum experimental values lie close to the actual value for all samples analyzed during the course of this work. This is because the maximum possible difference between these three values is small since the genus of the structures analyzed is large and the area analyzed on each section is also large. An indication of the maximum error which could result from this effect can be obtained as follows.

The 7.05 gm/cc sample of the 115 micron spherical powder is used as an example since the error for the analysis of the metal space of this sample is probably more than that for any of the other samples analyzed during the course of this work.

The error resulting from the indeterminacy of the positions of branches increases as the volume fraction of the space under consideration increases. That this error is present is indicated by little or no difference between the slopes of the cumulative maximum and minimum genus versus volume of material analyzed curves. This can be seen in Figures 57, 58, 62, 78 and 79.

The value of genus per unit volume for the 7.05 gm/cc sample of the 115 micron spherical powder is  $0.951 \times 10^6 \text{ cm}^{-3}$ . From equations (48), (50), (54) and (55), the difference between the maximum and minimum values of connectivity per unit volume for a stack of six-branch nodes in the shape of a circular cylinder with diameter,  $D$ , is

$$C_V^{\max} - C_V^{\min} = \frac{4}{DS^2} \quad (32)$$

where  $S$  is the edge length of a cube with volume equal to the average volume occupied by one six-branch node. A circular cylinder is used because the area of each section analyzed for the 115 micron spherical powder samples was circular. Equation (52) can be solved for  $S$  using the above value of genus. Equation (32) can then be solved to obtain an estimate of the maximum difference between the maximum and minimum values of genus per unit volume. The value obtained is

$$G_V^{\max} - G_V^{\min} = 0.3 \times 10^6 \text{ cm}^{-3}$$

This difference is indicated by the dotted lines in Figure 58, assuming the experimental slope is the actual value. The dotted lines give an estimate of the maximum possible difference. This indicates that the maximum error involved in taking the slope of the experimental curve as the actual value is not very large. A number of the experimental curves differ by about the same relative amount as the dotted lines of Figure 58. Therefore, the error due to the effect discussed in this section is generally small. This error decreases as the volume fraction of the space (metal or void) analyzed decreases (i.e., as the position of the deformation retract becomes more certain).

#### 6.13.6 Error Resulting from the Presence of Large-Scale Features in the Structure

Some error may result from the fact that large circuits or separate parts in the structure under consideration may not be observed as a result of the limited size of the volume of the structure which is analyzed. The smallest loops and separate parts which can remain unobserved have approximately the same dimensions as the volume analyzed. This effect becomes more important for small values of genus per unit volume. The volume analyzed must be increased in order to establish a result of the same accuracy as the genus decreases. When a thickness has been analyzed which is of the order of the dimension of the area analyzed on each section, further increase in the thickness analyzed will not increase the accuracy of the results. In order to further increase the accuracy, both the area and thickness analyzed must be increased.

For the volumes analyzed during the course of this work for the 48 micron powders, the error described above could be as large as  $0.02 \times 10^6 \text{ cm}^{-3}$ , which is small relative to most of the values of genus and number of separate parts obtained for these samples (see Tables 9, 10 and 11). For the samples having low values of genus, this effect could be significant; however, the trend in the genus and number of separate parts with density established during the course of this work would not be significantly affected even if these low values of genus and number of separate parts were considerably in error.

Recall (see Section 5.3.2) that a large fraction of the separate parts observed are small separate parts so the error

resulting from failure to detect large separate parts should not be significant relative to the total number of separate parts observed.

#### 6.13.7 Error in the Number of Separate Parts

Separate parts which intersect the surface of the volume analyzed were not included in the number of separate parts counted during the analysis of samples considered during the course of this work. The resulting error is less than 11 per cent according to the calculations in Appendix 2.

#### 6.14 The Design of Serial Sectioning Experiments

As a result of the experience gained during the course of this work, the following summary can be made concerning the experimental procedure and the accompanying accuracy of the result.

In general, the space with the lowest volume fraction should be chosen for analysis. Ideally, the serial sections should be spaced so that 10 or more intersect a distance equal to the diameter of the smallest particles from which the structure was formed. For an actual structure at low density, it may be desirable to neglect the smallest particles so that a larger spacing between sections can be used. The spacing of the serial sections must be established for each case so that the error and time spent in the analysis are optimized. The area analyzed on each serial section should contain about 150 features or void areas and about 50 serial sections should be analyzed. Under these conditions, the average of  $G_v^{\max}$  and  $G_v^{\min}$  ( $G_v^{\max}/2 + G_v^{\min}/2$ ) will be within about 10 per cent of the actual value of genus of the structure analyzed.

## CHAPTER VII

### CONCLUSIONS AND SUGGESTED RESEARCH

#### 7.1 Conclusions

1. The method of analysis developed during the course of this research can be employed to determine the topological properties, genus and number of separate parts of the void-solid interface of any sinter structure.

2. The general features of the variation of the topological properties of sinter structures during sintering were found to depend on the shape, size and stacking of the particles from which the structures are formed. The particle shape is important during the first stage of sintering. In structures formed from irregularly shaped particles, multiple connections between pairs of adjacent particles may form channels and filaments. A decrease in genus occurs as these channels close and the filaments pull apart. After this decrease is complete, the genus may increase as a result of the formation of new contacts produced by shrinkage. In structures formed from particles with smooth surfaces, the genus increases throughout the first stage of sintering as a result of the formation of contacts between particles. The remainder of the path of change of the topological properties is similar, independent of the

irregularity in the shape of the particles. The genus begins to decrease and separate parts are formed when channels formed by three or more particles begin to close. This continues until the genus reaches zero and the structure consists entirely of simply connected separate parts. After channel closure is complete, conglomeration dominates the remainder of the sintering process.

If the particle shape and stacking is held constant and the size of the particles is decreased, the magnitude of the specific topological properties throughout the sintering process is increased. The specific topological properties of two structures formed from particles which differ only in size can be related by a scale factor which is established by the relative size of the particles.

Differences in particle stacking affect the sample density at which each of the three stages of the sintering process begins and ends. The unsintered density is decreased by reducing the coordination number of the particles. As a result, first-stage sintering begins at a lower density when the coordination number in the unsintered stack is reduced. This is also true of second- and third-stage sintering.

3. The variation in the metric properties during sintering of the structures for which the topological properties were measured is consistent with the three-stage behavior of the topological properties during the sintering process.

4. The variation in the grain boundary structure during sintering was found to be closely linked to the variation in the genus. During the first stage, the grain boundaries are pinned in the neck regions between particles. As channel closure takes place,

triple lines of the type solid-solid-solid are formed and the grain boundaries become less pinned. Normal grain growth can then take place, more grain growth occurring as more channels close. This continues until exaggerated grain growth begins. The evolution of the grain boundary network through normal grain growth is restricted by the genus of the void-solid interface. The concept of a conditional minimal interface can be extended to include the grain boundary network; that is, a given surface area per unit volume, pore volume fraction and value of genus has associated with it a given grain boundary structure. As the genus and pore volume fraction decrease, so does the grain boundary area through grain growth. The conditional minimal void-solid interface plus the grain boundary network can be referred to as the conditional minimal structure.

5. The combination of the topological and metric properties provides a detailed, quantitative description of the geometric structure of a sinter body at any stage of the sintering process.

## 7.2 Suggested Research

The observations made during the course of this work indicate that the evolution of the topological properties of the void-solid interface and the grain structure of a sinter body are closely related. Coble [22] has suggested that a "metastable structure of pores and grain boundaries" exists during second-stage sintering.

Much work has been done on the role grain boundaries play in the sintering process [9, 22, 31 and 37 to 41]. This work indicates that a study of the evolution of the void-solid interface and the grain structure during second- and third-stage sintering by means of



the serial sectioning technique could yield valuable information concerning the sintering process, grain growth and the interaction between the two.

The topological properties of the phases and the interface between phases in two-phase and multi-phase materials may also be of interest. The evolution of the genus (or connectivity) during phase transformations has been mentioned previously [4, 14]. An investigation of the evolution of the topological properties during phase transformations could yield a more detailed description of the structural evolution during phase transformations than is presently available.

It has also been pointed out that highly connected structures may be present in superplastic two-phase alloys [3]. The topological properties of these alloys may be of importance in establishing a relationship between structure and the superplasticity phenomenon in these alloys.

## APPENDICES

## APPENDIX 1

### DETERMINATION OF THE NUMBER OF IDENTIFIABLE FEATURES PER UNIT VOLUME USING SERIAL SECTIONS

It is necessary to determine the genus and number of separate parts on a per-unit-volume basis. A general approach for determining the number of identifiable features per unit volume from measurements made on serial sections was developed by Steele [3] and is presented here.

In order for this technique to produce a representative value for the number of features per unit volume, it is necessary to assume a homogeneous structure within a sample volume,  $V_S$ , where  $V_S \ll V$ , the total volume of the structure, and yet larger than the incremental volume between adjacent serial sections. The expected number of features within a sample volume,  $V_S$ , is

$$\langle N_S \rangle = \overline{N_V} V_S \quad (33)$$

where  $\overline{N_V}$  is the average volume density of the features of interest.

The cumulative number of features observed with the sectioning technique after  $n$  incremental volumes have been considered is given by

$$N(n) = N_0 + \sum_{i=1}^n N_i \quad (34)$$

where  $N_0$  is the number observed on the initial section, and  $N_i$  is the number of features in the  $i^{\text{th}}$  incremental volume. Thus, for large values of  $n$  [i.e., where the cumulative sample volume,  $V(n)$ , is greater than  $V_S$ ], the summation in equation (34) can be approximated by  $\overline{N_V}V(n)$ ; therefore

$$N(n) \approx N_0 + \overline{N_V}V(n) \quad (35)$$

The cumulative number of features will therefore increase linearly with volume sectioned, for  $n$  sufficiently large. Hence, the slope of a plot of the cumulative function,  $N(n)$ , versus cumulative sample volume,  $V(n)$ , is the average volume density of features,  $\overline{N_V}$ .

A cumulative volume density of features can also be defined

$$N_V(n) = \frac{N(n)}{V(n)} \quad (36)$$

and measured as a function of the volume of material sampled. This function converges to the asymptotic value,  $\overline{N_V}$ , since

$$\lim_{n \rightarrow \infty} [N_V(n)] = \lim_{n \rightarrow \infty} \left[ \frac{N(n)}{V(n)} \right] = \lim_{n \rightarrow \infty} \left[ \frac{N_0}{V(n)} + \overline{N_V} \right] = \overline{N_V} \quad (37)$$

The two functions,  $N(n)$  and  $N_V(n)$ , are illustrated in Figure 131

[3] for grains in polycrystalline aluminum. The value of cumulative density,  $N_V(n)$ , is approximately 10 per cent higher than the estimate of its asymptotic value obtained from the slope of the linear relation between the cumulative number,  $N(n)$ , and  $n$ . The asymptotic value is represented by the dashed line in Figure 131. This example indicates that the slope of a plot of cumulative number versus volume of material sampled or analyzed gives the best estimate of the number per unit volume, since the cumulative density converges very slowly.

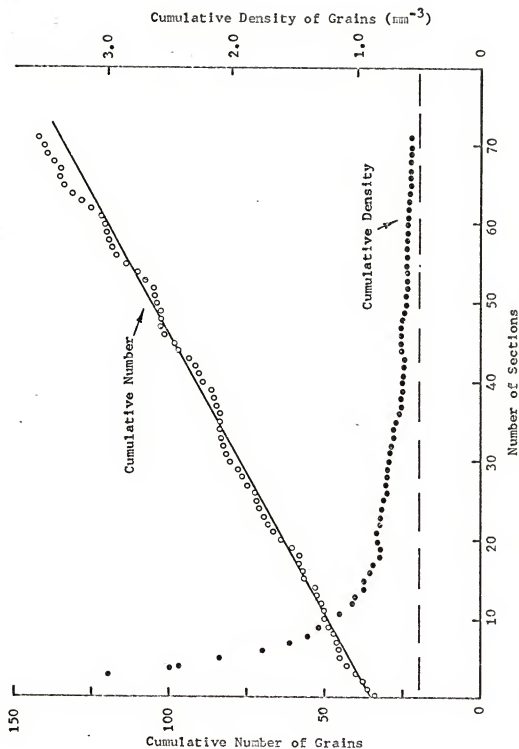


Figure 131. Cumulative grain data obtained from 72 serial sections. Note that the cumulative density approaches the asymptote (dashed line), which was calculated from the slope of the cumulative number data (Steele [3]).

APPENDIX 2

SEPARATE PARTS ERROR RESULTING  
FROM THE SURFACE EFFECT

For all sinter structures analyzed during the course of this work, the shape of a large fraction of the isolated separate parts can be characterized as nearly spherical in shape. In this case, the error resulting from neglecting those separate parts which contact the sides of the sample can be estimated by means of the following model.

The average diameter,  $\bar{D}$ , of the separate parts can be approximated by 1.5 times the mean pore intercept,  $\bar{\lambda}$ , which is given by equation (20).

Separate parts which have centers less than  $\bar{D}$  from the sides of the sample will contact the sides of the sample. Consider Figure 132. The square area which is analyzed on each serial section has sides of length  $L$ . After a thickness  $t$  has been analyzed, all separate parts with centers lying in the volume swept out by the shaded area to a depth  $t$  will contact the sides of the sample. Only those separate parts which contact the sides of the sample and have their centers inside the volume analyzed will contribute to the error. Those separate parts which intersect the top and bottom of the volume analyzed can be neglected as it is only

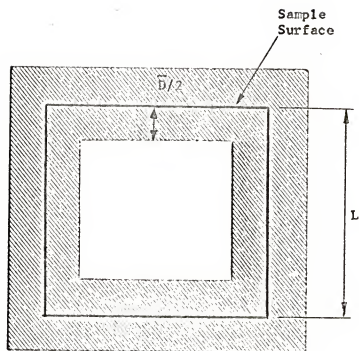


Figure 132. Illustration used to estimate the separate part error resulting from the surface effect.

necessary to determine the change in the number of separate parts which intersect the sample surface with volume analyzed in order to determine the error in the number of separate parts per unit volume. The number which intersects the sides of the sample,  $N_S$ , after a thickness,  $t$ , has been analyzed is

$$N_S = [4\bar{L}\bar{D}/2]t N_V \quad (38)$$

where  $N_V$  is the number of separate parts per unit volume. This number divided by the number of separate parts in the volume analyzed is the relative error,  $E$ , and is given by

$$E = \frac{\frac{4\bar{L}\bar{D}t}{2}N_V}{L^2tN_V} = \frac{2\bar{D}}{L} \quad (39)$$

Most values of  $L$  used during the course of this work are approximately  $7 \times 10^{-2}$  cm or greater, as shown in Table 19. The value of  $\bar{\lambda}$  is approximately 26 microns for most of the structures prepared from the 48 micron powders; therefore, the relative error according to equation (39) is

$$E = \frac{2(39 \times 10^{-6})}{7 \times 10^{-2}} = 0.11$$

Thus, the error in  $N_V$ , due to the sample surface effect, is about 11 per cent. This is probably an overestimate as  $1.5\bar{\lambda}$  is probably greater than  $\bar{D}$  for isolated separate parts. This is because many of the separate parts grow smaller and disappear during the sintering process. Therefore,  $\bar{\lambda}$  for the separate parts should be less than  $\bar{\lambda}$  for the entire void space of a structure which includes the multiply connected portion of the void space as well as the isolated separate parts.



Table 19. Values of L and D.

Sample Density (gm/cc)	L (cm)	D (cm)
<u>115 Micron Spherical Powder</u>		
7.05	-	0.1126
7.50	-	0.1126
7.76	-	0.1126
8.05	-	0.1126
<u>48 Micron Spherical Powder</u>		
7.26	0.1075	-
7.74	0.1075	-
8.00	0.1075	-
8.25	0.1075	-
8.40	0.1075	-
<u>48 Micron Electrolytic Powder</u>		
1.30	0.063	-
2.81	0.051	-
3.99	0.079	-
4.96	0.077	-
6.05	0.077	-
6.95	0.091	-
7.92		

### APPENDIX 3

#### RELATION BETWEEN THE VALUES OF GENUS FOR TWO DIFFERENT SIZE FRACTIONS OF SPHERICAL POWDER

Prior to sintering, the genus per gram for a single size fraction of spherical powder is given by equation (7) where  $C_p/P_p = \overline{b/n}$ . For two different size fractions, 1 and 2, equation (7) becomes

$$G_p(1) = P_p(1) [\overline{(b/n)}_{(1)} - 1] \quad (40)$$

$$G_p(2) = P_p(2) [\overline{(b/n)}_{(2)} - 1] \quad (41)$$

There is considerable evidence which indicates that the particle stacking is similar for any size fraction of spherical particles. The density of all such particle stacks is found to lie between 60 to 62 per cent of the theoretical density of the material. This density is difficult to change without deforming the particles [36]; therefore, the particle stacking of such a system is stable and is apparently similar for different size fractions of spherical powders.

This can be expressed for two size fractions, (1) and (2), as

$$\overline{b/n}_{(1)} = \overline{b/n}_{(2)} \quad (42)$$

On dividing equation (41) by equation (42), the following relation is obtained as the  $(\overline{b/n} - 1)$  terms cancel

$$\frac{G\rho(1)}{G\rho(2)} = \frac{P\rho(1)}{P\rho(2)} \quad (43)$$

The number of particles per gram,  $P\rho$ , is equal to the inverse of the mass of one particle; therefore

$$\frac{G\rho(1)}{G\rho(2)} = \frac{M(2)}{M(1)} \quad (44)$$

where  $M$  is the mass per particle. In terms of the theoretical density,  $\rho_{th}$ , and the volume of each particle this becomes

$$\frac{M(2)}{M(1)} = \frac{4/3\pi(r_2)^3\rho_{th}}{4/3\pi(r_1)^3\rho_{th}} = \frac{(r_2)^3}{(r_1)^3} \quad (45)$$

Combining equations (44) and (45) gives

$$\frac{G\rho(1)}{G\rho(2)} = \frac{(r_2)^3}{(r_1)^3} \quad (46)$$

For the 115 micron and 48 micron spherical powders, equation (46) gives

$$\frac{G\rho(48)}{G\rho(115)} = \frac{(115)^3}{(48)^3} = 13.74$$

#### APPENDIX 4

##### SAMPLING ERROR

Consider an ideal network formed as follows. The nodes and branches of the network correspond to small cubes and the faces of the small cubes, respectively, as illustrated in Figure 133a. A stack of these small cubes then forms a network which has six branches per node. Consider a stack which is square in cross section and extends indefinitely in the direction normal to this cross section, as illustrated in Figure 133b. The dimension of the small cubes is  $S$  and the length of an edge of the cross section of the stack of small cubes is  $L$ .

Recall that the connectivity of an actual sinter structure is obtained by determining the change in connectivity with volume of material analyzed. The analogous situation for the stack of cubes of Figure 133b can be developed as follows.

As each successive layer of small cubes is added to the stack, the connectivity and volume of the stack are increased. This is analogous to the consideration of successive serial sections through a sinter structure. The magnitude of the increase in connectivity depends on whether the maximum or minimum limit is under consideration.

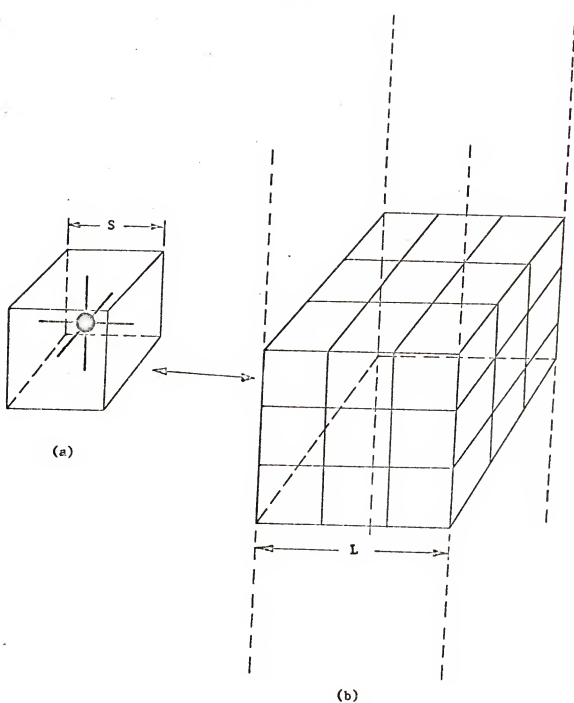


Figure 133. Illustration of a node-branch network formed from a stack of small cubes.

Consider the maximum limit first, when all branches crossing the surface of the stack are connected to an external node. Each layer consists of  $(L/S)^2$  small cubes. As each layer is added to the stack, the connectivity of the stack is changed as follows. The branches between the new layer and the preceding layer increase the connectivity by  $(L/S)^2 - 1$ . The -1 is a result of the fact that all branches, except the first, between the two layers contribute one to the connectivity. The branches in the layer contribute  $(L/S - 1)^2$  and those through the sides of the layer incident on the external node contribute  $4L/S$  to the connectivity. Thus, the maximum change in connectivity,  $\Delta C^{\max}$ , on adding one layer, is the sum of these terms, which is, on combining terms,

$$\Delta C^{\max} = \frac{2L^2}{S^2} + \frac{2L}{S} \quad (47)$$

When this is divided by the volume of the layer,  $L^2S$ , the following relation for the maximum connectivity per unit volume,  $C_V^{\max}$ , is obtained

$$C_V^{\max} = \frac{\Delta C^{\max}}{\Delta V} = \frac{2}{S^3} + \frac{2}{LS^2} \quad (48)$$

where  $\Delta V$  is the volume per layer. The quantity,  $C_V^{\max}$ , is analogous to the maximum limit for the genus per unit volume of a sinter structure.

Now consider the minimum limit of connectivity obtained when branches through the sides of the layer are capped at the surface of the stack. The minimum change in connectivity,  $\Delta C^{\min}$ , as each layer is added, is given by

$$\Delta C^{\min} = \frac{2L^2}{S^2} - \frac{2L}{S} \quad (49)$$

When this is divided by the volume per layer, the following relation for the minimum connectivity per unit volume,  $c_v^{\min}$ , is obtained

$$c_v^{\min} = \frac{\Delta c^{\min}}{\Delta v} = \frac{2}{S^3} = \frac{2}{LS^2} \quad (50)$$

The actual value of connectivity per unit volume,  $c_v^{\text{act}}$ , for a structure consisting of six-branch nodes can be obtained from equation (7) where  $c_p/p = \overline{b/n}$ . This gives

$$c_v^{\text{act}} = N_v(2) \quad (51)$$

as  $\overline{b/n}$  for a network consisting of six-branch nodes is 3. The number of nodes per unit volume,  $N_v$ , is  $1/S^3$ , which, when substituted in equation (51) gives

$$c_v^{\text{act}} = \frac{2}{S^3} \quad (52)$$

The following features of the experimentally determined cumulative genus versus volume of material analyzed curves can be inferred from equations (48), (50) and (52). As the cross-sectional area of the stack of cubes is increased, that is, as  $L$  increases, the maximum and minimum limiting values of connectivity approach the actual value of connectivity. This indicates that as the area analyzed on each serial section through a sinter structure is increased, the difference between the slopes of the maximum and minimum values of cumulative genus versus volume of material analyzed curves becomes less and these slopes both approach the actual value of the genus of the structure under consideration. This is not limited to the case where the square area of each serial section is analyzed. An area of any shape could be used for the stack of cubes or for the actual analysis of a sinter structure. The term  $2/LS^2$  in equations (48)

and (50) depends on the shape of the area chosen as follows. As each layer of cubes is added to the stack, the surface area,  $A_S$ , of the sides of the layer, through which branches to the external node pass, is given by

$$A_S = 4LS \quad (53)$$

and since the volume of the layer is  $L^2S$ , the ratio,  $R$ , of this surface area to the volume of the layer is

$$R = \frac{4}{L} \quad (54)$$

For a circular cylinder of diameter,  $D$ , the corresponding ratio is given by

$$R = \frac{4}{D} \quad (55)$$

Therefore, if the correction term  $2/LS^2$  is replaced by  $R/2S^2$ , then equations (48) and (50) hold for a stack of cubes of arbitrary cross section.



## REFERENCES

1. W. D. Jones, "Fundamental Principles of Powder Metallurgy," p. xi. 1960: London (E. Arnold, Ltd.).
2. F. N. Rhines, Reutte Plansee Proc. Third Seminar, Reutte/Tyrol, 1958, 38.
3. J. H. Steele, Jr., Doctoral Dissertation, University of Florida, 1967.
4. R. T. DeHoff, in "Quantitative Microscopy," R. T. DeHoff and F. N. Rhines, Editors, Chapter 10. 1968: New York (McGraw-Hill).
5. J. Kronsbein, L. J. Buteau, Jr. and R. T. DeHoff, Trans. AIME, 1965, 233, 1961.
6. L. K. Barrett and C. S. Yust, ORNL Report No. 4411, 1969.
7. G. C. Kuczynski, J. Appl. Phys., 1949, 20, 1160.
8. W. D. Kingery and M. Berg, J. Appl. Phys., 1955, 26, 1205.
9. H. Ichinose and G. C. Kuczynski, Acta. Met., 1962, 10, 209.
10. C. S. Smith, "Metal Interfaces," p. 65. 1952: Cleveland (American Society for Metals).
11. C. S. Smith, Met. Rev., 1964, 9 (33), 1.
12. C. S. Smith, Trans. AIME, 1948, 175, 15.
13. R. J. Charles, J. Am. Ceram. Soc., 1964, 47, 559.
14. J. W. Cahn, Acta. Met., 1966, 14, 477.
15. S. S. Cairns, "Introductory Topology," 1961: New York (The Ronald Press Company).
16. B. H. Arnold, "Intuitive Concepts in Elementary Topology," 1962: Englewood Cliffs, New Jersey (Prentice-Hall, Inc.).

17. K. R. Craig, Master's Thesis, University of Florida, 1966.
18. L. J. Buteau, Doctoral Dissertation, University of Florida, 1965.
19. R. W. Kraft, F. D. Lemkey and F. D. George, Trans. AIME, 1962, 224, 1037.
20. R. T. DeHoff, Trans. AIME, 1965, 233, 25.
21. R. A. Vandemeer and P. Gordon, Trans. AIME, 1959, 215, 787.
22. R. L. Coble, J. Appl. Phys., 1961, 32, 787.
23. J. W. Cahn, Acta. Met., 1956, 4, 449.
24. P. G. Hoel, "Introduction to Mathematical Statistics," p. 107. 1954: New York (John Wiley & Sons, Inc.).
25. R. T. DeHoff, in "Quantitative Microscopy," R. T. DeHoff and F. N. Rhines, Editors, Chapter 5. 1968: New York (McGraw-Hill).
26. E. E. Underwood, in "Quantitative Microscopy," R. T. DeHoff and F. N. Rhines, Editors, Chapter 4. 1968: New York (McGraw-Hill).
27. R. A. Gregg, Doctoral Dissertation, University of Florida, 1968.
28. F. N. Rhines, R. T. DeHoff and R. A. Rummel: A Topological Study of the Sintering Process, AEC Contract No. AT-(40-1)-2851, Annual Report, 1962.
29. T. Slean, University of Florida, Private Communication.
30. F. N. Rhines, C. E. Birchenall and L. A. Hughes, Trans. AIME, 1950, 183, 378.
31. H. G. Van Bueren and J. Hornstra, Proceedings of the Fourth International Symposium on Reactivity of Solids, Amsterdam, 1960, Elsevier, Amsterdam, 1961, 112.
32. R. T. DeHoff, R. A. Rummel, H. P. LaBuff and F. N. Rhines, "Modern Developments in Powder Metallurgy," Vol. 1: Fundamentals and Methods, p. 310. 1966: New York (Plenum Press).
33. F. N. Rhines, R. T. DeHoff and R. A. Rummel, "Agglomeration," p. 351. 1962: New York (Interscience).
34. R. T. DeHoff and F. N. Rhines: A Topological Study of the Sintering Process, AEC Contract No. AT-(40-1)-2581, Annual Report, 1968.

35. F. V. Lenel, H. H. Hausner, O. V. Roman and G. S. Ansell, Trans. AIME, 1963, 227, 640.
36. R. K. McGeary, in "Perspectives in Powder Metallurgy," Vol. 2: Vibratory Compacting, H. K. Hausner, K. H. Roll and P. K. Johnson, Editors, p. 211. 1967: New York (Plenum Press).
37. R. L. Coble and J. E. Burke, Proceedings of the Fourth International Symposium on Reactivity of Solids, Amsterdam, 1960, Elsevier, Amsterdam, 1961, 38.
38. L. Seigle, Kinetics of High-Temperature Processes Conference, Deadham, Mass., 1958, 172.
39. A. Mohanty and E. Bauman, (Inst. Met., Sisak, Yugoslovic), Acta. Met., 1963, 11, 84.
40. R. L. Coble, J. Appl. Phys., 1961, 32, 793.
41. R. L. Coble, in "Diffusion Sintering in the Solid State: Kinetics of High-Temperature Processes," W. D. Kingery, Editor, p. 147. 1959: M.I.T. (Technology Press, J. Wiley & Sons).

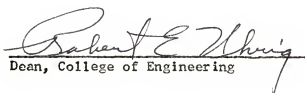
## BIOGRAPHICAL SKETCH

Edward Howard Aigeltinger was born December 25, 1941, at Glen Cove, New York. He was graduated from Southwest Miami Senior High School in June, 1959. He received the degree of Bachelor of Science in Metallurgical and Materials Engineering from Cornell University in June, 1964. In December, 1967, he received the degree of Master of Engineering in Metallurgical and Materials Engineering from the University of Florida. From October, 1967, until the present time, he has pursued the degree of Doctor of Philosophy in Metallurgical and Materials Engineering at the University of Florida.

The author is a member of Alpha Sigma Mu, American Society for Metals and The Metallurgy Society of the American Institute for Metallurgical, Mining and Petroleum Engineers.

This dissertation was prepared under the direction of the chairman of the candidate's supervisory committee and has been approved by all members of that committee. It was submitted to the Dean of the College of Engineering and to the Graduate Council, and was approved as partial fulfillment of the requirements for the degree of Doctor of Philosophy.

March, 1970

  
Dean, College of Engineering

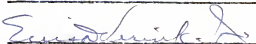
---

Dean, Graduate School

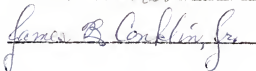
Supervisory Committee:

  
Chairman

  
\_\_\_\_\_

  
\_\_\_\_\_

  
\_\_\_\_\_

  
\_\_\_\_\_